قَالَ رَبِّ بِمَآ أَنۡعَمۡتَ عَلَيَّ فَلَنۡ أَكُونَ ظَهِيرٗا لِّلۡمُجۡرِمِينَ ١٧

سُورَةُ القَصَصِ

He said (Moses), "My Lord, for the favor You bestowed upon me, I will never be an assistant to the criminals." Qur'an (28:17)

This result is too beautiful to be false;
it is more important to have beauty in one's equations
than to have them fit experiment.

Paul Dirac, Nobel prize laureate in Physics, 1933

Theories have four stages of acceptance:

1. This is worthless nonsense;
2. This is interesting, but perverse;
3. This is true, but quite unimportant;
4. I always said so.

J. B. S. HALDANE, 1963

University of Alberta

A Particle Engineering Approach for the Design of Structured Microparticles

by

Mohammed Abd El-Hameed Ahmed Boraey

A thesis submitted to the Faculty of Graduate Studies and Research in partial fulfillment of the requirements for the degree of

Doctor of Philosophy

.

Department of Mechanical Engineering

Spring 2014
Edmonton, Alberta

Dedicated to prophet **Muhammad**
(peace and blessings be upon him)
The greatest man who ever walked on the face of the earth.

At the feet of my revered parents
Abd El-Hameed & Aisha

To my most beloved
Amira, Asmaa, Hend & Yousuf

Abstract

The process of microparticle formation from evaporating microdroplets is the main production method for many products. For most of these applications (especially pharmaceutical ones) the properties and morphology of the final dry particle have to be precisely tailored to ensure the proper functionality of the final product.

Particle engineering focuses on improving particle production processes by developing physical understanding and applying models to deliberately alter the properties of the particles.

The present work discusses two aspects of the microparticle formation process, the evaporation rate and the transient concentration profiles. Although many other aspects are involved, it is thought that these two are the most influential ones.

Chapter one gives a brief introduction to the process of structured microparticle formation along with the important particle physical properties and the associated challenges. Chapter two and three introduce a new particle formation theory for the formation of microparticles when diffusion is the main mechanism of mass transport. They also introduce a simplification of the theory results through a hybrid analytical/numerical model to ease the use of the results.

Chapter four introduces a novel hybrid technique for calculation of the variable

evaporation rate of microdroplets given knowledge of the droplet trajectory and the solvent material properties. A simplification of this approach is also proposed in the case when the trajectory data has a wide margin of uncertainty.

In chapter five, the asymptotic state solution and the transient solution of the concentration profiles of an evaporating cylindrical cylinder were derived. These results are used to verify the new model proposed in chapters six and seven.

Chapter six and seven propose a new numerical model (The Adaptive Interface Sweeping Method) for the calculation of the transient concentration profiles of an evaporating solution droplet. This model is capable of modeling many physical mechanisms involved in the particle formation process. It also offers a viable technique in dealing with variable material properties and evaporation rates.

Chapter eight gives a brief discussion of the results introduced through the thesis and recommendations for future work.

Acknowledgments

Glory and Praise be to **Allah** the Almighty.

I would like to thank first and foremost my supervisor *Dr. Reinhard Vehring* for his perfectly balanced level of supervision between the two extremes of over-caring and negligence.

I am also grateful to him for his valuable advices regarding my PhD work and life in general and for preparing a good productive environment for everyone in the Particle Engineering Group.

I would like to thank *Dr. Warren Finlay* and *Dr. Carlos Lange* for their helpful feedback and assistance during various stages of my work.

I am also thankful to everyone in the Particle Engineering Group at the Department of Mechanical Engineering for their help especially *James Ivey* for proofreading the thesis draft and providing a very useful feedback.

Finally, I would like to thank my parents for their support through prayers and supplications and my wife *Amira* for taking care of everything (including myself) and sparing my time and mind to focus on my work.

Contents

List of Tables

List of Figures

Nomenclature

Symbols

A_{pro}	Droplet projected area $\left[\mathrm{m}^2\right]$
C	Solute concentration $\left[\mathrm{kg/m}^3\right]$
C_{D}	Drag coefficient [−]
C_{cs}	Slip correction factor [−]
C_{c}	Solute center concentration $\left[\mathrm{kg/m}^3\right]$
C_{f}	Feed concentration $\left[\mathrm{kg/m}^3\right]$
C_{m}	Solute mean concentration $\left[\mathrm{kg/m}^3\right]$
C_{o}	Solute initial concentration $\left[\mathrm{kg/m}^3\right]$
C_{sol}	Solute solubility $\left[\mathrm{kg/m}^3\right]$
C_{s}	Solute surface concentration $\left[\mathrm{kg/m}^3\right]$
D_{o}	Initial solute diffusion coefficient $\left[\mathrm{m}^2/\mathrm{s}\right]$
D_{s}	Solvent vapor diffusion coefficient $\left[\mathrm{m}^2/\mathrm{s}\right]$
D_i	Solute diffusion coefficient of component i $\left[\mathrm{m}^2/\mathrm{s}\right]$
E_{ss}	Steady state surface enrichment [−]
E_i	Surface enrichment of component i [−]
E_{75}	Surface enrichment at 75 % of the droplet lifetime, τ_{D} [−]
J	Solute mass flux $\left[\mathrm{kg/s.m}^2\right]$
L	Solvent latent heat of vaporization [J/kg]
M_{s}	Solvent molecular weight [kg/mol]
N	Number of grid points [−]
N_τ	Number of normalized time steps [−]

P	Packing factor [−]
P_{s}	Solvent surface vapor pressure [Pa]
P_{total}	Total pressure [Pa]
Pe_i	Péclet number of component i [−]
R	Normalized radial coordinate [−]
Re	Droplet Reynolds number [−]
T_∞	Drying gas temperature [K]
T_{d}	Droplet temperature [K]
Y_i	Mass fraction of component i [−]
$\mathbf{F}_{\mathrm{D}}$	Drag force [N]
$\mathbf{F}_{\mathrm{G}}$	Gravitational force [N]
$\mathbf{a}$	Droplet acceleration $\left[\mathrm{m/s^2}\right]$
$\mathbf{g}$	Gravitational acceleration $\left[\mathrm{m/s^2}\right]$
$\mathbf{v}$	Droplet velocity [m/s]
$\mathbf{v}_{\mathrm{av}}$	Drying gas average velocity [m/s]
$\mathbf{v}_{\mathrm{conv}}$	Velocity of the convective term [−]
$\mathbf{v}_{\mathrm{dg}}$	Drying gas velocity [m/s]
$\mathbf{v}_{\mathrm{fx}}$	Final droplet X velocity [m/s]
$\mathbf{v}_{\mathrm{fy}}$	Final droplet Y velocity [m/s]
$\mathbf{v}_{\mathrm{ix}}$	Initial droplet X velocity [m/s]
$\mathbf{v}_{\mathrm{iy}}$	Initial droplet Y velocity [m/s]
$\mathbf{v}_{\mathrm{r}}$	Relative velocity between the droplet and the gas phase [m/s]
$\mathbf{v}_{\mathrm{ts}}$	Droplet terminal settling velocity [m/s]
$\tilde{c}_\infty$	Solvent vapor concentration far from the droplet $\left[\mathrm{kg/m^3}\right]$
$\tilde{c}_{\mathrm{s}}$	Solvent vapor concentration at the droplet surface $\left[\mathrm{kg/m^3}\right]$
$\tilde{t}$	Dummy variable for time [s]
c_{p}	Solvent specific heat [J/kg.K]
c_{ss}	Lattice speed of sound [−]
d	Droplet diameter [m]

d_{a}	Aerodynamic diameter [m]
d_{o}	Initial droplet diameter [m]
d_{sh}	Internal void diameter [m]
d_{t}	Tube internal diameter [m]
d_{v}	Volume equivalent diameter [m]
e	Concentration enrichment [−]
e_{κ}	The error in the evaporation rate [−]
e_{m}	The error in the solute mass [−]
f	Droplet generation frequency [Hz]
g_{α}	Solute particle distribution function [−]
g_{α}^{eq}	Solute equilibrium particle distribution function [−]
k	Drying gas thermal conductivity [W/m.K]
m	Mass [kg]
m_{o}	Initial solute mass [kg]
n_{int}	Number of time steps between interface updates [−]
r	Radial coordinate [m]
r_{o}	Initial droplet radius [m]
r_{s}	Droplet radius at time t [m]
s	Saturation ratio [−]
s_{o}	Initial saturation ratio [−]
t	time [s]
t_{p}	Precipitation time [s]
t_{sat}	Time to reach saturation [s]
t_{t}	Time to reach true density [s]
v	Volume $\left[\mathrm{m}^3\right]$

Greek Letters

$\Delta\tau$	Normalized Time step [−]
$\Delta\tau_{\mathrm{max}}$	Maximum stable normalized time step [−]
Δr	Change in the droplet radius [m]

Δt	Time step [s]
$\Delta\Omega$	The area between two interfaces $\left[\mathrm{m}^2\right]$
ϵ	Tolerance [−]
κ	Evaporation rate $\left[\mathrm{m}^2/\mathrm{s}\right]$
κ_{o}	Initial evaporation rate $\left[\mathrm{m}^2/\mathrm{s}\right]$
κ_{rel}	Real evaporation rate $\left[\mathrm{m}^2/\mathrm{s}\right]$
κ_{sim}	Simulated evaporation rate $\left[\mathrm{m}^2/\mathrm{s}\right]$
λ	Mean free path of the drying gas [m]
λ_κ	Evaporation rate decay rate [−]
λ_{s}	Dynamic shape factor [−]
λ_D	Diffusion coefficient decay rate [−]
μ	Drying gas dynamic viscosity [Pa.s]
Ω	The collision operator [−]
$\partial\Omega$	The droplet interface [−]
ρ_*	Reference unit density $\left[\mathrm{kg}/\mathrm{m}^3\right]$
ρ_{dg}	Drying gas density $\left[\mathrm{kg}/\mathrm{m}^3\right]$
ρ_{d}	Droplet density $\left[\mathrm{kg}/\mathrm{m}^3\right]$
ρ_{l}	Solvent density $\left[\mathrm{kg}/\mathrm{m}^3\right]$
ρ_{p}	Particle density $\left[\mathrm{kg}/\mathrm{m}^3\right]$
ρ_{sh}	Shell density $\left[\mathrm{kg}/\mathrm{m}^3\right]$
ρ_{t}	Solute true density $\left[\mathrm{kg}/\mathrm{m}^3\right]$
ρ_i	True density of component i $\left[\mathrm{kg}/\mathrm{m}^3\right]$
τ	Normalized time [−]
τ_{D}	Droplet lifetime [s]
τ_{final}	Normalized final evaporation time [−]
τ_{g}	Lattice relaxation time [−]
τ_{p}	Normalized precipitation time [−]
τ_{ro}	Initial droplet relaxation time [s]

τ_{r} Droplet/particle relaxation time [s]

τ_{sat} Normalized time to reach saturation [−]

τ_{sh} Normalized shell formation time [−]

τ_{t} Normalized time to reach true density [−]

Abbreviations

AISM The Adaptive Interface Sweeping Method

BGK Bhatnagar-Gross-Krook

C-D Coupled-derivative

CFL Courant-Friedrichs-Lewy

CSS Critical supersaturation

ES Equilibrium saturation

LBM The Lattice Boltzmann Method

PDF Particle Velocity Distribution Function

pMDIs Pressurized Metered Dose inhalers

SEM Scanning Electron Microscope

Chapter 1

Introduction

Evaporation of solution droplets is a topic of major importance to a wide spectrum of applications, ranging from industrial and medical ones to pure theoretical investigations. Many industrial products depend in one way or another on evaporating solution droplets to obtain the final product. Examples include the manufacturing of dairy products, powders for inhalation and many other pharmaceutical and industrial products [Vehring, 2008; Vehring et al., 2007; Boraey and Vehring, 2014].

1.1 Structured microparticles

A structured microparticle is a microparticle with a specific internal structure and properties.

The successful design of structured microparticles is a key factor in their success for their intended use. The properties and functionality of the final dry powder depend on its composition, which in turn depends on the history of solutes concentration profiles of the formed particle. It also depends on the composition and morphology of the particle shell, which is determined by the shell formation process at the later stages of the evaporation [Vehring, 2008; Boraey and Vehring, 2014].

During the preliminary design of products that rely on microparticles, such as dairy products or pharmaceutical powders, the ability to estimate the final dried particle properties based on formulation and process parameters can ease process development. The properties and functionality of the final dried product depend on the particle morphology, which varies given changes in drying process parameters or the physiochemical properties of the formulation.

In the case of a multi-component formulation, the spatial distribution of the different components is a key factor in the design of layered particles for microencapsulation [Schwendeman, 2002; Wischke and Schwendeman, 2008; Vehring, 2008], stabilization of biotherapeutics [Matinkhoo et al., 2011] and vaccines [Ingvarsson et al., 2013], and controlled release applications [Arifin et al., 2006]. Shell thickness and composition are responsible for controlling the drug release profiles and rates

Parts of this chapter has been published in the following publications.

1. M.A. Boraey and R. Vehring. Diffusion controlled formation of microparticles. *Journal of Aerosol Science*, 67:131–143, 2014

[Nie et al., 2010; Tan et al., 2005; Xu et al., 2013]. Particle size and surface chemistry also play a vital role in targeted delivery applications [Champion et al., 2008].

1.2 Spray drying as a microparticles manufacturing technique

The evaporation process is a challenging problem to deal with due to the many interacting physical mechanisms involved. However, many industrial applications rely on droplet evaporation using one of the various drying techniques [Nandiyanto and Okuyama, 2011]. Spray drying is a well established, scalable, and relatively simple one step process for drying solution droplets in a wide spectrum of applications.

There is a growing trend to use spray drying in the development of new pharmaceutical formulations, especially respirable dosage forms that contain proteins [Park et al., 2011; Schwendeman, 2002] , vaccines [Corbanie et al., 2007, 2008; Lee et al., 1997], biomolecules [Maltesen et al., 2008; Hoe et al., 2013d; Matinkhoo et al., 2012], lipids [Vehring et al., 2012], multi-component formulations [Hoe et al., 2013c], poorly soluble actives [Boraey et al., 2013b; Lu and Park, 2013; Hoe et al., 2013b], or nanoparticles [Nandiyanto and Okuyama, 2011; Okuyama et al., 2006a], fueled by the ability of the process to produce dry particles with a wide range of desired properties in one simple manufacturing step [Nandiyanto and Okuyama, 2011].

1.3 Design targets of structured microparticles

During the design stage for structured microparticles, several dry particle properties are required to ensure a successful functionality of the produced powder.

The purpose of the design stage is to decide the different production process parameters to ensure that the resulting powder possesses the required properties.

These properties can be split into four categories as following.

- Properties related to the internal structure: i.e., solid, hollow, layered ... etc.
- Properties related to the composition: Like spatial distribution of different components in the final dry particle and shell composition.
- Properties related to the physical behavior of the final dry particle: Like dry particle diameter, aerodynamic diameter , particle density and shell thickness for hollow particles.
- Properties related to the solid state: Like a preferred solid state (amorphous or crystalline) for different components in the final dry particle.

1.4 Particle engineering as a design approach

The process of particle formation due to the evaporation of solution droplets has been extensively studied and reviewed [Vehring, 2008]. Nandiyanto and Okuyama reviewed different dry particle morphologies and the corresponding manufacturing techniques [Nandiyanto and Okuyama, 2011]. Generally, the theoretical description

of evaporation processes is a challenging problem due to the many interacting physical mechanisms involved.

Particle engineering [Vehring, 2008; Vehring et al., 2007] provides an efficient way of developing new formulations in a time and cost effective manner. It explores the mechanisms governing the particle formation process and provides an easy-to-use approach for systematic design of engineered microparticles for a wide range of applications [Chen et al., 2011; Feng et al., 2011].

1.5 Challenges of the particle engineering approach

In order to make accurate predictions about the particle formation process, some process parameters need to be determined.

The first parameter is the determination of the evaporation rate, κ. As will be shown later this is the main factor that controls the particle formation process. Normally the assumption of a constant evaporation rate is used. This assumption may be valid for pure single component droplets. But in general, systems of practical importance are multi-component mixtures of different solvents and solutes. In this case a constant evaporation rate is not a good approximation. In the present work, a simple and fast approach for the determination of the variable evaporation rate is proposed.

The second parameter is the determination of the material properties. Material properties are generally specific to each formulation and have to be known *a priori*. Although the present work does not provide a means for the estimation of the material properties, it proposes a numerical framework which makes it easy to deal with variable material properties, i.e., solute diffusivity and the concentration needed to initialize shell formation, especially for interacting components.

In the present work, the evaporation of a single solution droplet to form a final dry particle is considered. The effect of nearby droplets, i.e., in a spray, on the particle formation process is out of the scope of the present study.

Chapter 2

Diffusion controlled formation of microparticles: Theory

2.1 Introduction

During the preliminary stages of product design (e.g. dairy products, new pharmaceutical formulations) an estimate of the final dry particle properties is desired in order to tailor the manufacturing process parameters accordingly. But due to the highly sophisticated production techniques and the complexity of the evaporation process this estimate is either not accurate enough using simple models or computationally expensive using full numerical models. For this reason many researchers tried to introduce simple particle formation models (analytical and numerical) that can reasonably predict the main properties of the final dry particle.

In the development of analytical models [Gardner, 1965; Leong, 1987; Vehring et al., 2007; Vehring, 2008] one must make simplifying assumptions such as a constant evaporation rate or constant material properties to arrive at a user friendly, approximate solution. Analytical models are generally easier to use and may provide a useful estimate of the final dry particle properties; however, due to the restrictive assumptions imposed during their development, their accuracy and usability are limited .

On the other hand, numerical models [Castillo and Munz, 2007a,b; Eslamian and Ashgriz, 2007; Hubbard et al., 1975; Jayanthi et al., 1993; Vehring et al., 2007;

Parts of this chapter has been published in the following publications.

1. M.A. Boraey and R. Vehring. Diffusion controlled formation of microparticles. *Journal of Aerosol Science*, 67:131–143, 2014
2. M. Boraey, A. Baldelli, and R. Vehring. Theoretical and experimental investigation of particle formation from evaporating microdroplets. In *AAAR 32nd Annual Conference, American Association for Aerosol Research, Portland, Oregon, USA, September 30 - October 4*, 2013a
3. M.A. Boraey and R. Vehring. A particle design model for spray drying of suspensions and large molecule formulations. In *RDD Europe, Respiratory Drug Delivery.*, 2013
4. M.A. Boraey, S. Hoe, H. Sharif, D.P. Miller, D. Lechuga-Ballesteros, and R. Vehring. Improvement of the dispersibility of spray-dried budesonide powders using leucine in an ethanol-water cosolvent system. *Powder Technology*, 236:171–178, 2013b

Widiyastuti et al., 2007; Xiong and Kodas, 1993; Yu and Liao, 1998] can take into account the full range of different interacting physical mechanisms involved in the evaporation process at the expense of higher complexity. In practice, the usefulness of numerical models is also limited. Firstly, accurate material properties are often unavailable for systems of practical importance. Secondly, the iterative and exploratory nature of the design stage of microparticles makes the use of numerical models computationally demanding. Since production scale powders are generally polydisperse, numerical model results have to be obtained for every size distribution interval in a very time consuming fashion. Most useful would be a comparatively simple model that can accurately predict the final dry particle properties with an affordable computational effort.

The present chapter proposes a model of structured microparticles formation from evaporating microdroplets. It is applicable when diffusion and surface recession are the main mechanisms of mass transport in the droplet. The model accounts for the transient nature of the solute concentration profiles during the evaporation process and thereby extends previously published models [Vehring, 2008; Vehring et al., 2007] to particle formation processes in which the droplet surface recession rate is much faster than the diffusion in the droplets, i.e., to cases with large Péclet , Pe, numbers.

Furthermore, the model is useful when the initial concentration of solutes in the droplet is close to saturation. The model also predicts the dry particle diameter, assuming a spherical particle, particle density, and aerodynamic diameter. For hollow particles formed at large Péclet numbers the shell thickness can be approximated. The model is capable of predicting the radial distribution of the components in the final dry particle in the case of multi-component formulations. The results of the model were recast in a simple analytical form, which can be used in particle design without the need for numerical tools. Predictions of the model were found to be in good agreement with analytical, numerical and experimental results in the literature.

2.2 Problem background

Since the internal circulation inside a liquid droplet is induced by the shear forces on the surface of the evaporating droplet, internal circulation can be neglected for small droplet Reynolds numbers [Sirignano, 1999]. This condition is satisfied for small particles moving at low velocities relative to the surrounding gas. Finlay showed that this condition is typically fulfilled for microdroplets in the size range of inhaled pharmaceutical aerosol particles [Finlay, 2001]. For this reason diffusion can be assumed to be the dominant mechanism of mass transport.

During the evaporation of solution droplets, the radial concentration profiles of the solutes are controlled by two counteracting mechanisms. The first is the recession of the droplet surface, which promotes higher surface concentrations by sweeping the solute molecules, while the second is the diffusion of solutes from the droplet surface towards its lower concentration core. The relative importance of these two mechanisms is described by the Péclet number, Pe_i, for component i which depends on the ratio between the evaporation rate, κ, and solute diffusivity of each component in the liquid phase, D_i [Vehring, 2008; Vehring et al., 2007].

There are many definitions for the evaporation rate, κ. The definition used here is the one given by Vehring et al., [Vehring, 2008; Vehring et al., 2007]. This

definition comes from Maxwell's equation for the evaporation of a spherical liquid droplet. Maxwell's equation can be written as follows [Finlay, 2001]:

$$\frac{\mathrm{d}d}{\mathrm{d}t} = -\frac{4D_\mathrm{s}[\tilde{c}_\mathrm{s} - \tilde{c}_\infty]}{\rho_\mathrm{d} d} \tag{2.1}$$

$$-\frac{\mathrm{d}d^2}{\mathrm{d}t} = \frac{8D_\mathrm{s}[\tilde{c}_\mathrm{s} - \tilde{c}_\infty]}{\rho_\mathrm{d}} \tag{2.2}$$

Where: $\tilde{c}_\mathrm{s}$ is the solvent vapor concentration at the droplet surface and $\tilde{c}_\infty$ is the solvent vapor concentration far from the droplet surface.

According to Equation 2.2, the evaporation rate, κ, can be defined as follows [Vehring, 2008; Vehring et al., 2007]:

$$\kappa = -\frac{\mathrm{d}d^2}{\mathrm{d}t} \tag{2.3}$$

The definition given by Equation 2.3 does not take into account the following two effects:

- The suppression of the solvent vapor pressure on the surface of the evaporating droplet due to the presence of solutes or any other impurities, i.e., Raoult's law [Finlay, 2001].
- The increase of the solvent vapor pressure on the droplet surface for very small droplet diameters (d <5 μm), i.e., Kelvin effect [Finlay, 2001; Hinds, 1999].

However, there are many advantages for using this definition of the evaporation rate, κ. Firstly, the evaporation rate, κ, is constant for a droplet whose diameter squared decreases linearly with time. This is referred to as the d^2 law and provides a good estimate for the evaporation rate of pure liquid droplets [Finlay, 2001; Sirignano, 1999].

Secondly, it allows the calculation of the droplet surface recession velocity, $\frac{\mathrm{d}r_\mathrm{s}}{\mathrm{d}t}$, without knowing the droplet density, ρ_d, as follows:

$$\kappa = -\frac{\mathrm{d}d^2}{\mathrm{d}t} \tag{2.4}$$

$$\kappa = -2d\frac{\mathrm{d}d}{\mathrm{d}t} \tag{2.5}$$

$$\kappa = -8r_\mathrm{s}\frac{\mathrm{d}r_\mathrm{s}}{\mathrm{d}t} \tag{2.6}$$

$$\frac{\mathrm{d}r_\mathrm{s}}{\mathrm{d}t} = -\frac{\kappa}{8r_\mathrm{s}} \tag{2.7}$$

Where: d and r_s are the time dependent droplet diameter and radius respectively.

And finally, a time independent Péclet number, Pe, can be defined, i.e., does not depend on the droplet radius, r_s, for a droplet evaporating with a constant evaporation rate, κ.

The mass Péclet number, Pe, is defined as the ratio between the mass transfer by advection and by diffusion [Bird et al., 2006].

$$Pe = \frac{L_s U}{D} \tag{2.8}$$

Where: L_s is a length scale, U is a characteristic velocity and D is the diffusion coefficient.

In the case of an evaporating solution droplet, it is desirable to quantify the relative strength of the two acting mechanisms mentioned earlier, i.e., recession of the droplet surface and the diffusion of solutes. In this case, it is reasonable to use the droplet radius, r_s, as the characteristic length since this is the distance between the high concentration droplet surface and the low concentration core, and the solute diffusivity as D. Actually, the ratio $\frac{L_s}{D}$ can be interpreted as the resistance to the diffusion of solutes from the droplet surface to its core. U can be replaced by the droplet surface recession velocity, $\frac{dr_s}{dt}$, which is the mechanism responsible for increasing the solute surface concentration.

Using the definition of the Péclet number, Pe, given in Equation 2.8 and the velocity of the receding droplet surface given by Equation 2.7, the Péclet number, Pe, can be defined as follows:

$$Pe = \frac{\kappa}{8D} \tag{2.9}$$

Equation 2.9 shows that the Péclet number, Pe, is constant for a droplet evaporating with a constant evaporation rate, κ.

A Péclet number larger than unity indicates an evaporation rate dominant effect with a subsequent surface enrichment. A lower value indicates a higher diffusion compared to evaporation rate and a nearly flat radial concentration profile is obtained throughout the droplet lifetime [Vehring, 2008; Vehring et al., 2007].

At the end of the evaporation process the solution droplet forms a solid particle, either by crystallization or by transition to an amorphous solid. Frequently, the formation of a shell is observed [Cruz et al., 2011; Gómez Gaete et al., 2008; Gómez-Gaete et al., 2008]. Shell formation is initiated when the solute surface concentration reaches a critical value, i.e., critical supersaturation, CSS, for crystalline shells, or a concentration close to the solute true density, i.e., density of the bulk material, for amorphous shells [Vehring, 2008].

For Péclet numbers more than unity, the effect of the surface recession velocity is more significant than solute diffusion, which results in a much higher solute concentration at the droplet surface compared to its core [Gómez Gaete et al., 2008; Gómez-Gaete et al., 2008]. Evaporation at large Péclet numbers, i.e., Pe >25, is a well-established technique for the production of large porous particles with low density [Nandiyanto and Okuyama, 2011; Widiyastuti et al., 2007] for pulmonary drug delivery [Anton et al., 2012; Vehring, 2008; Weers et al., 2007].

Comprehensive models describing in detail the various processes involved in shell formation are unavailable at this time, but several individual aspects like buckling of membranes have been described [Marty and Tsapis, 2008]. However, the comparatively simple evaporation models can be applied to estimate dry particle properties:

for a given evaporation rate and initial solute concentration, and assuming a spherical dry particle, the final dry particle diameter can be estimated if the time, and with that the droplet diameter, at which shell formation commences is calculated. The shell formation time depends on the evolution of surface concentration. Many particle properties such as composition, aerodynamic diameter and particle density can then be derived from the dry particle diameter. So an accurate estimate of the shell formation time is necessary to predict final dry particle properties.

2.3 The governing equation

The equation for the conservation of mass (without taking convection into account as per the discussion in section 2.2) can be written as follows:

$$\frac{\partial C}{\partial t} + \nabla J = 0 \tag{2.10}$$

It can be combined with Fick's first law of diffusion

$$J = -D\nabla C \tag{2.11}$$

to give Fick's second law of diffusion.

$$\frac{\partial C}{\partial t} = D\nabla^2 C \tag{2.12}$$

Note that this is a special case of the general diffusion equation for a constant diffusivity, D.

For a spherically symmetric droplet, the concentration is a function of the radial coordinate only and Equation 2.12 can be written as follows:

$$\frac{\partial C}{\partial t} = D\left[\frac{\partial^2 C}{\partial r^2} + \frac{2}{r}\frac{\partial C}{\partial r}\right] \tag{2.13}$$

The radial coordinate, r, extends from the center of the droplet (i.e., $r = 0$) to the droplet surface (i.e., $r = r_s(t)$). Where $r_s(t)$ is the droplet radius at time t. Since $r_s(t)$ is time dependent, it is easier to deal with Equation 2.13 if the radial coordinate, r, is normalized by the droplet radius, r_s. Let us call the normalized coordinate R.

We can derive the normalized space derivatives as follows:

$$R = \frac{r}{r_s(t)} \tag{2.14}$$

$$\frac{\partial R}{\partial r} = \frac{1}{r_s(t)} \tag{2.15}$$

$$\frac{\partial}{\partial r} = \frac{\partial}{\partial R}\frac{\partial R}{\partial r} \tag{2.16}$$

$$\frac{\partial}{\partial r} = \frac{\partial}{\partial R}\frac{1}{r_s(t)} \tag{2.17}$$

$$\frac{\partial^2}{\partial r^2} = \frac{\partial}{\partial r}\left[\frac{\partial}{\partial r}\right] \tag{2.18}$$

$$\frac{\partial^2}{\partial r^2} = \frac{\partial}{\partial R}\frac{1}{r_s(t)}\left[\frac{\partial}{\partial R}\frac{1}{r_s(t)}\right] \tag{2.19}$$

$$\frac{\partial^2}{\partial r^2} = \frac{1}{r_s^2(t)}\frac{\partial^2}{\partial R^2} \tag{2.20}$$

While the time derivative can be derived as follows:

$$\left.\frac{\partial}{\partial t}\right|_r = \left.\frac{\partial}{\partial t}\right|_R + \frac{\partial}{\partial R}\frac{\partial R}{\partial t} \tag{2.21}$$

$$\frac{\partial R}{\partial t} = -\frac{r}{r_s^2(t)}\frac{\partial r_s(t)}{\partial t} \tag{2.22}$$

$$\frac{\partial R}{\partial t} = -\frac{R}{r_s(t)}\frac{\partial r_s(t)}{\partial t} \tag{2.23}$$

$$\left.\frac{\partial}{\partial t}\right|_r = \left.\frac{\partial}{\partial t}\right|_R - \frac{\partial}{\partial R}\frac{R}{r_s(t)}\frac{\partial r_s(t)}{\partial t} \tag{2.24}$$

Substituting Equation 2.17, Equation 2.20 and Equation 2.24 into Equation 2.13 gives the following equation:

$$\frac{\partial C}{\partial t} = \frac{D_i}{r_s^2}\left[\frac{\partial^2 C}{\partial R^2} + \frac{2}{R}\frac{\partial C}{\partial R}\right] + \frac{R}{r_s}\frac{\partial C}{\partial R}\frac{\partial r_s(t)}{\partial t} \tag{2.25}$$

Equation 2.25 is the normalized version of Equation 2.13. Note that the normalization by the time dependent droplet radius , $r_s(t)$, results in an extra convective term on the right hand side of Equation 2.25. The convective term is a function of the droplet receding surface velocity (i.e.,$\frac{\partial r_s(t)}{\partial t}$) which is a function of the evaporation rate, κ.

Substituting Equation 2.6 into Equation 2.25 gives the following equation:

$$\frac{\partial C}{\partial t} = \frac{D_i}{r_s^2}\left[\frac{\partial^2 C}{\partial R^2} + \frac{2}{R}\frac{\partial C}{\partial R}\right] - \frac{\kappa R}{8r_s^2}\frac{\partial C}{\partial R} \tag{2.26}$$

Gardner used the assumptions of a constant evaporation rate, κ, constant material properties (i.e., solute diffusivity, D_i) and asymptotic state (i.e., limit of very long evaporation time) to analytically calculate the radial solute concentration profiles and surface enrichment, E_i, [Gardner, 1965] of an evaporating spherical solution droplet (Equation 2.26) using a zero flux boundary condition at the droplet center (i.e., $\frac{\partial C}{\partial R} = 0$ at $R = 0$).

Leong used the solution developed by Gardner to predict the final dry particle morphology as a function of the nucleation and crystallization process parameters [Leong, 1987].

Vehring presented a simple theory to predict the final dry particle volume equivalent diameter, d_v, and aerodynamic diameter, d_a, in addition to different characteristic times (i.e., saturation time, t_{sat}, precipitation time, t_p, and the time to reach true density, t_t) using the results of Gardner and Leong [Vehring, 2008] under the following assumptions.

- Small Biot number, Bi (no temperate gradient) [Finlay, 2001].
- Diffusion is the only mechanism for mass transfer, (no reaction or convection) [Finlay, 2001].
- Small droplet Reynolds number, Re (no internal circulation) [Sirignano, 1999].
- Constant evaporation rate, κ.
- Constant material properties, D and c_{sol}.

Vehring's model inputs are a constant evaporation rate, κ, and a constant diffusion coefficient, D_i, for each solute component, i, in the liquid phase. The evaporation rate can be estimated from tabulated data or using simple analytical expressions like Maxwell's equation, while the diffusion coefficient, D_i, is solute and solvent specific.

A detailed discussion of the solution can be found in Leong [1987]; Vehring et al. [2007] and Appendix A. The radial concentration profile can be calculated as follows:

$$C_i(R) = C_{\mathrm{m},i}\frac{\exp(Pe_iR^2/2)}{3\int_0^1 R^2\exp(Pe_iR^2/2)\mathrm{d}R} \tag{2.27}$$

Where: C_{m} is the solute mean concentration. It is the solute concentration in the droplet assuming a uniform concentration profile.

While the solute concentration at the droplet surface, $C_{\mathrm{s},i}$, can be found by:

$$C_{\mathrm{s},i} = \frac{C_{\mathrm{m},i}}{3\beta}\exp\left(\frac{Pe_i}{2}\right) \tag{2.28}$$

$$\text{where } \beta_i = \int_0^1 R^2\exp\left(\frac{Pe_i}{2}R^2\right)\mathrm{d}R \tag{2.29}$$

The increase in the surface concentration, $C_{\mathrm{s},i}$, relative to the mean concentration, $C_{\mathrm{m},i}$, can be quantified by the surface enrichment, E_i, of component i which is the dimensionless ratio between solute surface concentration, $C_{\mathrm{s},i}$, and its mean concentration, $C_{\mathrm{m},i}$.

Surface enrichment can be calculated from Equation 2.28 as follows:

$$E_i = \frac{C_{\mathrm{s},i}}{C_{\mathrm{m},i}} = \frac{1}{3\beta_i}\exp\left(\frac{Pe_i}{2}\right) \tag{2.30}$$

An analytical approximation for E_i , which is accurate within 1% for Péclet numbers less than 20 has been provided by Vehring [Vehring, 2008; Vehring et al., 2007].

$$E_i = \frac{C_{\mathrm{s},i}}{C_{\mathrm{m},i}} \approx 1 + \frac{Pe_i}{5} + \frac{Pe_i^2}{100} - \frac{Pe_i^3}{4,000} \tag{2.31}$$

Vehring [Vehring, 2008] suggested the use of the following characteristic times to indicate the solid state of each component in the final dry particle.

$$t_{\text{sat}} = \tau_{\text{D}} \left[1 - (s_{\text{o}} E)^{\frac{2}{3}}\right] \tag{2.32}$$

$$s_{\text{o}} = \frac{C_{\text{o}}}{C_{\text{sol}}} \tag{2.33}$$

$$t_{\text{t}} = \tau_{\text{D}} \left[1 - (p_{\text{o}} E)^{\frac{2}{3}}\right] \tag{2.34}$$

$$p_{\text{o}} = \frac{C_{\text{o}}}{\rho_{\text{t}}} \tag{2.35}$$

$$t_{\text{p}} = \tau_{\text{D}} - t_{\text{sat}} = \tau_{\text{D}} \left(s_{\text{o}} E\right)^{\frac{2}{3}} \tag{2.36}$$

Where: C_{sol} is the solute solubility, t_{sat} and t_{t} are the times needed to reach saturation (for crystalline components) and true density (for amorphous components) on the droplet surface respectively.

t_{p} is the precipitation time. It is the time remaining in the droplet lifetime, τ_{D}, after the formation of the shell. A longer t_{p} for a specific component means a higher chance of forming a crystalline shell and higher crystalline content. This is because solute molecules have more time to arrange themselves in a crystal structure before their mobility is reduced by the reduction of the solvent mass fraction [Vehring, 2008; Vehring et al., 2007; Hoe et al., 2013a].

The actual precipitation time is usually less than the calculated one since τ_{D} is calculated assuming a final droplet diameter of zero. Since non-pure droplets form dry particles, the actual time remaining for crystallization is less than the one given by Equation 2.36.

2.4 Clarification of misconceptions

The analytical and numerical models discussed in section 2.1 were derived and used based on a set of assumptions. However, many studies in literature started to use these models without paying attention to these limiting assumptions [Weiler et al., 2012; Xiong and Kodas, 1993; Castillo and Munz, 2007a]. In this section, some of the misconceptions related to these models and their range of usability will be discussed.

2.4.1 Early shell formation

Shell formation is initiated when the solute surface concentration reaches a critical value. Once the shell starts to form the evaporation rate, κ, is no longer constant and the evaporation process starts to slow down.

The time at which shell formation starts depends on the initial saturation ratio, s_{o}, and the evaporation rate, κ. A common mistake is to use the asymptotic state solution of the concentration profile to predict shell composition. If critical supersaturation at the surface precedes the establishment of the asymptotic concentration profile, then it is this surface concentration that governs the shell composition. The saturation ratio has to be kept in mind while predicting the transient concentration profiles and not the concentration profiles alone.

2.4.2 Asymptotic versus steady state

The expression derived by Gardner [1965] as a solution for the 1D diffusion equation in spherical coordinates is an asymptotic solution and not a steady state solution (see the detailed derivation in Appendix A). For an evaporating solution droplet, concentration is always changing with time and so it can not reach a steady state value.

This means that the predicted concentration, C, is an asymptotic and not a steady state value which means that it is still varying with time. In Gardner's derivation the expressions for both the mean, C_{m}, and surface concentration, C_{s}, are functions of the concentration at the droplet center, C_{c}, which is time dependent.

2.4.3 Surface concentration versus enrichment

Although both the mean and surface concentrations are time dependent, the asymptotic behavior of the surface concentration leads to a steady state value of surface enrichment. This can happen when the surface concentration changes with the same time rate as the mean concentration.

The first expression that is time independent in Gardner's paper is the one for surface enrichment, E. Reviewing the derivation for the asymptotic solution reveals that this steady state behavior for surface enrichment was implicitly enforced by the imposed condition that the concentration is inversely proportional to the droplet volume for any point, R, in the asymptotic limit.

2.4.4 How long does it take to reach the asymptotic state ?

The fact that the expressions for the radial concentration profiles and surface enrichment were derived assuming an asymptotic behavior is often overlooked. There is a tendency to use these expressions at any time during the evaporation process without checking if this asymptotic state is reached or not.

From a mathematical prospective, asymptotic behavior of an equation is reached after a very long period of time. But in the case of an evaporating droplet, the whole process has a limited time period and using this equation beyond this period is invalid. In other words, although the asymptotic solution for an equation describing a physical system exists in a mathematical sense, the physical system itself may not exist by the time the solution is valid.

Every evaporating droplet has a lifetime that depends on its size and the evaporation rate. The time it takes for the solute concentration profile to reach an asymptotic behavior depends on other parameters. This time might be a fraction of or even longer than the droplet lifetime.

The asymptotic solution introduced by Gardner does not consider how long it takes for an evaporating droplet to reach that asymptotic state profile. It is important to check the validity of this assumption and to introduce an improved version of the theory for cases where this assumption is not justified. As will be shown in the results section, for large Péclet numbers or high initial saturation the error introduced by using the asymptotic state assumption becomes significant.

2.5 The normalized form of the governing equation

To the best of the author's knowledge none of the studies that used Gardner's solution of Equation 2.26 investigated the validity of his solution. The original paper itself did not try to establish any relationship between the droplet lifetime and the time required for the system to behave asymptotically. Although many studies used his solution, they did not try to check if this solution is relevant to their problem of interest.

Equation 2.26 itself does not tell us much about when the asymptotic state is reached compared to the droplet lifetime and hence does not tell us about the range of validity of the solution. The only process parameter that appears in the equation is the evaporation rate, κ. However this is not enough to precisely correlate the equation to the existing physical system of an evaporating droplet with a limited lifetime.

For all these reasons, Equation 2.26 will be normalized by the main process parameters to help us better understand its behavior. The normalization procedure will be presented in the rest of the current section.

In order to make the equation and its solution more usable, it is always desired to put it in a non-dimensional form. In this case the non-dimensional numbers will govern the behavior of the equation and its evolution in time. If these non-dimensional numbers are process related, a meaningful and usable solution can be obtained. For the rest of the chapter, the subscript i will be dropped for simplicity.

The radial coordinate, r, was already normalized by the droplet radius, r_s. The rest of the variables also need to be normalized. We will normalize the concentration, C, and the time, t. Introducing the new normalized variables c and τ.

$$\tau = \frac{t}{\tau_D} \text{ Where } \tau_D \text{ is the droplet lifetime} \tag{2.37}$$

$$c = \frac{C}{C_o} \text{ Where } C_o \text{ is the solute initial concentration} \tag{2.38}$$

All concentration derivatives, spatial and temporal, will be multiplied by C_o which will cancel out from all terms in the equation. For the rest of this chapter c will refer to the normalized concentration.

The temporal derivative will be divided by τ_D to normalize the time variable.

$$\frac{\partial}{\partial t} = \frac{\partial}{\partial \tau}\frac{\partial \tau}{\partial t} \tag{2.39}$$

$$\frac{\partial \tau}{\partial t} = \frac{1}{\tau_D} \tag{2.40}$$

$$\frac{\partial}{\partial t} = \frac{\partial}{\partial \tau}\frac{1}{\tau_D} \tag{2.41}$$

Substituting Equation 2.41 in Equation 2.26 gives:

$$\frac{\partial c}{\partial \tau} = \frac{\tau_D}{r_s^2}\left[D\left(\frac{\partial^2 c}{\partial R^2} + \frac{2}{R}\frac{\partial c}{\partial R}\right) - \kappa\frac{R}{8}\frac{\partial c}{\partial R}\right] \tag{2.42}$$

We can still remove κ and r_s from Equation 2.42 as follows:

$$d^2 = d_o^2 - \kappa t \tag{2.43}$$

$$4r_s^2 = 4r_o^2 - \kappa t \tag{2.44}$$

$$\left(\frac{r_s}{r_o}\right)^2 = 1 - \frac{\kappa t}{4r_o^2} \tag{2.45}$$

Where: d_o and r_o are the initial droplet diameter and radius respectively.

The droplet lifetime, τ_D, can be defined as follows (assuming a final droplet diameter of zero):

$$\tau_D = \frac{d_o^2}{\kappa} = \frac{4r_o^2}{\kappa} \tag{2.46}$$

Substituting Equation 2.46 in Equation 2.45 gives the following equation:

$$\left(\frac{r_s}{r_o}\right)^2 = 1 - \frac{t}{\tau_D} = 1 - \tau \tag{2.47}$$

$$\frac{\tau_D}{r_s^2} = \frac{4}{\kappa}\left(\frac{r_o}{r_s}\right)^2 = \frac{4}{\kappa}\frac{1}{1-\tau} \tag{2.48}$$

Substituting Equation 2.48 in Equation 2.42 gives the following equation:

$$\frac{\partial c}{\partial \tau} = \frac{1}{2Pe(1-\tau)}\left(\frac{\partial^2 c}{\partial R^2} + \frac{2}{R}\frac{\partial c}{\partial R}\right) - \frac{R}{2(1-\tau)}\frac{\partial c}{\partial R} \tag{2.49}$$

Equation 2.49 is much more meaningful and useful compared to Equation 2.26. All the variables are normalized and the solution is only governed by the Péclet number, Pe. The time variable is also easier to use and understand as it gives the solution of the concentration field relative to the droplet lifetime, τ_D. Note that both the diffusive and convective terms evolve with the same temporal rate (i.e., $\frac{1}{1-\tau}$) and that the convective term does not depend on the Péclet number, Pe. The convective term is also more significant at the droplet surface (i.e., $R = 1$). The smaller the Péclet number, Pe, the stronger the diffusive flux compared to the convective one. Both terms have different signs. All these observations, which agree with the physics of the problem are now more obvious by looking at Equation 2.49.

The normalized mean concentration, c_m, can also be derived in terms of the normalized time, τ, as follows:

$$c_m = \left(\frac{r_o}{r_s}\right)^3 = (1-\tau)^{-\frac{3}{2}} \tag{2.50}$$

Surface enrichment can be calculated from the solution of Equation 2.49 and Equation 2.50.

In Equation 2.49 the concentration was normalized by the initial solute concentration, C_o. However, in some cases it is more useful to express the concentration

as a saturation ratio, s where $s = C/C_{\text{sol}}$ and C_{sol} is the solute solubility. In this case the equation reads as follows:

$$\frac{\partial s}{\partial \tau} = \frac{1}{2Pe(1-\tau)}\left(\frac{\partial^2 s}{\partial R^2} + \frac{2}{R}\frac{\partial s}{\partial R}\right) - \frac{R}{2(1-\tau)}\frac{\partial s}{\partial R} \tag{2.51}$$

A numerically more plausible form of Equation 2.49 can be obtained by solving for the concentration enrichment, e, defined as the concentration, C, normalized by the mean concentration, C_{m}, (i.e., $e = \frac{C}{C_{\text{m}}}$). Time and space derivatives can be derived as follows:

$$e = \frac{C}{C_{\text{m}}} = \frac{c}{c_{\text{m}}} \tag{2.52}$$

$$c = e c_{\text{m}} \tag{2.53}$$

$$c_{\text{m}} = (1-\tau)^{-\frac{3}{2}} \tag{2.54}$$

$$\frac{\partial c_{\text{m}}}{\partial \tau} = \frac{3}{2}(1-\tau)^{-\frac{5}{2}} \tag{2.55}$$

$$\frac{\partial c_{\text{m}}}{\partial \tau} = \frac{3}{2}\frac{c_{\text{m}}}{(1-\tau)} \tag{2.56}$$

$$\frac{\partial c}{\partial R} = c_m \frac{\partial e}{\partial R} \tag{2.57}$$

$$\frac{\partial^2 c}{\partial R^2} = c_m \frac{\partial^2 e}{\partial R^2} \tag{2.58}$$

$$\frac{\partial c}{\partial \tau} = c_m \frac{\partial e}{\partial \tau} + e\frac{\partial c_{\text{m}}}{\partial \tau} \tag{2.59}$$

$$\frac{\partial c}{\partial \tau} = c_m \frac{\partial e}{\partial \tau} + \frac{3}{2}\frac{c_{\text{m}}}{(1-\tau)}e \tag{2.60}$$

Substituting Equation 2.57, Equation 2.58 and Equation 2.60 into Equation 2.49 gives the following form of the governing equation.

$$\frac{\partial e}{\partial \tau} = \frac{1}{2Pe(1-\tau)}\left(\frac{\partial^2 e}{\partial R^2} + \frac{2}{R}\frac{\partial e}{\partial R}\right) - \frac{R}{2(1-\tau)}\frac{\partial e}{\partial R} - \frac{3}{2}\frac{e}{(1-\tau)} \tag{2.61}$$

Equation 2.61 is favored numerically for two reasons. First, the concentration enrichment, e, approaches a constant value with increasing τ in contrast to c that keeps on increasing. Second, the gradient of e (i.e., $\frac{\partial e}{\partial R}$) near the droplet surface , especially for higher Pe numbers, is less as a numerical value compared to the gradient of c. These two advantages make it easier to solve for the concentration field at high Pe numbers.

2.6 A solution attempt

In order to calculate the time needed for the concentration field to reach an asymptotic state, Equation 2.49 has to be solved numerically since there is no analytical

solution to it. The numerical procedure used will be presented in this section.

Equation 2.49 is a diffusion equation with a convective term that is time and position dependent. The convective term gets stronger at the droplet surface (i.e., $R = 1$) and at the final stage of evaporation (i.e., $\tau \sim 1$). The diffusive term also gets stronger for small Péclet numbers, Pe, and near the end of the droplet lifetime. As will be shown later, these properties will have consequences on the solution procedure used.

Since the problem at hand dose not involve complex geometry, the finite difference method offers an easy and attractive way for the solution of Equation 2.49. As a first step the finite difference method can be used to solve Equation 2.49 using a fixed uniform grid and a constant time step.

Spatial derivatives were discretized using central second order differencing schemes coupled with an Euler first order explicit time stepping scheme as follows:

$$\left.\frac{\partial c}{\partial R}\right|_i^n \approx \frac{c_{i+1}^n - c_{i-1}^n}{2\,\Delta R} \tag{2.62}$$

$$\left.\frac{\partial^2 c}{\partial R^2}\right|_i^n \approx \frac{c_{i+1}^n - 2c_i^n + c_{i-1}^n}{(\Delta R)^2} \tag{2.63}$$

$$\left.\frac{\partial c}{\partial \tau}\right|_i^n \approx \frac{c_i^{n+1} - c_i^n}{\Delta \tau} \tag{2.64}$$

2.6.1 Boundary and initial conditions

In order to solve Equation 2.49, boundary conditions are needed for both sides of the computational domain (i.e., $r = 0$ & $r = r_s(t)$).

Because of the symmetry, the no flux condition is used for the droplet center, $r = 0$,

$$\frac{\partial C}{\partial r} = 0 \text{ at } r = 0 \tag{2.65}$$

which when normalized following the same normalization procedure reads as:

$$\frac{\partial c}{\partial R} = 0 \text{ at } R = 0 \tag{2.66}$$

This boundary condition is discretized using a first order forward differencing scheme as follows:

$$\left.\frac{\partial c}{\partial R}\right|_{R=0}^n \approx \frac{c_{i+1}^n - c_i^n}{\Delta R} \tag{2.67}$$

At the other end of the domain, $r = r_s(t)$, the sum of the diffusive flux and the convective flux due to the velocity of the receding droplet surface is zero since there is no flux of the solute across the droplet surface.

$$D\frac{\partial C}{\partial r} + C\frac{\partial r_s(t)}{\partial t} = 0 \text{ at } r = r_s(t) \tag{2.68}$$

Which can be normalized to give the following Robin boundary condition:

$$\frac{\partial c}{\partial R} - cPe = 0 \text{ at } R = 1 \tag{2.69}$$

Because of the high concentration gradient at the droplet surface, this boundary condition (Equation 2.69) is discretized using a sixth order backward differencing scheme.

$$\left.\frac{\partial c}{\partial R}\right|_{R=1}^{n} \approx \frac{49}{20}c_i^n - 6c_{i-1}^n + \frac{15}{2}c_{i-2}^n - \frac{20}{3}c_{i-3}^n + \frac{15}{4}c_{i-4}^n - \frac{6}{5}c_{i-5}^n + \frac{1}{6}c_{i-6}^n \tag{2.70}$$

The choice of a sixth order scheme gave accurate results for the tested range of Péclet numbers, Pe, and final evaporation time, τ_{final}. However, this choice was arbitrary and it might have been possible to use lower order schemes.

The initial condition is a uniform concentration profile.

$$c(R) = 1 \text{ at } \tau = 0 \tag{2.71}$$

The boundary and initial conditions for Equation 2.61 are given as follows:

$$\frac{\partial e}{\partial R} = 0 \text{ at } R = 0 \tag{2.72}$$

$$\frac{\partial e}{\partial R} - ePe = 0 \text{ at } R = 1 \tag{2.73}$$

$$e(R) = 1 \text{ at } \tau = 0 \tag{2.74}$$

2.6.2 Mass conservation

The total solute mass has to be checked every time step during the solution to ensure mass conservation. In the real physical domain of the problem, the domain is changing with time (i.e., $r_{\text{s}}(t)$) and mass can be simply calculated at each time step as follows:

$$M(t) = \iiint_{v(t)} C \, \mathrm{d}v \tag{2.75}$$

Where: C is the solute concentration.

But since the radial coordinate, r, is normalized, the computational domain is fixed and its volume does not reflect the actual volume of the droplet. An expression has to be derived to express the system mass in terms of the normalized coordinate, R.

Differential mass, $\mathrm{d}M$, can be calculated for an elemental volume, $\mathrm{d}v = r^2 \sin\theta \mathrm{d}r\mathrm{d}\theta\mathrm{d}\phi$, in spherical coordinates as follows:

$$\mathrm{d}M = C(r)\,\mathrm{d}v = C(r)\,r^2\,\sin\theta\,\mathrm{d}r\,\mathrm{d}\theta\,\mathrm{d}\phi \tag{2.76}$$

Since it is only the radial coordinate, r, that was normalized and not the other two coordinates (i.e., θ, ϕ), we can define the differential mass, $\mathrm{d}m$, as follows:

$$\mathrm{d}m = \frac{\mathrm{d}M}{\sin\theta \mathrm{d}\theta \mathrm{d}\phi} = C(r) r^2 \mathrm{d}r \tag{2.77}$$

$$m(t) = \int_0^{r_\mathrm{s}(t)} C(r) r^2 \mathrm{d}r = \int_0^1 C(R) R^2 r_\mathrm{s}^2(t) \mathrm{d}R r_\mathrm{s}(t) \tag{2.78}$$

$$m(t) = r_\mathrm{s}^3(t) \int_0^1 C(R) R^2 \mathrm{d}R \tag{2.79}$$

Equation 2.79 can be used to calculate the mass at any time, $m(t)$, using the concentration, $C(R)$, in the normalized coordinate , R. It can also be used to express the ratio of the mass at any time, $m(t)$, to the initial mass, m_o.

$$m_\mathrm{o} = r_\mathrm{o}^3 \int_0^1 C_\mathrm{o} R^2 \mathrm{d}R = r_\mathrm{o}^3 C_\mathrm{o} \int_0^1 R^2 \mathrm{d}R = \frac{r_\mathrm{o}^3 C_\mathrm{o}}{3} \tag{2.80}$$

$$\frac{m(t)}{m_\mathrm{o}} = 3 \left(\frac{r_\mathrm{s}}{r_\mathrm{o}} \right)^3 \int_0^1 \frac{C}{C_\mathrm{o}} R^2 \mathrm{d}R \tag{2.81}$$

$$\frac{m(\tau)}{m_\mathrm{o}} = 3(1-\tau)^{\frac{3}{2}} \int_0^1 \frac{C}{C_\mathrm{o}} R^2 \mathrm{d}R \tag{2.82}$$

$$\frac{m(\tau)}{m_\mathrm{o}} = 3(1-\tau)^{\frac{3}{2}} \int_0^1 c R^2 \mathrm{d}R \tag{2.83}$$

Where c is the normalized concentration, $\frac{C}{C_\mathrm{o}}$. Equation 2.83 can be integrated numerically using a zero order integration polynomial as follows:

$$\frac{m(\tau)}{m_\mathrm{o}} \approx 3(1-\tau)^{\frac{3}{2}} \sum_{i=0}^{N} c_i R_i^2 \Delta R \tag{2.84}$$

Where: $N+1$ is the number of grid points and ΔR is the grid spacing (i.e., $\Delta R = 1/N$).

Although the ratio given by Equation 2.83 should be unity if mass conservation is achieved, it will be slightly different than unity even if the solution is mass conservative. This is because the accuracy of the numerical integration given by Equation 2.84 depends on the number of grid points, $N+1$, and the integration method. To account for this error, Equation 2.84 has to be corrected to account for the accuracy of the numerical integration used.

We can start by calculating the ratio $\frac{m(0)}{m_\mathrm{o}}$ for the initial concentration profile, $c_\mathrm{o}(R) = 1$, at time $\tau = 0$ assuming a constant grid spacing, ΔR.

$$\frac{m(0)}{m_\mathrm{o}} \approx 3(1-\tau)^{\frac{3}{2}} \sum_{i=0}^{N} c_i R_i^2 \Delta R \tag{2.85}$$

$$\frac{m(0)}{m_\mathrm{o}} \approx 3(1-\tau)^{\frac{3}{2}} \Delta R c_\mathrm{o} \sum_{i=0}^{N} R_i^2 \tag{2.86}$$

$$R_i = i\Delta R \tag{2.87}$$

$$\frac{m(0)}{m_o} \approx 3(1-\tau)^{\frac{3}{2}}(\Delta R)^3 c_o \sum_{i=0}^{N} i^2 \tag{2.88}$$

$$\Delta R = \frac{1}{N} \tag{2.89}$$

$$\frac{m(0)}{m_o} \approx 3(1-\tau)^{\frac{3}{2}} \frac{1}{N^3} c_o \sum_{i=0}^{N} i^2 \tag{2.90}$$

$$\sum_{i=0}^{N} i^2 = \frac{N^3}{3} + \frac{N^2}{2} + \frac{N}{6} \tag{2.91}$$

$$\frac{m(0)}{m_o} \approx 1 + \frac{3}{2}\frac{1}{N} + \frac{1}{2}\frac{1}{N^2} \tag{2.92}$$

Equation 2.92 shows that the ratio calculated by Equation 2.84 is not unity and has to be corrected. The correction factor is a function of the number of grid points used, $N+1$. As the number of grid points increases, the ratio approaches unity.

2.6.3 Stability considerations

Using an explicit scheme (i.e., first order Euler) for time stepping puts an upper limit on the time step, $\Delta\tau$. The CFL condition can be used to calculate the maximum time step for a stable solution.

First, we need to know the velocity magnitude of the convective term. Equation 2.49 will be rewritten by grouping all terms with a first order spatial derivative together.

$$\frac{\partial c}{\partial \tau} = \frac{1}{2Pe(1-\tau)}\left(\frac{\partial^2 c}{\partial R^2}\right) + \frac{2 - R^2 Pe}{2(1-\tau)RPe}\left(\frac{\partial c}{\partial R}\right) \tag{2.93}$$

By comparing Equation 2.93 to a standard convection-diffusion equation we can write the velocity magnitude of the convective term as follows:

$$||\mathbf{v}_{\text{conv}}|| = \frac{2 - R^2 Pe}{2(1-\tau)RPe} \tag{2.94}$$

The velocity of the convective term depends on the radial coordinate, R, The Péclet number, Pe, and the time at the current time step, τ. Plotting Equation 2.94 shows that for a given Péclet number and time, τ, $||\mathbf{v}_{\text{conv}}||$ is maximum at the droplet center (Figure 2.1). Since the concentration of the first grid point is calculated from the no flux boundary condition (i.e., Equation 2.66), the solution of Equation 2.93 starts from the second grid point which has a radial coordinate $R = \Delta R$.

The maximum value for $||\mathbf{v}_{\text{conv}}||$ can then be calculated as follows:

$$||\mathbf{v}_{\text{conv,max}}|| = \frac{2 - (\Delta R)^2 Pe}{2(1-\tau)\Delta RPe} \tag{2.95}$$

Which can be conservatively approximated for small values of ΔR as follows:

$$||\mathbf{v}_{\text{conv,max}}|| \approx \frac{1}{(1-\tau)\Delta RPe} \tag{2.96}$$

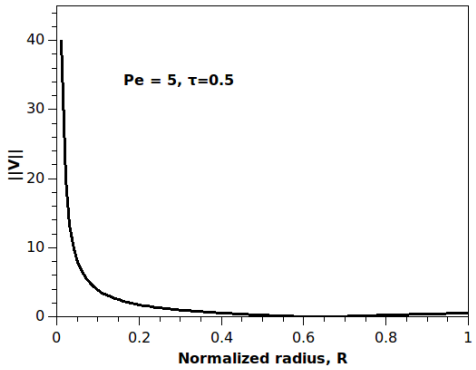

Figure 2.1: Magnitude of the convective term in Equation 2.49 for $Pe = 5$ & $\tau = 0.5$.

The CFL condition is given by:

$$\text{CFL} = \frac{||\mathbf{v}_{\text{conv,max}}||\Delta\tau}{\Delta R} \leq 1 \tag{2.97}$$

$$\text{CFL} = \frac{2 - (\Delta R)^2 Pe}{2(1-\tau)\Delta R Pe}\frac{\Delta\tau}{\Delta R} \leq 1 \tag{2.98}$$

$$\text{CFL} \approx \frac{\Delta\tau}{(1-\tau)(\Delta R)^2 Pe} \leq 1 \tag{2.99}$$

The maximum time step, $\Delta\tau$, can be approximated as follows:

$$\Delta\tau_{\max} \approx (1-\tau)(\Delta R)^2 Pe \tag{2.100}$$

Equation 2.100 shows that the maximum time step, $\Delta\tau$, is inversely proportional to the current time, τ. So there are two options for time stepping.

- Constant time step based on the final time, τ_{final}, at the end of the simulation (which will give the most conservative value of $\Delta\tau_{\max}$).
- Adaptive time step based on the time at the current time step.

The first option is easier to implement but results in an unnecessarily small time step during the early stage of evaporation. The final time has also to be determined in advance to avoid any instability at the later stages of the simulation.

The second option offers a suitable time step according to the current state of the simulation without imposing an upper limit on the final time. This is computationally more efficient than using a constant time step, as the ratio between the maximum stable time step at the beginning and at the end of the simulation can be huge.

The ratio between the maximum stable time steps, if adaptive time stepping is used, can be calculated as follows:

$$\Delta\tau_{\max} \propto 1 - \tau \tag{2.101}$$

$$\frac{\Delta\tau_1}{\Delta\tau_{N_\tau}} \approx \frac{1-\tau_1}{1-\tau_{N_\tau}} \tag{2.102}$$

Where: $\Delta\tau_1$ and $\Delta\tau_{N_\tau}$ are the maximum stable initial and final time steps respectively and τ_1 and τ_{N_τ} are the times of the first and last time points that needs to be resolved respectively. For example, if $\tau_1 = 0.01$ and $\tau_{N_\tau} = 0.99$ then the ratio between the two time steps is 99. This can be shown be plotting Equation 2.100 for a specific Pe and ΔR as a function of the normalized time, τ (Figure 2.2).

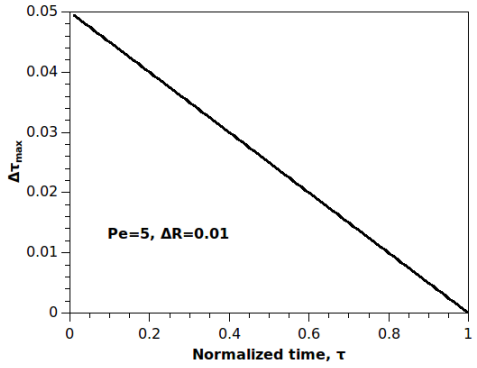

Figure 2.2: Maximum stable time step, $\Delta\tau_{\max}$, for $Pe = 5$ & $\Delta R = 0.01$.

The main drawback of using an adaptive time step is that the time points of the results are not known ahead of the simulation and are irregular. So the solution at a certain time cannot be obtained. As a first step toward the solution of Equation 2.49 a constant time step will be used.

It has to be noted that the CFL condition provides a rough estimate of the maximum time step that can be used for a stable solution. A more accurate estimate can be obtained by using other stability analysis techniques like the matrix stability analysis or von Neumann stability analysis [Moin, 2010].

2.7 Results

The evolution of the concentration profile described by Equation 2.49 is a function of the Péclet number, Pe, only. Equation 2.49 was solved for a wide range of Pe numbers (0.1 - 200). The evolution of the concentration profile and surface enrichment suggests the splitting of that range into three regimes as shown in Figure 2.3. As the Péclet number increases, it takes more time to reach the steady state value for surface enrichment predicted by Equation 2.30.

2.7.1 How long does it take to reach the asymptotic state ?

Since a steady state value for $E(\tau)$ is only reached when the concentration profile reaches an asymptotic state, subsection 2.4.3, the evolution of $E(\tau)$ with time can

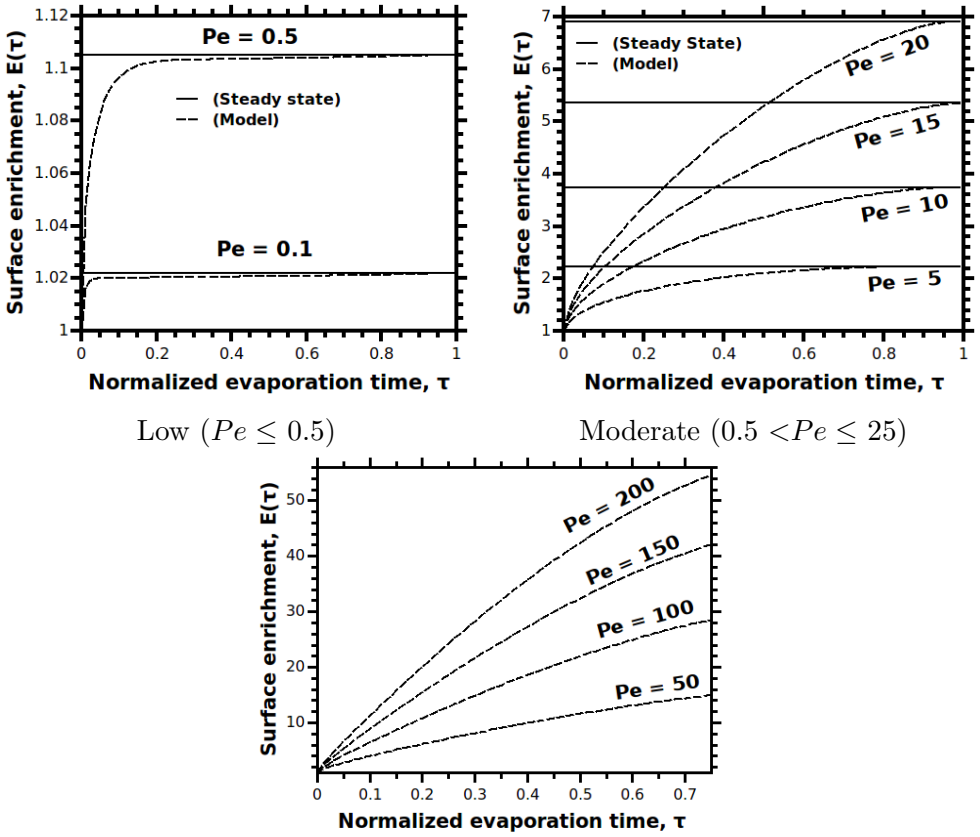

Low ($Pe \leq 0.5$) Moderate ($0.5 < Pe \leq 25$)

High ($25 < Pe \leq 200$)

Figure 2.3: Evolution of the surface enrichment for different Péclet number regimes.

be used to estimate the time needed to reach the asymptotic state.

It is hard to answer the question explained in subsection 2.4.4 just by looking at the results for different Pe numbers given in Figure 2.3. We have to define a criterion for $E(\tau)$ to reach a steady state. The first option is to calculate the time needed for $E(\tau)$ to reach 95 % (or any other percentage) of the steady state value given by Equation 2.30 or Equation 2.31. In this case Figure 2.3 can be used to calculate this value for each Pe number to decide what is the limiting maximum Pe number for the concentration profile to reach an asymptotic state within 95 % (or any other percentage) of the droplet lifetime. Using Figure 2.3 we can predict this number to be less than 10.

A second, more accurate, option is to calculate the time needed for $\frac{\mathrm{d}E(\tau)}{\mathrm{d}\tau}$ to reach a predefined tolerance, ϵ, small enough to reflect the variation of E with τ as it approaches a steady state value. In this case we need to calculate $\frac{\mathrm{d}E(\tau)}{\mathrm{d}\tau}$ for different Pe numbers.

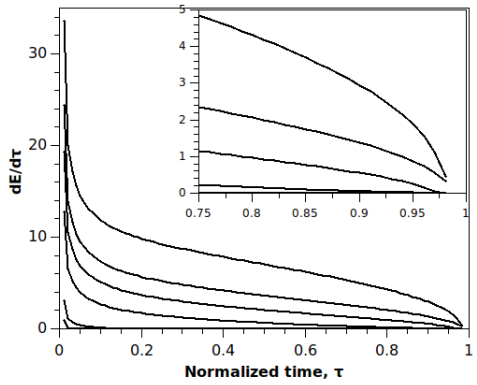

Figure 2.4: Traces top to bottom are $\frac{dE(\tau)}{d\tau}$ for: Pe = 25, 15, 10, 5, 0.5 and 0.1 respectively and Pe = 25, 15, 10 and 5 respectively (inset graph)

Figure 2.4 shows $\frac{dE(\tau)}{d\tau}$ for different Pe numbers. It is clear that for any Pe number above 5, the surface enrichment does not reach the steady state value within the droplet lifetime. Of course this number will depend on the tolerance, ϵ.

2.7.2 Shell composition

Although we have answered the question of *"How long does it take for the concentration profile in an evaporating solution droplet to reach an asymptotic state ?"* asked in subsection 2.4.4, subsection 2.4.1 shows that the shell composition is determined by the surface enrichment, $E(\tau)$, at the time of shell formation whether it is the steady state value or not. It is important to calculate the surface enrichment for any Pe number at any time during the evaporation process.

The solution of Equation 2.49 does not tell us anything about the shell formation, however if we solve Equation 2.51 we can calculate the time needed for the surface saturation ratio, s, to reach the value needed to trigger shell formation. This is the time at which the shell starts to form. Then Figure 2.3 can be used to determine the value of E at that time which gives the shell composition.

2.7.3 How to use the results

As pointed out in the last two sections (subsection 2.7.1 and subsection 2.7.2) both figures (Figure 2.3 and Figure 2.4) can be used to determine the maximum limiting Pe number and the shell composition. However, Equation 2.49 has to be solved for other values of the Pe number not given in the two figures. An easier alternative is to fit the model results with an analytical equation that is easier to use.

Pe <0.5 (Low)

For Pe numbers less than 0.5, the initial surface enrichment (i.e., $E(0) = 1$) is more than 90 % of the steady state value, E_{ss}, given by Equation 2.30 or Equation 2.31. 95 % of E_{ss} is reached in less than 2 % of the droplet lifetime, τ_D, (i.e., τ <0.02). While 99 % of E_{ss} is reached in less than 9 % of the droplet lifetime, τ_D, (i.e., τ <0.09). So using the steady state value , E_{ss}, does not introduce a significant error.

$0.5 \leq Pe \leq 25$ (Moderate)

Looking at Figure 2.3, we can fit the evolution of $E(\tau)$ with an asymptotic function of the following form.

$$E(\tau) = A - Be^{-n\tau} \tag{2.103}$$

From Figure 2.3 it is clear that $E(\tau)$ reaches the steady state value, E_{ss}, before the end of the droplet lifetime. The two constants A and B can then be calculated to satisfy the two conditions $E(0) = 1$ and $E(1) = E_{ss}$. Upon substitution, Equation 2.103 takes the following form.

$$E(\tau) \approx \frac{E_{ss} - e^{-n}}{1 - e^{-n}} - \frac{E_{ss} - 1}{1 - e^{-n}} e^{-n\tau} \tag{2.104}$$

n determines the growth rate of $E(\tau)$ for different Pe numbers and is calculated by fitting the model results.

$$n(Pe) = 15Pe^{-0.7} \quad \text{for } 0.5 \leq Pe \leq 25 \tag{2.105}$$

Equation 2.104 and Equation 2.105 are valid for Pe numbers from 0.5 up to 25. The error of Equation 2.104 compared to the numerical model results is less than 8 % for $\tau > 0.2$.

The time derivative of $E(\tau)$ can also be calculated from Equation 2.104 as follows:

$$\frac{\mathrm{d}E(\tau)}{\mathrm{d}\tau} = \frac{n\,(E_{ss} - 1)}{1 - e^{-n}} e^{-n\tau} \tag{2.106}$$

Evaluating Equation 2.106 at $\tau = 1$ can be used to calculate the maximum Pe number for surface enrichment to reach a steady state condition.

$$\left.\frac{\mathrm{d}E(\tau)}{\mathrm{d}\tau}\right|_{\tau=1} = \frac{n\,(E_{ss} - 1)}{1 - e^{-n}} e^{-n} \tag{2.107}$$

$$\frac{n\,(E_{ss} - 1)}{1 - e^{-n}} e^{-n} = \epsilon \tag{2.108}$$

Equation 2.108 can be solved iteratively for a given value of ϵ to calculate the maximum Pe number that allows the concentration profile to reach the asymptotic state within the droplet lifetime.

ϵ is a predetermined value small enough to reflect the temporal change of surface enrichment, $E(\tau)$, at the asymptotic state (i.e., ideally it should be zero).

$25 < Pe \leq 200$ (High)

Due to the higher gradients at high Pe numbers at the droplet surface, the concentration profiles and surface enrichment were calculated up to 75 % of the droplet lifetime, τ_D, (i.e., $\tau_{final} = 0.75$) for Pe numbers more than 25.

The same form of Equation 2.103 can be used to fit the results for the evolution of surface enrichment, $E(\tau)$. The two constants A and B can be calculated to satisfy the two conditions $E(0) = 1$ and $E(0.75) = E_{75}$, where E_{75} is the surface entrainment at 75 % of the droplet lifetime, τ_D.

$$E(\tau) = A - Be^{-\frac{4}{3}n\tau} \tag{2.109}$$

$$E(\tau) \approx \frac{E_{75} - e^{-n}}{1 - e^{-n}} - \frac{E_{75} - 1}{1 - e^{-n}} e^{-\frac{4}{3}n\tau} \tag{2.110}$$

n determines the growth rate of $E(\tau)$ for different Pe numbers and is given by:

$$n(Pe) = 0.95 \quad \text{for } 25 < Pe \leq 200 \tag{2.111}$$

While E_{75} is give by:

$$E_{75} = 0.858 E_{ss} \quad \text{for } 25 < Pe \leq 200 \tag{2.112}$$

The error of Equation 2.110 compared to the numerical model results is less than 10 % for $\tau > 0.2$.

2.7.4 Steady state surface enrichment, E_{ss}, at high Péclet numbers

In subsection 2.7.3 the model results were recast in simple analytical forms to make them easy to use without the need for code development. However, subsection 2.7.3 shows that the steady state value of surface enrichment, E_{ss}, is still needed to calculate the transient value, $E(\tau)$. E_{ss} can be calculated using Equation 2.29 by numerical integration of Equation 2.30 for any Péclet number. Equation 2.30 was obtained by fitting the numerical results of integration for Péclet numbers less than 20 [Vehring, 2008; Vehring et al., 2007]. This approach can not be used to derive a similar relation for larger Péclet numbers because the computational demand for this integration increases rapidly with increasing Péclet number.

This is because the integrand function becomes very steep near the droplet surface which necessitates the use of a large number of points for integration and double precision calculation. Instead, asymptotic analysis was used to derive an approximation for E_{ss} which was then corrected with the numerical integration results.

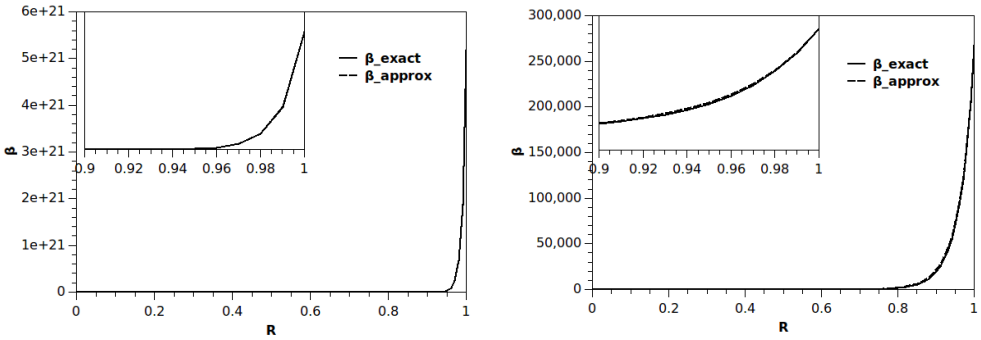

$Pe = 100$ $Pe = 25$

Figure 2.5: β (Equation 2.113) vs. β_{approx} (Equation 2.114) at high Pe numbers.

For very high Pe numbers (i.e., $Pe \geq 100$) an approximation can be made to give an analytical solution for β. In this range of Pe numbers the integrand in

Equation 2.29 is mainly dominated by the exponential part (i.e., $\exp\left(\frac{Pe}{2}R^2\right)$). The integrand function is also very steep near the droplet surface (i.e., $R = 1$). The value of β is mainly determined by the part of the integrand near the interface (i.e., $R \sim 1$) and in this range we can replace R^2 by R in the non-exponential part of the integrand without introducing a significant error (Figure 2.5). This modification allows us to obtain an analytical solution for β and hence E_{ss} as follows:

$$\beta = \int_0^1 R^2 \exp\left[\left(\frac{Pe}{2}\right)R^2\right] \mathrm{d}R \tag{2.113}$$

$$\beta \approx \int_0^1 R \exp\left[\left(\frac{Pe}{2}\right)R^2\right] \mathrm{d}R \tag{2.114}$$

$$\beta \approx \frac{1}{Pe}\int_0^1 PeR \exp\left[\left(\frac{Pe}{2}\right)R^2\right] \mathrm{d}R \tag{2.115}$$

$$\beta \approx \frac{1}{Pe}\left[\exp\left(\frac{Pe}{2}R^2\right)\right]_0^1 \tag{2.116}$$

$$\beta \approx \frac{\exp\left(\frac{Pe}{2}\right) - 1}{Pe} \tag{2.117}$$

$$E_{\mathrm{ss}} = \frac{c_{\mathrm{s}}}{c_{\mathrm{m}}} = \frac{1}{3\beta}\exp\frac{Pe}{2} \tag{2.118}$$

$$E_{\mathrm{ss}} \approx \frac{Pe}{3}\frac{\exp\left(\frac{Pe}{2}\right)}{\exp\left(\frac{Pe}{2}\right) - 1} \tag{2.119}$$

The second term on the right hand side of Equation 2.119 approaches unity for high Péclet numbers (i.e., 1.000045402 for $Pe = 20$) and hence can be dropped.

$$E_{\mathrm{ss}} \approx \frac{Pe}{3} \tag{2.120}$$

Equation 2.120 is accurate within 1% for $Pe \geq 100$.

A correction can be added to Equation 2.120 to extends its range of usability and enhance its accuracy. For $Pe \geq 20$ the following approximation can be used.

$$E_{\mathrm{ss}} = \frac{c_{\mathrm{s}}}{c_{\mathrm{m}}} \approx \frac{Pe}{3} + 0.363 \tag{2.121}$$

The accuracy of Equation 2.121 can be demonstrated by plotting the steady state surface enrichment, E_{ss}, as calculated from Equation 2.121 compared to the one obtained from Equation 2.29 by the numerical integration of Equation 2.30 as shown by Figure 2.6. Equation 2.121 is accurate within 0.15% for $Pe \geq 20$.

2.7.5 Transient surface enrichment, $E(\tau)$, at high Péclet numbers

Equation 2.110 for the high Péclet number regime depends on two parameters. The first is n which is Pe number independent (Equation 2.111), while the second E_{75} is linear in E_{ss} (Equation 2.112) which is in turn a function of the Pe number (Equation 2.29). However, Equation 2.121 shows that E_{75} is linear in Pe for the high Pe number regime. It can be shown that the evolution of the surface enrichment $E(\tau)$

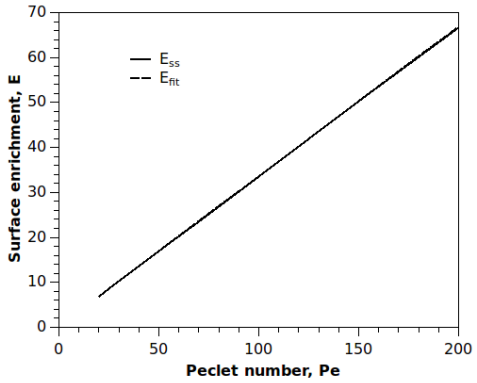

Figure 2.6: Steady state surface enrichment, E_{ss}: Gardner's solution (Equation 2.29) vs. the proposed fitting equation (Equation 2.121).

is linear in Pe and the ratio $\frac{E(\tau)}{E_{ss}}$ is Pe independent for the high Pe number regime.

Equation 2.110 can be written as follows:

$$E(\tau) = \frac{1}{c_1}\left(E_{75} - c_3 - (E_{75} - 1)e^{c_2\tau}\right) \tag{2.122}$$

Where:
$c_1 = 1 - e^{-n} = 1 - e^{-0.95} = 0.613$
$c_2 = -\frac{4}{3}n = -\frac{4}{3} \times 0.95 = -1.267$
$c_3 = e^{-n} = e^{-0.95} = 0.387$

Using Equation 2.120 as an approximation for E_{ss}, $\frac{E(\tau)}{E_{ss}}$ can be written as follows:

$$\frac{E(\tau)}{E_{ss}} \approx \frac{1}{c_1}\frac{3}{Pe}\left(c_4 Pe - c_3 - (c_4 Pe - 1)e^{c_2\tau}\right) \tag{2.123}$$

$$\frac{E(\tau)}{E_{ss}} \approx \frac{1}{c_1}\left(3c_4 - 3\frac{c_3}{Pe} - \left[3c_4 - 3\frac{1}{Pe}\right]e^{c_2\tau}\right) \tag{2.124}$$

Where:
$c_4 = 0.858 \times \frac{1}{3} = 0.286$

For high Pe number, all the $\frac{1}{Pe}$ terms in Equation 2.124 can be dropped.

$$\frac{E(\tau)}{E_{ss}} \approx \frac{1}{c_1}\left(3c_4 - 3c_4 e^{c_2\tau}\right) \tag{2.125}$$

$$\frac{E(\tau)}{E_{ss}} \approx 3\frac{c_4}{c_1}\left(1 - e^{c_2\tau}\right) \tag{2.126}$$

$$\frac{E(\tau)}{E_{ss}} \approx 1.4\left(1 - e^{-1.267\tau}\right) \tag{2.127}$$

Equation 2.127 shows that the evolution of $\frac{E(\tau)}{E_{ss}}$ is Pe independent and can be used for any Pe number in the high Pe number regime. This result can be verified by the excellent matching between the the normalized surface enrichment, $\frac{E(\tau)}{E_{ss}}$, as calculated by the model and that predicted by Equation 2.127 for different Pe numbers as shown in Figure 2.7.

Equation 2.127 can be recast in a more usable form as follows:

$$E(Pe,\tau) \approx \left[\frac{Pe}{2} - \frac{1}{9}\right] - \left[\frac{Pe}{2} - \frac{10}{9}\right] e^{-\frac{6}{5}\tau} \tag{2.128}$$

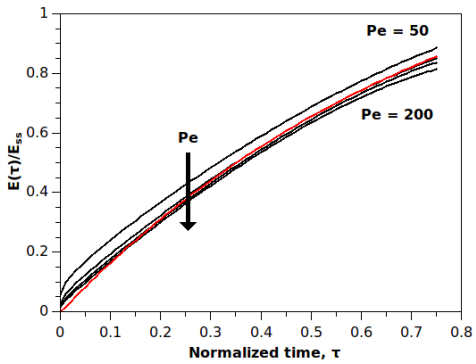

Figure 2.7: Traces top to bottom are normalized surface enrichment, $\frac{E(\tau)}{E_{ss}}$, for Pe = 50, 100, 150 and 200 respectively. Black: Model results, Red: Equation 2.127.

2.7.6 Characteristic times

Different characteristic times suggested by Vehring [2008] can be calculated using $E(\tau)$ instead of E_{ss}. Characteristic times normalized by the droplet drying time, τ_D, are given as follows (see Equation 2.32, Equation 2.34 and Equation 2.36):

$$\tau_{sat} = 1 - (s_o E(\tau_{sat}))^{\frac{2}{3}} \tag{2.129}$$

$$\tau_t = 1 - (p_o E(\tau_t))^{\frac{2}{3}} \tag{2.130}$$

$$\tau_p = 1 - \tau_{sat} = (s_o E(\tau_{sat}))^{\frac{2}{3}} \tag{2.131}$$

However, in this case these equations have to be solved iteratively.

Equation 2.129 points again to the same important factor that has to be considered in addition to the Pe number, the initial saturation, s_o [subsection 2.4.1]. Equation 2.129 shows that the time to reach saturation at the droplet surface depends on the product of s_o and $E(\tau)$. These variables are functions of both the initial saturation and the Pe number respectively.

τ_{sat} is the main characteristic time that affects most of the final dry particle properties as will be shown in the following sections. It has to be noticed that τ_{sat} is used for components that form crystalline shells while τ_{t} is used for amorphous shells [Vehring, 2008].

In case of a variable evaporation rate, the droplet diameter at time t is calculated as following for a known evaporation rate, $\kappa(t)$.

$$d^2(t) = d_{\mathrm{o}}^2 - \int_0^{\mathrm{t}} \kappa(\tilde{t})\,\mathrm{d}\tilde{t} \tag{2.132}$$

While the droplet lifetime, τ_{D}, can be calculated by solving the following equation .

$$d_{\mathrm{o}}^2 = \int_0^{\tau_{\mathrm{D}}} \kappa(t)\,\mathrm{d}t \tag{2.133}$$

In this case, the mean normalized concentration, c_{m}, and the saturation time, t_{sat}, can be calculated as follows:

$$c_{\mathrm{m}} = \frac{d_{\mathrm{o}}^2}{\left[d_{\mathrm{o}}^2 - \int_0^{\mathrm{t}} \kappa(\tilde{t})\,\mathrm{d}\tilde{t}\right]^{\frac{3}{2}}} \tag{2.134}$$

$$\int_0^{t_{\mathrm{sat}}} \frac{\kappa(t)}{d_{\mathrm{o}}^2}\mathrm{d}t = 1 - \left[s_{\mathrm{o}} E(t_{\mathrm{sat}})\right]^{\frac{2}{3}} \tag{2.135}$$

2.7.7 Dry particle properties

Several dry particle properties can be calculated. Some of these properties can be calculated using the classical particle formation theory [Vehring, 2008; Vehring et al., 2007] as a first approximation. However, the results of this theory become increasingly inaccurate at higher Pe numbers and initial saturation, as will be shown later.

For single component droplets, the shell formation time, τ_{sh}, equals the saturation time, τ_{sat}, (or the time to reach true density,τ_{t} for amorphous shells). For multi-component droplets, the shell formation time, τ_{sh}, is equal to the saturation time, $\tau_{\mathrm{sat},i}$, for the component i that reaches saturation first.

$$\tau_{\mathrm{sh}} = \min(\tau_{\mathrm{sat},i}) \text{ for crystalline components} \tag{2.136}$$

$$\tau_{\mathrm{sh}} = \min(\tau_{\mathrm{t},i}) \text{ for amorphous components} \tag{2.137}$$

Dry particle size

The minimum concentration required to initialize shell formation is referred to as the critical supersaturation, CSS. Generally CSS is hard to calculate numerically and it is measured experimentally for different solutes under different evaporation conditions. CSS also depends on the droplet temperature at the onset of shell formation. Several researchers used different methods to estimate the value of CSS [Leong, 1987; Tang and Munkelwitz, 1984; Brechtel and Kreidenweis, 2000a,b].

Based on the evolution of $E(\tau)$ and an estimate of the minimum concentration to initialize shell formation, the dry particle volume equivalent diameter, d_{v}, can by calculated as follows:

$$d_{\mathrm{v}} = d_{\mathrm{o}} \sqrt{1 - \tau_{\mathrm{sh}}} \tag{2.138}$$

Under the following two assumptions:

- No shrinkage of the particle occurs once a shell is formed.
- No folding or buckling occurs for the formed shell.

The classical particle formation theory calculates the dry particle volume equivalent diameter, d_{v}, based on a simple mass balance of the solute mass without taking radial concentration profiles into account.

$$d_{\mathrm{v}} = d_{\mathrm{o}} \sqrt[3]{\frac{C_{\mathrm{f}}}{\rho_{\mathrm{p}}}} \tag{2.139}$$

Where: C_{f} is the feed concentration, $C_{\mathrm{f}} = \sum_i C_{\mathrm{o},i}$.

The dependence of the dry particle size on the drying conditions like the evaporation rate, κ, and the solute properties like diffusivity, D, is included through an estimate of the dry particle density, ρ_{p}.

Density

Once the dry particle size is calculated, the true particle density, ρ_{p}, can be calculated as follows:

$$\rho_{\mathrm{p}} = C_{\mathrm{f}} \left[\frac{d_{\mathrm{o}}}{d_{\mathrm{v}}}\right]^3 \tag{2.140}$$

The classical particle formation theory does not provide a means to calculate the dry particle density, which is a logical consequence of ignoring the dependence of the dry particle morphology on the drying conditions and solute properties.

Using the steady state value of surface enrichment, E_{ss}, instead of the transient value, $E(\tau)$, has the drawback of making the particle density independent of the initial concentration for a given Péclet number. This can be proved as follows:

For a constant surface enrichment, E_{ss}, the normalized saturation time, τ_{sat}, can be written as follows (Equation 2.129 & Equation 2.33):

$$\tau_{\mathrm{sat}} = 1 - \left(\frac{C_{\mathrm{o}}}{C_{\mathrm{sol}}}\, E_{\mathrm{ss}}\right)^{\frac{2}{3}} \tag{2.141}$$

Then the dry particle diameter, d_{v}, can be written as follows (Equation 2.141 & Equation 2.139):

$$\sqrt{1 - \tau_{\mathrm{sat}}} = \left(\frac{C_{\mathrm{o}}}{C_{\mathrm{sol}}}\, E_{\mathrm{ss}}\right)^{\frac{1}{3}} \tag{2.142}$$

$$d_{\mathrm{v}} = d_{\mathrm{o}} \sqrt[3]{\frac{C_{\mathrm{o}}}{C_{\mathrm{sol}}}\, E_{\mathrm{ss}}} \tag{2.143}$$

For a single component particle, the particle density can be written as follows (Equation 2.140):

$$\rho_{\mathrm{p}} = C_{\mathrm{o}} \left[\frac{d_{\mathrm{o}}}{d_{\mathrm{v}}}\right]^3 \tag{2.144}$$

Substituting Equation 2.143 in Equation 2.144 gives the particle density, ρ_{p}, as follows:

$$\left[\frac{d_{\mathrm{o}}}{d_{\mathrm{v}}}\right]^3 = \frac{C_{\mathrm{sol}}}{C_{\mathrm{o}}\, E_{\mathrm{ss}}} \tag{2.145}$$

$$\rho_{\mathrm{p}} = C_{\mathrm{o}} \frac{C_{\mathrm{sol}}}{C_{\mathrm{o}}\, E_{\mathrm{ss}}} \tag{2.146}$$

$$\rho_{\mathrm{p}} = \frac{C_{\mathrm{sol}}}{E_{\mathrm{ss}}} \text{ for crystalline components} \tag{2.147}$$

$$\rho_{\mathrm{p}} = \frac{\rho_{\mathrm{t}}}{E_{\mathrm{ss}}} \text{ for amorphous components} \tag{2.148}$$

Equation 2.147 and Equation 2.148 show that for a given Péclet number, Pe, the particle density, ρ_{p}, is independent of the initial concentration, C_{o}.

Equation 2.147 and Equation 2.148 is a good approximation for particle density, ρ_{p}, at low Péclet numbers, Pe, or low initial saturation ratios, s_{o}.

Aerodynamic diameter

The aerodynamic diameter is calculated based on the known particle density and volume equivalent diameter.

$$d_{\mathrm{a}} = d_{\mathrm{v}} \sqrt{\frac{\rho_{\mathrm{p}}}{\rho^*} \frac{C_{\mathrm{cs}}(d_{\mathrm{v}})}{C_{\mathrm{cs}}(d_{\mathrm{a}})} \frac{1}{\lambda_{\mathrm{s}}}} \tag{2.149}$$

Where: ρ^* is a reference unit density (1000 kg/m^3) , $C_{\mathrm{cs}}(d_{\mathrm{v}})$ and $C_{\mathrm{cs}}(d_{\mathrm{a}})$ are the slip correction factors [Davis, 2006; DeCarlo et al., 2004] for the volume equivalent diameter and aerodynamic diameter, respectively, and λ_{s} is the dynamic shape factor [DeCarlo et al., 2004] of the dry particle. For spherical particles the dynamic shape factor is unity.

Shell thickness

For droplets evaporating at high Pe numbers (section 2.7.3), the dry particle shell thickness can be calculated. When the shell forms, the outer particle diameter is assumed to be the fixed volume equivalent diameter, d_{v}, and it is assumed that the remaining solvent evaporates through the formed shell with a subsequent receding of the internal interface from the droplet center towards its outer shell.

Evaporation at high Pe numbers results in very steep concentration profiles near the droplet surface with most of the droplet remaining close to the initial concentration (Figure 2.8). Hence, we can assume that at the end of the evaporation process the whole solute mass will be concentrated in a thin shell. If the average shell density, ρ_{sh}, can be estimated, e.g., by the true density of the solute, ρ_{t}, a simple mass balance yields the internal void diameter, d_{sh}.

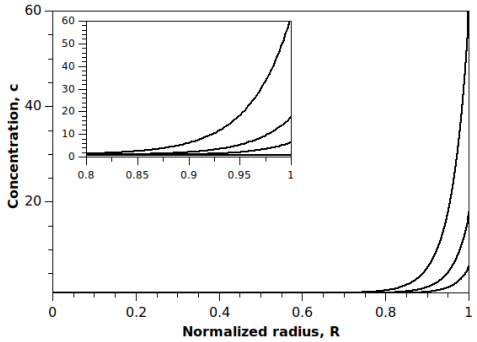

Figure 2.8: Traces top to bottom are concentration profiles for $Pe = 25$, at $\tau = 0.75$, 0.5, 0.25 and 0 respectively.

$$\frac{\pi}{6} C_{\mathrm{f}} d_{\mathrm{o}}^3 = \frac{\pi}{6} \rho_{\mathrm{sh}} \left[d_{\mathrm{v}}^3 - d_{\mathrm{sh}}^3 \right] \tag{2.150}$$

$$\frac{d_{\mathrm{sh}}}{d_{\mathrm{v}}} = \sqrt[3]{1 - \frac{C_{\mathrm{f}}}{\rho_{\mathrm{sh}}} \left[\frac{d_{\mathrm{o}}}{d_{\mathrm{v}}} \right]^3} \tag{2.151}$$

Substituting Equation 2.140 in Equation 2.151 gives d_{sh} as a function of the particle to shell density ratio.

$$\frac{d_{\mathrm{sh}}}{d_{\mathrm{v}}} = \sqrt[3]{1 - \frac{\rho_{\mathrm{p}}}{\rho_{\mathrm{sh}}}} \tag{2.152}$$

For multi-component particles ρ_{sh} can be estimated as follows:

$$\rho_{\mathrm{sh}} = \frac{1}{\sum\limits_i \frac{Y_i}{\rho_i}} \tag{2.153}$$

Where: Y_i is the mass fraction of component i and ρ_i is the solubility of component i (C_{sol}) for crystalline components or the true density of component i (ρ_{t}) for amorphous components.

For solid particles without a void, particle and shell density are the same which gives an internal particle diameter of zero using Equation 2.152, as expected. For hollow particles, particle density is always lower than the shell density which gives a value less the unity for the ratio between the internal particle diameter and the volume equivalent diameter.

For droplets containing suspended solid particles the shell density can be calculated as follows:

$$\rho_{\mathrm{sh}} = \rho_{\mathrm{t}} P \tag{2.154}$$

Where ρ_{t} is the true density of the used suspended particles and P is the packing factor.

The packing factor depends on the diameter distribution of the suspended particles. The wider the distribution the higher the packing factor [Chen et al., 2011]. For the case of narrow size distributions, a packing factor of 63.1 % has been reported for monodisperse particles [Chen et al., 2011].

It has to be noted that for some cases, especially for high Pe numbers and at the later stages of the droplet lifetime, the model results cannot be used since the concentration profiles at the surface of the droplet will be so steep to the point of having a large concentration gradient across a length scale comparable to the mean free path of the solute molecules. In this case, the continuum assumption breaks down and the proposed approach cannot be used.

2.8 Conclusions

The new model presented in this chapter extends the range of usability of the classical particle formation theory [Vehring, 2008; Vehring et al., 2007] to high initial saturation ratios and large Péclet numbers. Improved predictive ability was obtained by removing one of the limiting assumptions of the classical particle formation theory by taking the transient nature of the solute concentration profiles into account.

The additional accuracy was achieved without compromising usability for the formulator. The numerical model results were recast in a simple analytical form to facilitate easy use, especially in the preliminary stage of formulations design, without the need for numerical model development. The model allows prediction of many important properties of the resulting dry particle and thus enables a mechanistic procedure to the design of multi-component layered particles with specific properties. Spray drying process parameters and the formulation composition can be largely determined *a priori* and most parameters need not be determined empirically, which may provide very significant time savings in the early development process.

For a specific formulation design, the procedure of predicting the final dry particle properties can be summarized as follows:

1. Based on the range of possible drying process parameters, the available range of evaporation rates can be derived.

2. The solute diffusivities are then used to calculate the Péclet numbers for all components (Equation 2.9).

3. Using the appropriate equation for the Péclet number range, the surface enrichment for each component can be determined at each point during the droplet lifetime (Equation 2.31, Equation 2.104 or Equation 2.110).

4. By estimating the critical concentration, a characteristic time to reach supersaturation, $\tau_{\mathrm{sat},i}$ can be derived for each component (Equation 2.129). The

shortest time τ_{sh} indicates the component that likely forms a shell first and will be found on the outside of the dry particle.

5. The volume equivalent diameter of the particle can now be approximated by determining the particle diameter at the onset of shell formation (Equation 2.138).

6. Particle density (Equation 2.140), aerodynamic diameter (Equation 2.149) and shell thickness (Equation 2.151 and Equation 2.152) can now be derived.

7. Information about the radial composition of the dry particles can be inferred by calculating the radial concentration profiles for each component at the onset of shell formation, τ_{sh} (Equation 2.49).

8. Components' mass fractions, Y_i, at any position, R, can then be calculated, $Y_i = \frac{c_i(R,\tau_{\mathrm{sh}})}{\sum_i c_i(R,\tau_{\mathrm{sh}})}$.

Chapter 3

Diffusion controlled formation of microparticles: Validation & Results

3.1 Introduction

The results of the new particle formation theory proposed in chapter 2 will be validated in the current chapter. The chapter starts with comparing the model results to the analytical solution given by Gardner [Gardner, 1965]. Then the model results will be compared to experimental and numerical results from literature, highlighting its ability in predicting different dry particle properties and emphasizing the lack of accuracy of the classical particle formation theory for some particle formation conditions. The model results will then be verified against the experimental results generated by the single droplet setup.

3.2 Analytical Validation

Since the present model takes the transient nature of the concentration profiles into account as opposed to the asymptotic state solution given by Gardner [Gardner, 1965], the model results should match Gardner's solution for the cases where this asymptotic state is reached within the droplet lifetime as pointed out in chapter 2.

Parts of this chapter has been published in the following publications.

1. M.A. Boraey and R. Vehring. Diffusion controlled formation of microparticles. *Journal of Aerosol Science*, 67:131–143, 2014
2. M. Boraey, A. Baldelli, and R. Vehring. Theoretical and experimental investigation of particle formation from evaporating microdroplets. In *AAAR 32nd Annual Conference, American Association for Aerosol Research, Portland, Oregon, USA, September 30 - October 4*, 2013a
3. A.L. Feng, M.A. Boraey, M.A. Gwin, P.R. Finlay, P.J. Kuehl, and R. Vehring. Mechanistic models facilitate efficient development of leucine containing microparticles for pulmonary drug delivery. *International Journal of Pharmaceutics*, 409(1-2):156–163, 2011
4. M.A. Boraey, S. Matinkhoo, and R. Vehring. A new time and cost effective approach for the development of microparticles for pulmonary drug delivery. In *RDD Europe, Respiratory Drug Delivery.*, 2011

3.2.1 Asymptotic concentration profiles

The normalized concentration, $\frac{c(R)}{c_m}$, can be calculated using Gardner's solution as follows (see Appendix A):

$$\frac{c(R)}{c_m} = \frac{1}{3\beta} \exp\left[\left(\frac{Pe}{2}\right) R^2\right] \tag{3.1}$$

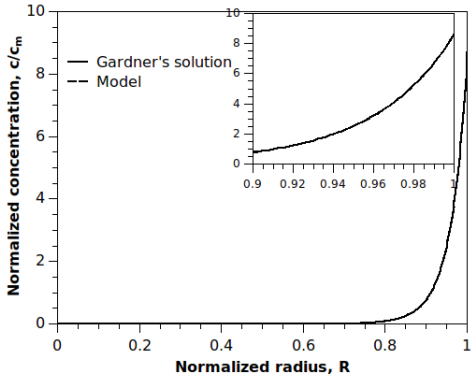

Figure 3.1: Normalized concentration profiles: Model results at $\tau = 0.99$ vs. Asymptotic state solution for $Pe = 25$.

The model results for the normalized concentration, $\frac{c(R)}{c_m}$, at $\tau = 0.99$ is compared against the asymptotic state solution given by Equation 3.1 for $Pe = 25$ as shown in Figure 3.1.

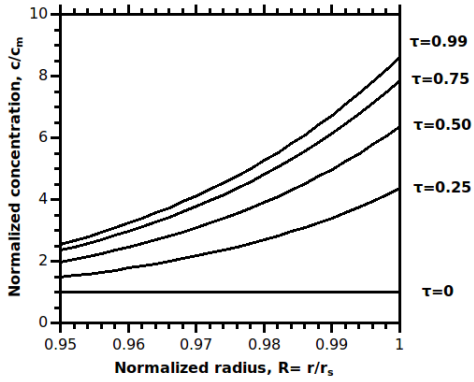

Figure 3.2: Normalized transient concentration profiles: Model results for $Pe = 25$.

The perfect agreement between the results confirms the ability of the new model to predict the asymptotic state solution in addition to the transient concentration profiles, as shown in Figure 3.2.

3.2.2 Steady state surface enrichment

It was shown that the asymptotic state solution for the concentration profiles leads to a steady state value for surface enrichment, E_{ss}. In this section, the steady state value predicted using Gardner's solution is compared against the transient value for surface enrichment, $E(\tau)$, at $\tau = 0.99$. Good agreement can be seen in Figure 3.3.

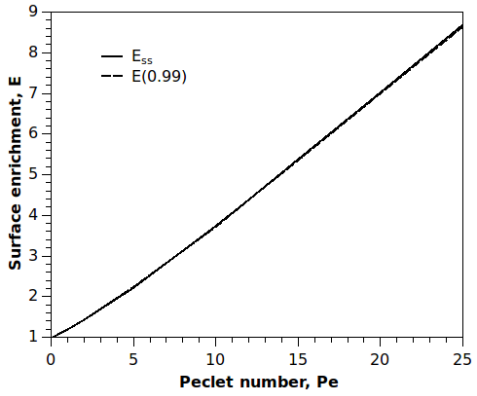

Figure 3.3: Surface enrichment: Model results at $\tau = 0.99$ vs. Asymptotic state solution.

3.3 Experimental Validation

In this section, different dry particle properties predicted by the model are compared against numerical and experimental results in literature.

3.3.1 Moderate Péclet number and low initial saturation

In the first study used for comparison [Vehring et al., 2007], glycoprotein particles with increasingly hollow morphology were formed under controlled conditions using a droplet chain apparatus. Different drying gas temperatures resulted in a Péclet number range between 2.7 and 16.8, which lies in the moderate Péclet number regime. A numerical model was also proposed to predict the transient concentration profiles and the droplet evaporation rate. However, the model did not include a means to predict the dry particle diameter and density, so the VFL model was used to calculate them [Vehring, 2008].

As pointed out previously [Vehring, 2008], components such as proteins often do not crystallize. Thus, using the time when equilibrium saturation, ES, or critical supersaturation, CSS, is reached to calculate the final dry particle diameter is not relevant in this case. Instead, a value close to the component true density, ρ_t, was used. In this case, the formed shell was assumed to be in an amorphous rather than a crystalline state [Vehring, 2008].

Figure 3.4 shows the comparison between the measured dry particle diameter and measured particle density and the predicted ones using the proposed model (chapter 2) and the classical particle formation model using the steady state value

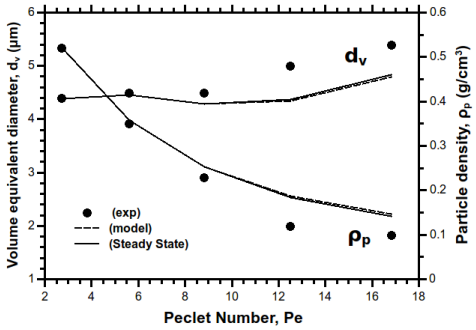

Figure 3.4: Measured vs. predicted particle volume equivalent diameter, d_{v}, and particle density, ρ_{p}. [Vehring et al., 2007; Vehring, 2008]

for surface enrichment, E_{ss} [Vehring, 2008].

As shown in Figure 3.4, the two theoretical approaches yield almost identical results in this case, as expected. In this experiment the initial saturation of the solute ($s_{\mathrm{o}} = 0.003$ based on $\rho_{\mathrm{t}} = 1.37$ g/cm^3) was very low. Hence, shell formation was initiated late in the drying process, when both models predict similar surface enrichment. The appropriate concentration value for estimation of the onset of shell formation was not known beforehand. A value of 0.85 g/cm^3 was derived by fitting the model results to the experimental ones at the lowest Péclet number.

In this case, both models predict particle size and density with sufficient accuracy to greatly assist in the particle design process. It is not surprising that there is not a perfect match between experiment and models considering the relatively simple nature of the theoretical description. Both models are limited to a constant value for the solute diffusivity, D, which is in reality a function of the solute concentration, so as the concentration increases with the droplet evaporation the solute diffusivity drops and the average or actual Pe number for the whole evaporation time is larger than the initial value at the beginning of the evaporation. This results in a higher surface enrichment, E, which means a shorter time is needed until surface concentration reaches the minimum values to trigger shell formation. This shorter time results in a larger droplet diameter at the onset of shell formation compared to the calculated one. This is one of the reasons behind the underestimated dry particle volume equivalent diameter, d_{v}, and the overestimated particle density, ρ_{p}, predicted by both models compared to the measured values. This is referred to as *Particle formation with changing Péclet number* [Vehring, 2008; Vehring et al., 2007].

In addition, the appropriate concentration value for the onset of shell formation is likely temperature dependent [Leong, 1987] and the models cannot properly account for deformation of the shells, which was visible in the electron micrographs of the dried particles in this study.

3.3.2 Moderate Péclet number and high initial saturation

Lin and Gentry [2003] experimentally studied the morphology of spray dried solution droplets for different solutes using a pendant droplet approach. Three different initial saturation ratios, $s_{\mathrm{o}} = 0.2$, 0.4 and 0.6, at four different drying air temperatures

were used for the evaporation of sodium chloride solution droplets. The authors reported the visually observed time for the appearance of the first crystal and the corresponding reduced droplet diameter, i.e., the droplet diameter divided by the initial droplet diameter.

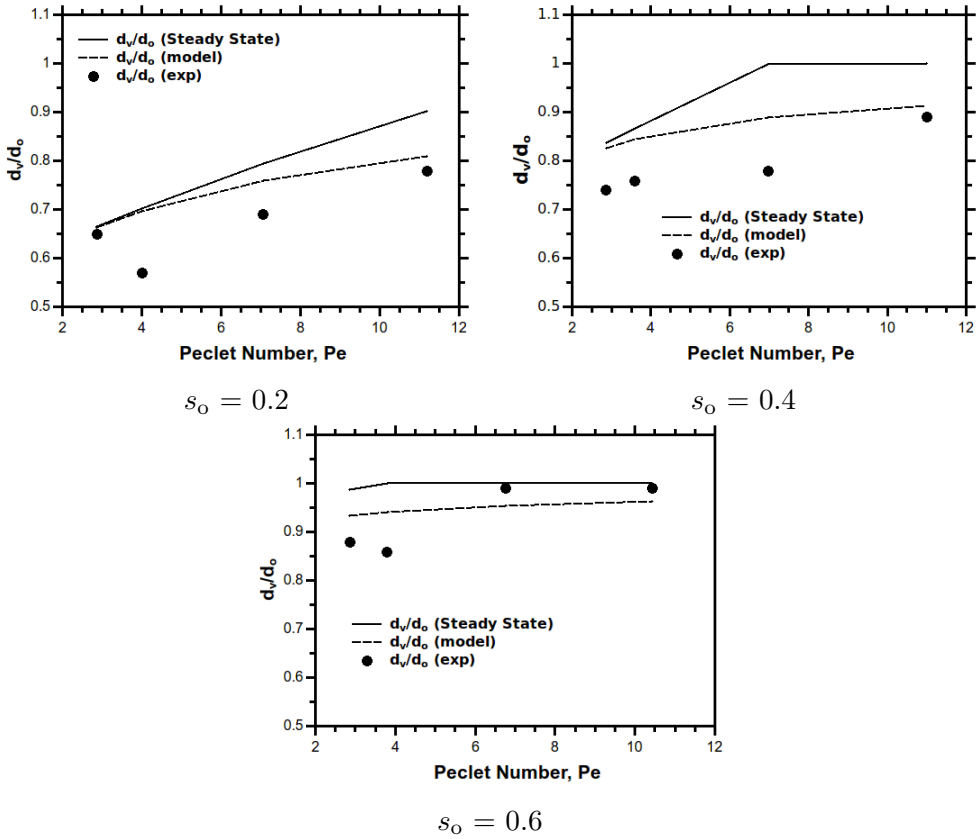

Figure 3.5: Predicted vs. measured particle volume equivalent diameter, d_{v}, for different initial saturation ratios ($s_{\mathrm{o}} = 0.2$ top left panel, $s_{\mathrm{o}} = 0.4$ top right panel, $s_{\mathrm{o}} = 0.6$ bottom panel).[Lin and Gentry, 2003]

The present model was used to calculate the droplet diameter at the onset of crystallization based on the equilibrium saturation value of $C_{\mathrm{sol}} = 6.167$ M given by Tang and Munkelwitz [1984]. The Péclet number was calculated based on an estimate of the evaporation rate of water given by Vehring et al. [2007] and the diffusion coefficient of sodium chloride in aqueous solutions given by Guggenheim [1954].

Figure 3.5 shows the results of the model using the transient value of surface enrichment, $E(\tau)$, in comparison to the experimental results and the results using the steady state value, E_{ss}.

Agreement between experimental and model results is reasonable, considering that some experimental conditions were outside of the range of application of the model. Droplets were in the millimeters range and suspended from a filament. Nev-

ertheless trends are predicted correctly.

Figure 3.5 shows that the two models deviate increasingly from each other at high saturation ratios, s_o, and higher Péclet numbers, Pe, as expected. The importance of these two parameters was realized earlier in the literature [Vehring et al., 2007].

We can also see that, compared to the classical model, the new model more accurately predicts the measured particle diameter at higher Péclet numbers, and when the initial saturation is large, as shown in the bottom panel. In fact, the classical model erroneously predicts surface supersaturation for this case from the very beginning of the evaporation period, i.e., $\tau = 0$, because it cannot account for the transient behavior. The current model doses not suffer from this drawback.

The results shown in Figure 3.5 were calculated based on the assumption that sodium chloride crystallization commences without delay when saturation, $s = 1$, is reached at the surface. Several researchers studied the crystallization of evaporating sodium chloride droplets and found that in fact supersaturation, $s > 1$, is necessary to trigger crystallization [Xiong and Kodas, 1993; Leong, 1987; Tang and Munkelwitz, 1984]. Hence, the surface saturation ratio at the onset of crystallization which was used in the model was adjusted by matching the dry particle diameter at the smallest Péclet number and intermediate initial saturation ration of $s_o = 0.4$. Then, using the same approach as in the previous section, this saturation ratio was also applied for the larger Péclet numbers.

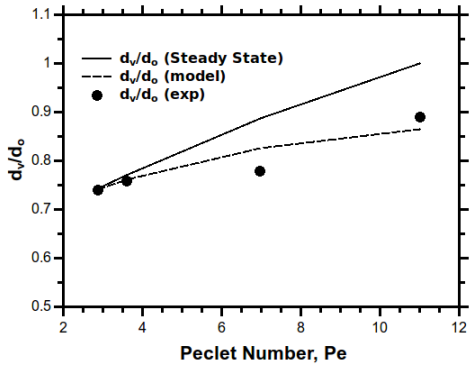

Figure 3.6: Predicted vs. measured particle volume equivalent diameter, d_v, for s_o=0.4. [Lin and Gentry, 2003]

Figure 3.6 shows the modeling results obtained using a supersaturation ratio of $s_{sat} = 1.425$. The results agree well with observed reduced droplet diameter at the onset of crystallization. The supersaturation ratio used to fit the first data point was found to be in excellent agreement with the critical supersaturation ratio for sodium chloride, $s_{sat} = 1.40$, numerically calculated and experimentally measured by Brechtel et al., [Brechtel and Kreidenweis, 2000a,b].

The present case shows that the use of the new model to predict the transient surface enrichment, $E(\tau)$, leads to significant improvement at large Péclet numbers and high initial saturation ratios.

3.3.3 High Péclet number and high initial saturation

Widiyastuti et al., [Lenggoro et al., 2000; Widiyastuti et al., 2007] numerically and experimentally investigated spray pyrolysis of zirconyl hydroxychloride solution droplets. The diffusion coefficient of zirconnyl hydroxychloride was not reported in their work and the Péclet number could not be calculated. However, due to the very high temperatures of up to 700 °C, used in the study it can be assumed that the resulting Péclet number is large.

The authors developed a numerical model to predict the radial concentration profiles and shell thickness for the final dry particle. For the zirconyl hydroxychloride used in this study solubility and critical supersaturation of 5.7 M and 8 M, respectively, are well documented [Jayanthi et al., 1993].

The ratio of the dry particle size to the initial droplet diameter was calculated from the reported measured data. Using an initial concentration of 0.32 g/cm^3(s_o = 0.35) and an estimated average shell density, ρ_{sh}, equal to the zirconium dioxide true density of 5.68 g/cm^3 [Pakhomov, 2011], the dry particle shell thickness can be calculated using Equation 2.151 or Equation 2.152.

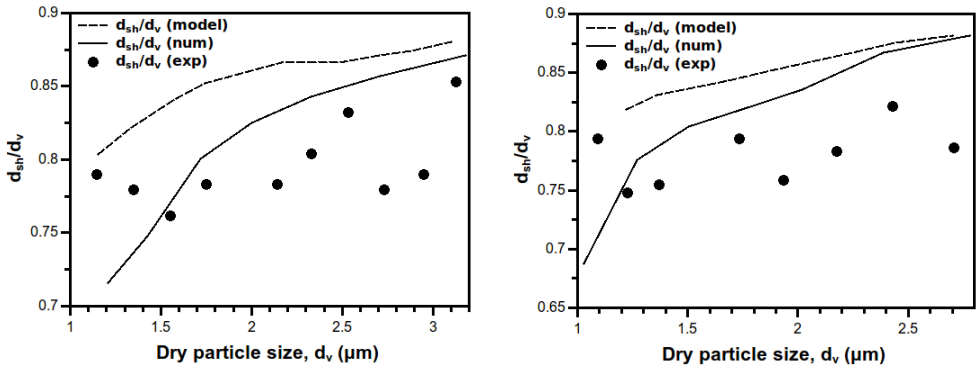

Figure 3.7: Predicted vs. measured shell thickness of Zirconia particles (T=500 °C, left panel ; T=700 °C, right panel). [Widiyastuti et al., 2007]

Figure 3.7 shows the dry particle shell thickness predicted by the present model and by the numerical model suggested by Widiyastuti et al., [Widiyastuti et al., 2007]. The present model results have the same trend as the numerical model. Despite the simplicity of the presented model, its results are appropriate for microparticle design.

3.4 Applications

In this section, the application of the classical [Vehring, 2008; Vehring et al., 2007] and proposed particle formation models to the design and production of microparticles for some applications is discussed.

3.4.1 The design of L-leucine containing microparticles

In this application, the classical particle formation theory is used in the design of L-leucine containing microparticles. This was possible due to the low Péclet numbers, Pe, and low initial saturation ratios, s_o, of the evaporation process. The asymptotic normalized concentration profiles were calculated for the two components used (L-leucine and trehalose) as shown in Figure 3.8.

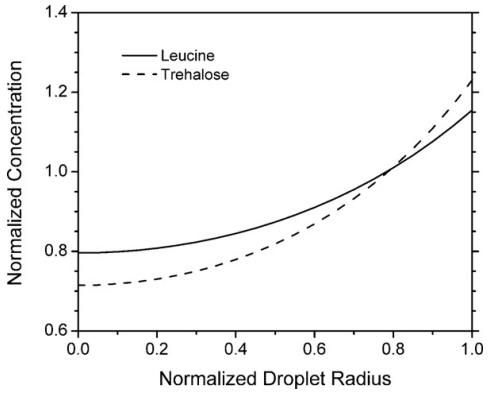

Figure 3.8: Radial normalized concentration profiles, $\frac{c}{c_m}$, of L-leucine and trehalose.

The solid state of Leucine in the final dry particle was determined using Raman Spectroscopy [Vehring, 2005] and found to be in good agreement with an increasing precipitation time for higher L-leucine initial concentration according to Equation 2.131.

Figure 3.9 shows the calculation of the L-leucine saturation time and shows that it reaches saturation before trehalose (due to the higher solubility of trehalose) and thus it is the main shell former.

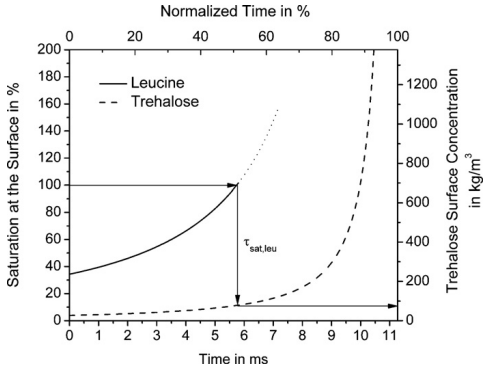

Figure 3.9: Surface concentration and saturation time of L-leucine.

Figure 3.10 shows the increase of the crystalline leucine content of the final dry particle with the increase in the initial mass fraction. Equation 2.131 shows that

for a given evaporation rate, κ, the precipitation time, τ_p, increases with the initial saturation ratio. τ_p was correlated with a higher crystalline content, as expected.

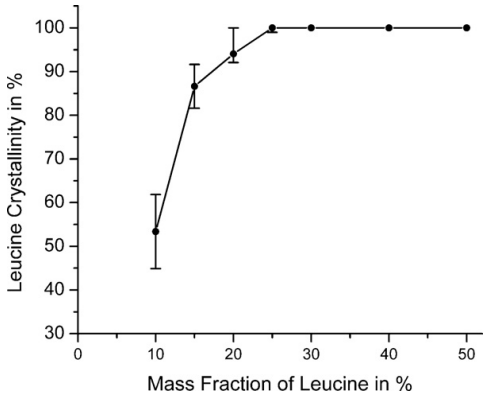

Figure 3.10: Crystallinity of L-leucine in the final dry particle.

SEM micrographs of the dried particles provide further support of the proposed model, as the predicted increase in volume equivalent diameter, d_v, with increasing initial saturation ratio, s_o, (Equation 2.138) was observed in this experiment as shown in Figure 3.11.

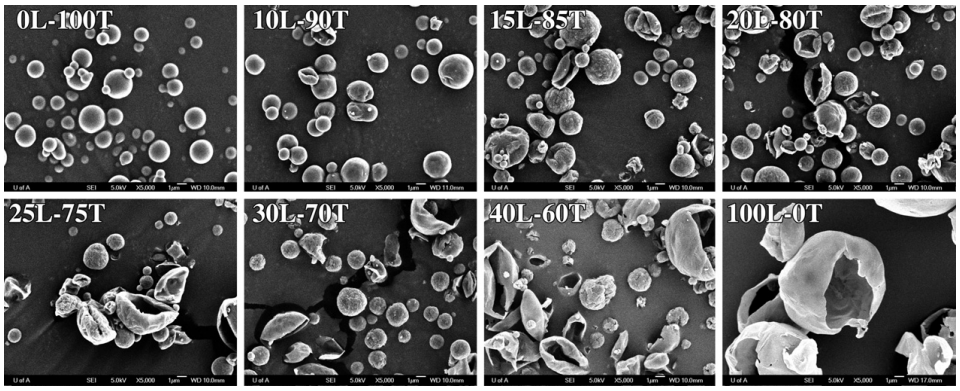

Figure 3.11: Morphology of spray dried L-leucine (L) trehalose (T) microparticles with varying mass fractions of L-leucine.

3.4.2 Formation of sodium nitrate particles

In this study, sodium nitrate microparticles were formed by the evaporation of solution microdroplets in a droplet chain setup (see chapter 4 for a description of the setup). Four initial concentrations with two evaporation rates were used to test the effect of the initial saturation ratio, s_o, and the Péclet number, Pe, on the morphology and the solid state of the final dry powder.

The solute surface saturation ratio was calculated and the corresponding time to reach saturation was used to calculate the final dry particle diameter (Equation 2.138). Figure 3.12 shows the surface saturation ratios of sodium nitrate evaporating at two temperatures, 85°C and 125°C.

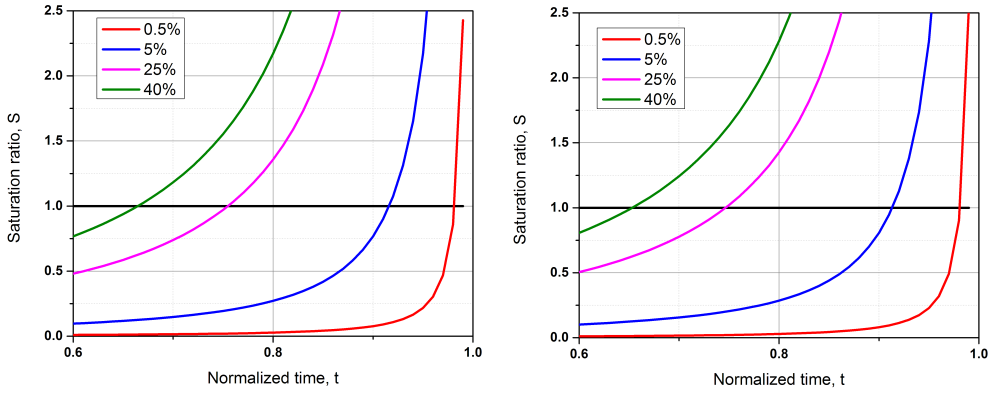

$T = 85°C$ $T = 125°C$

Figure 3.12: Sodium nitrate surface saturation for different initial concentrations, C_o. The time axis shows the time needed to reach saturation, as fraction of the total droplet lifetime.

Figure 3.13 shows the calculated dry particle diameter compared to values measured by averaging the dry particle diameter of 70 particles from the SEM images. A good agreement can be observed.

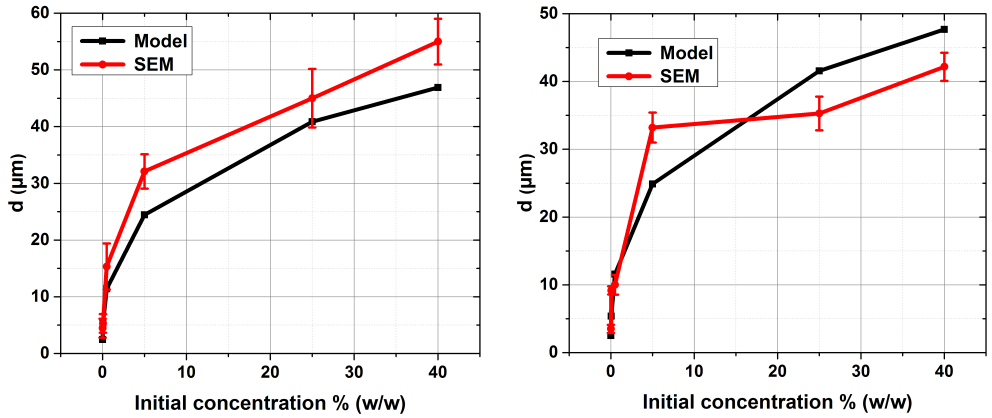

$T = 85°C$ $T = 125°C$

Figure 3.13: Diameter of the sodium nitrate dry particle, d_v, at different initial concentrations. Model results vs. SEM images.

Figure 3.14 shows the SEM images of the final dry particle. As the initial concentration increases, the time needed to reach saturation, τ_{sat}, decreases with a subsequent increase in the precipitation time, τ_p, which promotes crystallization.

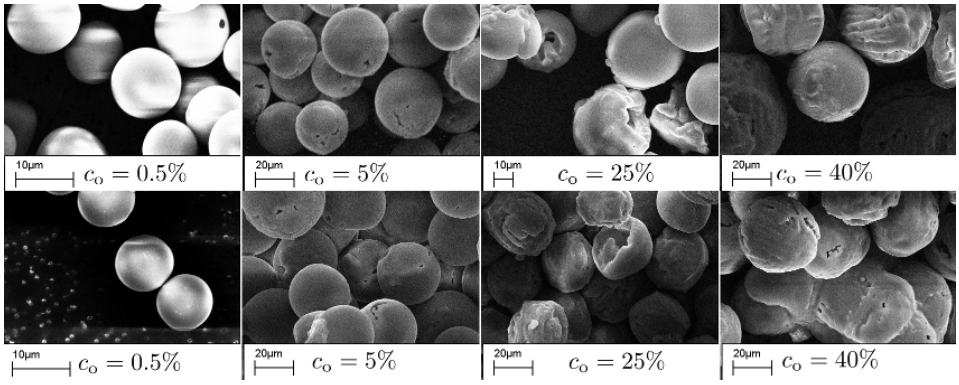

Figure 3.14: SEM images of sodium nitrate particles formed at 85°C (top) and 125°C (bottom) at different initial concentrations.

3.5 Conclusions

Through this chapter and chapter 2, it was shown that the asymptotic solution of the one dimensional spherically symmetric diffusion equation derived by Gardner [Gardner, 1965] to describe the concentration profile of an evaporating spherical droplet introduces a significant error for high Péclet numbers or high initial saturation ratios. Although the solution itself is correct in a mathematical sense, it does not consider the limited droplet lifetime.

chapter 2 introduces an analytical approach to calculate the time needed for the concentration profile to reach the asymptotic solution [Gardner, 1965] by taking into account the droplet lifetime.

The proposed approach also gives two alternatives for the calculation of the surface enrichment during the evaporation process before the asymptotic state is reached. The first is to solve the governing equation in time and space, while the other one offers an easy way of calculating the evolution of surface enrichment using an algebraic equation.

The results of proposed particle formation model become more important as the difference between the transient and asymptotic solution gets bigger. Solution droplets evaporating with a high Pe number or high initial saturation ratio, s_o, are typical cases.

Chapter 4

A hybrid approach for the measurement of variable droplet evaporation rate

4.1 Introduction

A new hybrid Optical-Numerical approach is proposed for the determination of the variable evaporation rate of a multi-component solution or suspension droplet. The proposed approach is based on the use of the droplet trajectory data to calculate the droplet velocity and acceleration. With the knowledge of the initial droplet diameter, the droplet evaporation rate and diameter can be calculated at any time during the evaporation process. It turns out that the accuracy of the predicted evaporation rate depends largely on the droplet generation frequency. The error increases with a decreasing droplet generation frequency. To overcome this limitation, higher order numerical schemes are used to predict the evaporation rate with a reasonable accuracy at low generation frequencies. The proposed approach is robust, reliable, much easier to use and less expensive compared to other fully optical techniques commonly used. Some benchmark cases have been used to assess the accuracy of the proposed approach.

Many industrial processes depend on the evaporation of pure or non-pure droplets for the production of a specific product. Examples of this include the use of spray dryers in the food and pharmaceutical industries. The evaporation rate is a key parameter in any evaporation process as it affects many features of the process itself and its final product [Vehring, 2008]. Although the evaporation rate can be controlled by the process parameters such as the drying gas temperature and the relative humidity, its precise determination is not easy. The reason for this is the many interfering physical and chemical mechanisms involved in the evaporation process. Analytical expressions for the evaporation rate are limited to very specific and simple flow situations. For these reasons experimental determination of the evapo-

Parts of this chapter has been published in the following publications.

1. M. Boraey, A. Baldelli, and R. Vehring. Theoretical and experimental investigation of particle formation from evaporating microdroplets. In *AAAR 32nd Annual Conference, American Association for Aerosol Research, Portland, Oregon, USA, September 30 - October 4*, 2013a

ration rate is preferred.

There are several techniques for the measurement of the evaporation rate and droplet diameter [Nandiyanto and Okuyama, 2011], such as low-angle light scattering [Lamanna et al., 2005], analytical expressions, i.e., Maxwell's equation, [Finlay, 2001] and numerical simulations [Sirignano, 1999]. However, these techniques suffer from some limitations. For example, in light scattering techniques the determination of the droplet diameter becomes difficult as its geometry starts to deviate from that of a sphere. In fact, the accuracy of the technique is at its worst (during the final stage of the drying process) when it is most needed, as it is at the end of the droplet lifetime that deviations from simple theories are most apparent.

Also if the droplet diameter or the exposure time is small, the intensity of the scattered light is reduced, which may affect the signal strength and the detection limits. Using a high energy laser to overcome this problem may affect the evaporation process through local heating of the droplet. Another limitation to this class of techniques is the dependence of the scattered light intensity on the optical properties of the droplet (i.e., index of refraction) [Hinds, 1999]. For droplets of pure liquids or a mixture of different liquids this may be taken into account by measuring these properties for the mixture at hand **a priori**. However for a single-component or multi-component solution droplet that will eventually form a solid particle it becomes very difficult to determine these properties in advance as they vary with the change in the solvent mass fraction during the evaporation process.

In analytical expressions and numerical simulations, the temperature-vapor pressure relationship must be known in addition to other physical properties.

The objective of this chapter is to provide a new approach for the determination of the evaporation rate of a droplet based on its trajectory data.

4.2 Experimental setup

For the present study a custom built setup is used to collect the needed data. The setup consists of a glass tube with a droplet-on-demand droplet generator (a piezoceramic surrounding a glass capillary) to generate droplets of a pre-specified initial diameter with controlled generation frequency. All the experimental work including building the setup and collecting the data was done by *Alberto Baldelli* in the particle engineering laboratory at the University of Alberta. The same setup has been widely used and described in many previous studies [Vehring et al., 2007] (Figure 4.1).

Droplets are injected horizontally into the glass tube with an initial velocity $\mathbf{v}_{\mathrm{ix}}$. The droplet injection velocity is adjusted such that the droplet reaches the tube center line when its velocity in the X direction drops to zero.

A laminar flow of the drying gas with controlled temperature and humidity enters the tube from the top to provide the heat needed for evaporation. A high resolution camera is used along with a strobe light to acquire the data of the droplet trajectory during its evaporation in the glass tube.

Given the tube dimensions and the camera magnification the resulting photos can be processed to give the droplet trajectory. The accuracy of the resulting trajectory data will depend in part on the camera resolution.

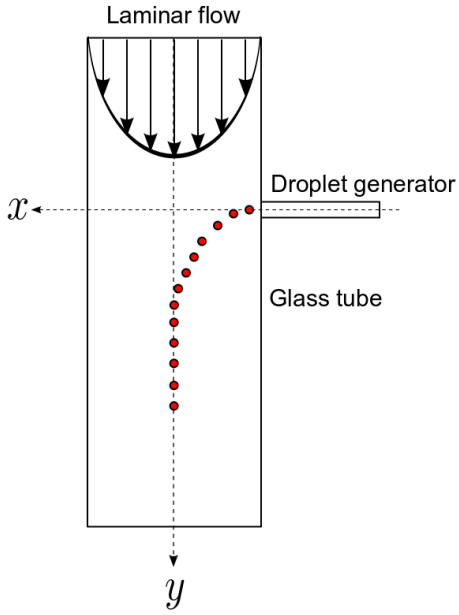

Figure 4.1: The droplet chain setup.

4.3 The hybrid approach for the determination of the variable evaporation rate

In this section the theory behind the proposed approach for the determination of the variable evaporation rate, $\kappa(t)$, is explained. The equations used to calculate different variables are derived and the numerical methods used for the implementation are explained.

4.3.1 Theory

Neglecting the buoyancy force (due to the much higher density of the droplet (e.g., $\sim 10^3$ kg/m^3) compared to that of the drying gas (e.g., ~ 1 kg/m^3)), the droplet motion is governed by two forces, the drag force and the gravitational force.

For an evaporating solution droplet, the droplet density, ρ_d, can be calculated as follows:

$$m = m_\mathrm{solute} + m_\mathrm{solvent} = \frac{\pi}{6}\left[d_\mathrm{o}^3 c_\mathrm{o} + d^3(t)\rho_\mathrm{l}\right] \tag{4.1}$$

$$\rho_\mathrm{d} = \frac{m}{v} \tag{4.2}$$

$$\rho_\mathrm{d} = \rho_\mathrm{l} + c_\mathrm{o}\left[\frac{d_\mathrm{o}}{d(t)}\right]^3 \tag{4.3}$$

Using a coordinate system attached to the setup such that the glass tube center line represents the Y axis and points downwards and the droplet generator center

line represents the X axis (Figure 4.1), the droplet equation of motion can be written as follows:

$$\mathbf{F}_{\mathrm{G}} + \mathbf{F}_{\mathrm{D}} = \frac{\mathrm{d}(m\mathbf{v})}{\mathrm{d}t} \tag{4.4}$$

$$\mathbf{F}_{\mathrm{G}} + \mathbf{F}_{\mathrm{D}} = m\mathbf{a} + \mathbf{v}\frac{\mathrm{d}m}{\mathrm{d}t} \tag{4.5}$$

$$\frac{\mathrm{d}m}{\mathrm{d}t} = \frac{\pi}{2}\rho_{\mathrm{l}} d^2 \frac{\mathrm{d}d}{\mathrm{d}t} \tag{4.6}$$

$$\mathbf{F}_{\mathrm{G}} = m\mathbf{g} = \frac{\pi}{6}\left[d_{\mathrm{o}}^3 c_{\mathrm{o}} + d^3\rho_{\mathrm{l}}\right]\mathbf{g} \tag{4.7}$$

$$\mathbf{F}_{\mathrm{D}} = \frac{1}{2}\rho_{\mathrm{g}}||\mathbf{v}_{\mathrm{r}}||^2 A_{\mathrm{pro}}\frac{C_{\mathrm{D}}}{C_{\mathrm{cs}}}\mathbf{n}_{\mathrm{r}} \tag{4.8}$$

$$A_{\mathrm{pro}} = \frac{\pi}{4}d^2 \tag{4.9}$$

$$\mathbf{n}_{\mathrm{r}} = \frac{\mathbf{v}_{\mathrm{r}}}{||\mathbf{v}_{\mathrm{r}}||} \tag{4.10}$$

$$\mathbf{v}_{\mathrm{r}} = \mathbf{v}_{\mathrm{dg}} - \mathbf{v} \tag{4.11}$$

$$C_{\mathrm{cs}} = 1 + \frac{\lambda}{d}\left[2.34 + 1.05\exp\left(-0.39\frac{d}{\lambda}\right)\right] \tag{4.12}$$

The drag coefficient, C_{D}, depends on the range of the Re number of the droplet. For small Re numbers of less than unity, the following expression can be used [Hinds, 1999]:

$$C_{\mathrm{D}} = \frac{24}{Re} \tag{4.13}$$

For higher Re numbers the following relation can be used which is accurate within $\pm$ 5 % for Re less than 800 [Clift et al., 1978].

$$C_{\mathrm{D}} = \frac{24}{Re}\left(1 + 0.15Re^{0.687}\right) \tag{4.14}$$

Substituting all the variables in Equation 4.4 yields the following differential equation for the droplet diameter, d.

$$\frac{\mathrm{d}d(t)}{\mathrm{d}t} = \frac{2}{\mathbf{v}\pi\rho_l d^2(t)}\left[\mathbf{F}_{\mathrm{G}} + \mathbf{F}_{\mathrm{D}} - m\mathbf{a}\right] \tag{4.15}$$

The solution of Equation 4.15 gives the droplet diameter at any given time; then the evaporation rate can be calculated. Note that this equation is valid for both X and Y directions but with different values for $\mathbf{v}$ and $\mathbf{a}$ components.

The droplet velocity and acceleration can be calculated from the droplet trajectory as follows:

$$\mathbf{v} = \frac{\mathrm{d}\mathbf{s}}{\mathrm{d}t} \tag{4.16}$$

$$\mathbf{a} = \frac{\mathrm{d}^2\mathbf{s}}{\mathrm{d}t^2} = \frac{\mathrm{d}\mathbf{v}}{\mathrm{d}t} \tag{4.17}$$

For a laminar flow in a circular tube the radial velocity profile is given by:

$$\mathbf{v}_{\mathrm{dg}}(s_{\mathrm{x}}) = 2\ \mathbf{v}_{\mathrm{av}} \left[1 - \left(\frac{2s_{\mathrm{x}}}{d_{\mathrm{t}}}\right)^2\right] \tag{4.18}$$

4.3.2 Calculation of the droplet velocity and acceleration

Equation 4.15 uses the velocity and acceleration of the droplet that are calculated from its trajectory data. The first source of errors comes from the trajectory data and how they were acquired using the high resolution camera. The measurement errors in the velocity and acceleration values will add to the error introduced by the numerical approximation of the governing equation. To avoid the propagation of the numerical error in the calculation of the velocity to the calculation of the acceleration, the acceleration is calculated from the displacement rater than from the velocity.

Regardless of the numerical scheme used, the accuracy of the calculated velocity and acceleration will depend on the time increment between the trajectory data points, which in turn is a function of the droplet generator frequency. The preceding discussion suggests that the use of the commonly used second order schemes is not feasible and a numerical scheme with high order of accuracy is necessary, especially at low droplet generation frequencies.

Four finite difference schemes have been tested.

- 8^{th} order central difference scheme.
- 4^{th} order Padé scheme.
- 6^{th} order C-D scheme.
- 8^{th} order C-D scheme.

8^{th} order central difference scheme

This is a standard finite difference scheme with 8^{th} order accuracy [Fornberg, 1988]. The first derivative of displacement (i.e., velocity) is calculated using the following 8^{th} order central scheme.

$$\begin{aligned} f_i^{'} \approx \frac{1}{h}\Bigg[&\frac{1}{280}f_{i-4} - \frac{4}{105}f_{i-3} + \frac{1}{5}f_{i-2} - \frac{4}{5}f_{i-1} \\ &+\frac{4}{5}f_{i+1} - \frac{1}{5}f_{i+2} + \frac{4}{105}f_{i+3} - \frac{1}{280}f_{i+4}\Bigg] \end{aligned} \tag{4.19}$$

The velocity at the end points are calculated using 8^{th} order one sided schemes.

$$\begin{aligned} f_1^{'} \approx \frac{1}{h}\Bigg[&\frac{-761}{280}f_1 + 8f_2 - 14f_3 + \frac{56}{3}f_4 - \frac{35}{2}f_5 \\ &+\frac{56}{5}f_6 - \frac{14}{3}f_7 + \frac{8}{7}f_8 - \frac{1}{8}f_9\Bigg] \end{aligned} \tag{4.20}$$

$$f_n^{'} \approx \frac{1}{h}\left[\frac{761}{280}f_n - 8f_{n-1} + 14f_{n-2} - \frac{56}{3}f_{n-3} + \frac{35}{2}f_{n-4} - \frac{56}{5}f_{n-5} + \frac{14}{3}f_{n-6} - \frac{8}{7}f_{n-7} + \frac{1}{8}f_{n-8}\right] \tag{4.21}$$

The second derivative of displacement (i.e., acceleration) is calculated using the following 8^{th} order scheme.

$$f_i^{''} \approx \frac{1}{h^2}\left[\frac{-1}{560}f_{i-4} + \frac{8}{315}f_{i-3} - \frac{1}{5}f_{i-2} + \frac{8}{5}f_{i-1} - \frac{205}{72}f_i + \frac{8}{5}f_{i+1} - \frac{1}{5}f_{i+2} + \frac{8}{315}f_{i+3} - \frac{1}{560}f_{i+4}\right] \tag{4.22}$$

The acceleration at the end points are calculated using 7^{th} order one sided schemes.

$$f_1^{''} \approx \frac{1}{h^2}\left[\frac{29531}{5040}f_1 - \frac{962}{35}f_2 + \frac{621}{10}f_3 - \frac{4006}{45}f_4 + \frac{691}{8}f_5 - \frac{282}{5}f_6 + \frac{2143}{90}f_7 - \frac{206}{35}f_8 + \frac{363}{560}f_9\right] \tag{4.23}$$

$$f_n^{''} \approx \frac{1}{h^2}\left[\frac{-29531}{5040}f_n + \frac{962}{35}f_{n-1} - \frac{621}{10}f_{n-2} + \frac{4006}{45}f_{n-3} - \frac{691}{8}f_{n-4} + \frac{282}{5}f_{n-5} - \frac{2143}{90}f_{n-6} + \frac{206}{35}f_{n-7} - \frac{363}{560}f_{n-8}\right] \tag{4.24}$$

7^{th} order one sided schemes are used for acceleration to keep the same stencil width used for velocity calculations.

4^{th} order Padé scheme

The Padé scheme is a compact finite difference scheme [Lele, 1992; Moin, 2010]. It has a higher accuracy with fewer stencil points compared to the standard finite difference schemes. This is achieved by expressing the derivative at a certain point as a function of the derivatives at neighbor points which results in a system of coupled equations of size n that needs to be solved simultaneously.

The 4^{th} order Padé scheme with 3^{rd} order accuracy at the boundary for the first

derivative is given as follows:

$$\begin{bmatrix} 1 & 2 & 0 & 0 & 0 & \cdots & 0 \\ 1 & 4 & 1 & 0 & 0 & \cdots & 0 \\ 0 & 1 & 4 & 1 & 0 & \cdots & 0 \\ \vdots & \vdots & \ddots & \ddots & \ddots & \vdots & \vdots \\ \vdots & \vdots & \vdots & \ddots & \ddots & \ddots & \vdots \\ 0 & 0 & 0 & \cdots & 1 & 4 & 1 \\ 0 & 0 & 0 & 0 & \cdots & 2 & 1 \end{bmatrix} \begin{Bmatrix} f_1^{'} \\ f_2^{'} \\ f_3^{'} \\ \vdots \\ \vdots \\ f_{n-1}^{'} \\ f_n^{'} \end{Bmatrix} \approx \frac{1}{h} \begin{Bmatrix} -\frac{5}{2}f_1 + 2f_2 + \frac{1}{2}f_3 \\ 3\left(f_3 - f_1\right) \\ 3\left(f_4 - f_2\right) \\ \vdots \\ \vdots \\ 3\left(f_n - f_{n-2}\right) \\ \frac{5}{2}f_n - 2f_{n-1} - \frac{1}{2}f_{n-2} \end{Bmatrix} \tag{4.25}$$

The 4^{th} order Padé scheme for the second derivative can be calculated by solving the following system of equations:

$$\begin{bmatrix} 1 & 0 & 1 & 0 & 0 & \cdots & 0 \\ 1 & 10 & 1 & 0 & 0 & \cdots & 0 \\ 0 & 1 & 10 & 1 & 0 & \cdots & 0 \\ \vdots & \vdots & \ddots & \ddots & \ddots & \vdots & \vdots \\ \vdots & \vdots & \vdots & \ddots & \ddots & \ddots & \vdots \\ 0 & 0 & 0 & \cdots & 1 & 10 & 1 \\ 0 & 0 & 0 & 0 & 1 & 0 & 1 \end{bmatrix} \begin{Bmatrix} f_1^{''} \\ f_2^{''} \\ f_3^{''} \\ \vdots \\ \vdots \\ f_{n-1}^{''} \\ f_n^{''} \end{Bmatrix} \approx \frac{1}{h^2} \begin{Bmatrix} 2f_1 - 4f_2 + 2f_3 \\ 12\left(f_1 - 2f_2 + f_3\right) \\ 12\left(f_2 - 2f_3 + f_4\right) \\ \vdots \\ \vdots \\ 12\left(f_{n-2} - 2f_{n-1} + f_n\right) \\ 2f_n - 4f_{n-1} + 2f_{n-2} \end{Bmatrix} \tag{4.26}$$

6^{th} order C-D scheme.

C-D schemes are a class of compact finite difference schemes that have higher order of accuracy compared to the standard finite difference schemes and the Padé scheme for the same stencil width [Mahesh, 1998]. Higher accuracy is achieved by expressing the first and second derivatives as a function of the first and second derivatives of neighbor points. This results in a coupled system of linear algebraic equations of size $2n$. Despite the higher computational cost, the C-D schemes are more suited for applications when both the first and second derivative are needed.

The scheme is 6^{th} order accurate for interior points while it is 3^{rd} order accurate for the boundary points 1 and n. The first and second derivative are calculated by

solving the following system of equations:

$$\begin{bmatrix} 1 & 0 & 2 & -h/2 & & & & & & \\ 0 & h & -6 & 5h & 0 & & & & & \\ \ddots & \ddots & \ddots & \ddots & \ddots & \ddots & & & & \\ & 0 & 7 & h & 16 & 0 & 7 & -h & & \\ & & -9 & -h & 0 & 8h & 9 & -h & 0 & \\ & & & \ddots & \ddots & \ddots & \ddots & \ddots & \ddots & \ddots \\ & & & & & 0 & 2 & h/2 & 1 & 0 \\ & & & & & & -6 & -5h & 0 & -h \end{bmatrix} \begin{Bmatrix} f_1' \\ f_1'' \\ \vdots \\ f_i' \\ f_i'' \\ \vdots \\ f_n' \\ f_n'' \end{Bmatrix} \tag{4.27}$$

$$\approx \frac{1}{h} \begin{Bmatrix} 3\left(f_2 - f_1\right) \\ 9f_1 - 12f_2 + 3f_3 \\ \vdots \\ 15\left(f_{i+1} - f_{i-1}\right) \\ 24\left(f_{i-1} - 2f_i + f_{i+1}\right) \\ \vdots \\ 3\left(f_n - f_{n-1}\right) \\ -9f_n + 12f_{n-1} - 3f_{n-2} \end{Bmatrix}$$

8th order C-D scheme.

This scheme is 8^{th} order accurate for the interior points 3 to $n-2$, 6^{th} order accurate for the interior points 2 and $n-1$ and 3^{rd} order accurate for the boundary points 1 and n.

The first and second derivative are calculated by solving the following system of

equations:

$$
\begin{bmatrix}
1 & 0 & 2 & -h/2 & & & & & & & & & \\
0 & h & -6 & 5h & 0 & & & & & & & & \\
7 & h & -16 & 0 & 7 & -h & & & & & & & \\
9 & -h & 0 & 8h & 9 & -h & 0 & & & & & & \\
 & \ddots & \ddots & \ddots & \ddots & \ddots & \ddots & \ddots & & & & & \\
 & & & 0 & 51 & 9h & 108 & 0 & 51 & -9h & & & \\
 & & & & -138 & -18h & 0 & 108h & 138 & -18h & 0 & & \\
 & & & & & \ddots & \ddots & \ddots & \ddots & \ddots & \ddots & \ddots & \\
 & & & & & & & 0 & 7 & h & 16 & 0 & 7 & -h \\
 & & & & & & & & -9 & -h & 0 & 8h & 9 & -h \\
 & & & & & & & & & 0 & 2 & h/2 & 1 & 0 \\
 & & & & & & & & & & -6 & -5h & 0 & -h
\end{bmatrix}
\begin{Bmatrix}
f_1' \\ f_1'' \\ f_2' \\ f_2'' \\ \vdots \\ f_i' \\ f_i'' \\ \vdots \\ f_{n-1}' \\ f_{n-1}'' \\ f_n' \\ f_n''
\end{Bmatrix}
$$

$$
\approx \frac{1}{h}
\begin{Bmatrix}
3\left(f_2 - f_1\right) \\
9f_1 - 12f_2 + 3f_3 \\
15\left(f_3 - f_1\right) \\
24\left(f_1 - 2f_2 + f_3\right) \\
\vdots \\
107\left(f_{i+1} - f_{i-1}\right) - \left(f_{i+2} - f_{i-2}\right) \\
-\left(f_{i+2} + f_{i-2}\right) + 352\left(f_{i+1} + f_{i-1}\right) - 702f_i \\
\vdots \\
15\left(f_n - f_{n-2}\right) \\
24\left(f_{n-2} - 2f_{n-1} + f_n\right) \\
3\left(f_n - f_{n-1}\right) \\
-9f_n + 12f_{n-1} - 3f_{n-2}
\end{Bmatrix}
\tag{4.28}
$$

The reason for the reduced order of accuracy at the end points for the implicit difference schemes (i.e., Padé and C-D) comes from some considerations in the numerical solution of ordinary differential equations [Moin, 2010] as will be discussed in a later section (subsection 4.4.4).

4.3.3 Calculation of the droplet diameter and the evaporation rate

Equation 4.15 can be solved for the droplet diameter at any time and the evaporation rate can be calculated afterwords. Starting with a known initial droplet diameter, d_o, the droplet diameter, $d(t + \Delta t)$, can be calculated by numerically integrating

Equation 4.15 as follows:

$$d(t+\Delta t) \approx d(t) + \frac{2\Delta t}{\mathbf{v}\pi\rho_l d^2(t)} \left[\mathbf{F}_{\mathrm{G}} + \mathbf{F}_{\mathrm{D}} - m\mathbf{a}\right] \tag{4.29}$$

Equation 4.29 can be solved for either of the two directions. However, the droplet velocity in each direction is zero at some point in its trajectory. $\mathbf{v}_x$ approaches zero as the droplet approaches the tube center line and $\mathbf{v}_y$ is zero for the horizontally injected initial droplet. The R.H.S. of Equation 4.29 approaches infinity in both cases.

This problem can be avoided by writing Equation 4.29 for both directions then summing them to calculate the droplet diameter, d, as follows (see Appendix B for the derivation):

$$d(t+\Delta t) \approx d(t) + \frac{2\Delta t}{(v_x + v_y)\pi\rho_l d^2(t)} \left[F_{\mathrm{G}x} + F_{\mathrm{G}y} + F_{\mathrm{D}x} + F_{\mathrm{D}y} - m(a_x + a_y)\right] \tag{4.30}$$

The used coordinate system has to be chosen such that the sum of the two velocity components (i.e., $v_x + v_y$) is never zero as shown in Figure 4.1.

A better option is to solve the droplet equation of motion in the direction tangential to its motion; in this case the droplet velocity will always be more than zero. The resulting equation is:

$$d(t+\Delta t) \approx d(t) + \frac{2\Delta t}{\mathbf{v}_{\mathrm{s}}\pi\rho_l d^2(t)} \left[\mathbf{F}_{\mathrm{Gs}} + \mathbf{F}_{\mathrm{Ds}} - m\mathbf{a}_{\mathrm{s}}\right] \tag{4.31}$$

Where the subscript s denotes the component of vector quantities tangential to the droplet trajectory.

In the literature there is more than one definition for the evaporation rate. In the present work the particle engineering definition will be used [Vehring, 2008].

$$d^2(t) = d_{\mathrm{o}}^2 - \kappa t \tag{4.32}$$

Differentiating this equation with respect to time gives the expression for the evaporation rate.

$$\kappa = -\frac{\mathrm{d}d^2(t)}{\mathrm{d}t} = -2d(t)\frac{\mathrm{d}d(t)}{\mathrm{d}t} \tag{4.33}$$

The evaporation rate, κ, can now be calculated using Equation 4.33 and assuming a constant evaporation rate during the time increment Δt [Roth et al., 2004].

$$\kappa(t) \approx \frac{d^2(t) - d^2(t+\Delta t)}{\Delta t} \tag{4.34}$$

Where Δt can be calculated from the droplet generation frequency as follows:

$$\Delta t = \frac{1}{f} \tag{4.35}$$

Starting from a known initial droplet diameter, d_{o} , the evaporation rate and the droplet diameter can be calculated until the end of the evaporation process.

4.4 Results and discussion

To assess the validity and accuracy of the proposed approach, the calculated evaporation rate for a set of benchmark problems is compared with experimental or analytical values given in literature. To the best of the author's knowledge there is no available data in the literature for the evaporation rate of droplets as a function of the trajectory data. This is expected since all the available data is either analytically derived or optically measured using different light scattering techniques. The proposed approach is kinematics based, so the evaporation rate can be calculated even without knowing many of the droplet and drying gas properties (e.g., viscosity, latent heat of vaporization, saturation pressure/temperature relationship, thermal conductivity and heat capacity ... etc.) that are essential to the analytically derived models. To validate the model experimentally, an experimental setup was built.

4.4.1 Non-evaporating droplet

The first test case is a non-evaporating droplet in a stagnant flow. The reason for this is the ease of analytically calculating the trajectory for a constant diameter droplet [Hinds, 1999].

Although it looks trivial, the constant diameter droplet case turns out to be the most important case in validating the proposed approach. For an evaporating droplet the error in the calculated evaporation rate will be the total error coming from all sources including the solution of the droplet equation of motion in addition to the error in the trajectory data obtained experimentally. Any discrepancies between the known and calculated evaporation rate, κ, do not reflect the accuracy of the proposed algorithm.

For the case of a zero evaporation rate, κ, the trajectory data can be analytically calculated and does not need any measurements. Actually the algorithm will be using a group of variables that should ideally lead to an evaporation rate of zero. In this case the calculated evaporation rate will be the error introduced by the proposed approach.

For a non-evaporating droplet, the injection velocity $\mathbf{v}_{\mathrm{ix}}$ can be calculated using the glass tube radius as the stopping distance as follows [Hinds, 1999]:

$$\mathbf{v}_{\mathrm{ix}} = \frac{1}{2}\frac{d_{\mathrm{t}}}{\tau_{\mathrm{ro}}} \tag{4.36}$$

Where: τ_{ro} is the initial droplet relaxation time and is given by [Hinds, 1999].

$$\tau_{\mathrm{ro}} = \frac{\rho_{\mathrm{d}} d_{\mathrm{o}}^2 C_{\mathrm{cs}}}{18\mu} \tag{4.37}$$

Since the droplet is injected horizontally in the tube, the initial droplet velocity in the Y direction, $\mathbf{v}_{\mathrm{iy}}$, is zero. The droplet velocity in the X direction, $\mathbf{v}_{\mathrm{fx}}$, becomes zero as the droplet reaches the tube center line while the Y component of the velocity, $\mathbf{v}_{\mathrm{fy}}$, becomes the droplet terminal settling velocity, $\mathbf{v}_{\mathrm{ts}}$, given as follows [Hinds, 1999]:

$$\mathbf{v}_{\mathrm{ts}} = \tau_{\mathrm{ro}}\mathbf{g} \tag{4.38}$$

The droplet trajectory can then be calculated as follows using Stokes's law for drag (Equation 4.13) ,without an external flow around the droplet and assuming a constant droplet density [Hinds, 1999].

$$x(t) = \left[\mathbf{v}_{\mathrm{fx}} t - (\mathbf{v}_{\mathrm{fx}} - \mathbf{v}_{\mathrm{ix}})\,\tau_{\mathrm{ro}}\left(1 - \exp^{\frac{-t}{\tau_{\mathrm{ro}}}}\right)\right] - \frac{d_{\mathrm{t}}}{2} \tag{4.39}$$

$$y(t) = \left[\mathbf{v}_{\mathrm{fy}} t - (\mathbf{v}_{\mathrm{fy}} - \mathbf{v}_{\mathrm{iy}})\,\tau_{\mathrm{ro}}\left(1 - \exp^{\frac{-t}{\tau_{\mathrm{ro}}}}\right)\right] \tag{4.40}$$

The calculated trajectory data (i.e., $x(t)$ and $y(t)$) can be used instead of the measured one. The trajectory data was calculated for the first 100 ms of the droplet lifetime.

4.4.2 Role of the droplet generation frequency

It is clear that the accuracy of the predicted evaporation rate will depend on the droplet generation frequency. As will be shown later, the error becomes significant for droplet generation frequencies below 1000 Hz. In fact most of the results reported in literature are for the droplet diameter rather than the evaporation rate, κ [Roth et al., 2004], for a high range of droplet generation frequency, f (20-70 kHz) [Homer et al., 2009] and for droplets of liquid mixtures without any solutes [Hopkins and Reid, 2005, 2006].

4.4.3 Test cases

Three different droplet generation frequencies (250, 500 and 1,000 Hz) are tested for two droplet diameters (50 and 100 μm) with a solvent density ρ_l of 10^3 kg/m^3. For all cases the glass tube internal diameter is 30 mm. The drying gas is air at a temperature of 360 K and atmospheric pressure of 1.014 bar.

Table 4.1 shows the final calculated evaporation rate for various differencing schemes. The 8$^{\mathrm{th}}$ order FDM gives the most accurate results especially at higher droplet generation frequencies and larger droplets.

Table 4.1: The final predicted evaporation rate, κ (μm^2/ms).

f (Hz)	FDM 8$^{\mathrm{th}}$		Padé 4$^{\mathrm{th}}$		C-D 6$^{\mathrm{th}}$		C-D 8$^{\mathrm{th}}$	
	50 μm	100 μm	50 μm	100 μm	50 μm	100 μm	50 μm	100 μm
250	119.37	0.0	-76.40	1.36	-0.84E3	1.04	-1.27E8	-5.52E3
500	4.65	0.0	-58.05	0.21	-1.00E4	57.05	-1.07E6	-1.80E4
1,000	0.05	0.0	-58.57	0.03	-3.14E3	31.16	-1.47E6	-23.16

The accuracy for all schemes decreases dramatically with the decrease in the droplet generation frequency. However the effect of the droplet size is more significant. This shows that a high order scheme is needed especially for low droplet generation frequencies and smaller droplets.

Table 4.2 shows the normalized final droplet diameter. This value shows the loss of the initial droplet diameter due to the cumulative error in the calculated evaporation rate.

Both tables (Table 4.1 & Table 4.2) show that both C-D schemes (6$^{\mathrm{th}}$ & 8$^{\mathrm{th}}$ order) have a very large error compared to the 8$^{\mathrm{th}}$ FDM and the 4$^{\mathrm{th}}$ Padé schemes.

Table 4.2: Normalized final droplet diameter, $\frac{d}{d_0}$.

f (Hz)	FDM 8th		Padé 4th		C-D 6th		C-D 8th	
	50 µm	100 µm	50 µm	100 µm	50 µm	100 µm	50 µm	100 µm
250	0.49	0.99	-0.57	0.99	-1.89	0.99	737.42	5.10
500	0.99	0.99	-0.51	0.99	-6.67	0.86	-68.59	9.14
1,000	0.99	1.00	-0.51	0.99	-3.77	0.93	-2.58	-0.32

For this reason the two C-D schemes will not be used for the rest of the study. The reason for their large error despite their higher accuracy is discussed in a following section.

Figure 4.2 shows the normalized droplet diameter for the 50 µm diameter droplet. It highlights the cumulative nature of the error. The normalized final droplet diameter is affected by all the errors accumulating from the calculations at the previous time steps. Ideally this value is unity for the cases considered.

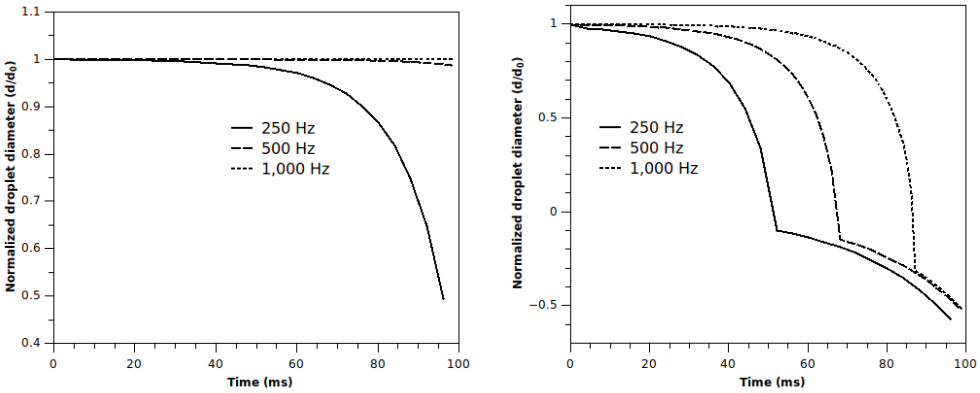

8th FDM 4th Padé

Figure 4.2: Normalized droplet diameter for the 50µm droplet.

Figure 4.3 shows the same information for the 100 µm diameter droplet case. It is clear that the error decreases for larger droplets, which puts a lower limit on the droplet size for a given scheme. These figures also help to identify at which time in the drying process the largest error occurs.

4.4.4 Optimal selection of the numerical scheme

Although the use of the 8th order FDM scheme looks favorable because of its small error, the downside of this scheme is that it needs a minimum number of data points to achieve this accuracy due to its wider stencil. For high values of droplet generation frequency, f, this is not a problem because the small time increment between the droplets allows the collection of a large number of data points.

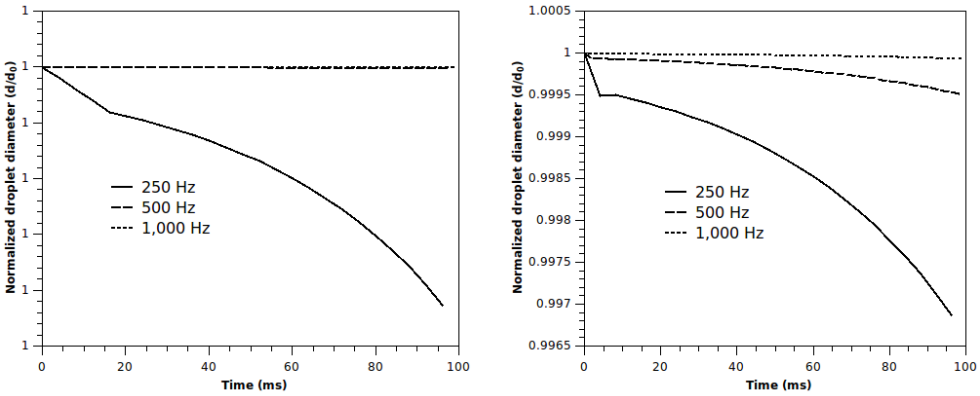

8^{th} FDM 4^{th} Padé

Figure 4.3: Normalized droplet diameter for the 100µm droplet.

On the other side for low values of f the distance and time between successive droplets is relatively large which may not provide the minimum number of data points for this scheme during the droplet lifetime.

A possible way to overcome this problem is to extend the measurement time, even unnecessarily. This will increase the cumulative error at the end point and may need a longer glass tube and a higher camera resolution to get the droplet trajectory in this long range with a reasonable accuracy. Another drawback of this approach is the difficulty of obtaining accurate trajectory data for smaller droplets. Normally droplets smaller than a specific size are not visible to the camera.

Using the 4^{th} order Padé scheme does not suffer from these limitations since it is a compact scheme which means that it achieves high numerical accuracy with fewer stencil points [Moin, 2010; Lele, 1992; Mahesh, 1998]. It is worth mentioning that despite its advantages, the Padé scheme is computationally more expensive than the traditional finite difference schemes. It involves the inversion of a matrix. This matrix is tridiagonal for the 4^{th} order Padé scheme so its inversion is relatively easy, but for higher order Padé schemes the matrix is a banded matrix which makes its inversion more expensive especially for large data sets.

A better solution seems to be the use of higher order compact schemes (8^{th} order or higher) like the C-D schemes despite their higher computational cost compared to the Padé schemes and the standard FDM schemes.

C-D schemes are a class of compact schemes that are considered to be a generalization of the Padé schemes [Mahesh, 1998]. For example a 6^{th} order accuracy for the first derivative needs a stencil width of 7 points for the FDM scheme [Fornberg, 1988], 5 points for the Padé scheme [Moin, 2010] and 3 points for the C-D scheme [Mahesh, 1998]. The drawbacks of the C-D schemes are its higher computational cost (requires the inversion of a matrix of size $2n$ compared to a matrix of size n for the Padé schemes and no matrix inversion at all for the FDM schemes) and a reduced order of accuracy at the boundary points.

For compact schemes, lower order boundary formulations have to be used to

ensure the stability of the overall scheme since the use of a boundary scheme with the same order of accuracy of the internal points does not always guarantee stability [Mahesh, 1998].

Since the derivatives are calculated by the solution of a coupled system of equations, this reduced order of accuracy at the boundary points affects the solution on all points. Although it has been suggested that the effect of this reduced order is limited to points close to the boundary for the Padé schemes [Moin, 2010], it was shown that the global error is largely determined by the boundary schemes [Lele, 1992].

The previous discussion explains the reason for the poor performance of the C-D schemes as shown in Table 4.1 and Table 4.2 compared to the FDM and Padé schemes. Another reason is that the C-D schemes are used in the present work to calculate temporal rather than spatial derivatives which makes the coupling between the boundary points (actually initial and final time points) and internal points stronger. In other words, even if the lower order of accuracy in estimating the derivatives is limited to boundary points, the error in calculating the droplet diameter propagates into all subsequent time points.

The search for higher order differencing schemes comes from the fact that the droplet generation frequency, f, is not determined by a required order of accuracy for the droplet velocity and acceleration, but rather by other considerations pertaining to the droplet generation process, i.e., a specific production rate, a predetermined spacing between successive droplets in the chain ... etc. So, in some cases, the use of low order schemes might be acceptable.

Finally, the use of the 8^{th} order FDM scheme is an optimal selection in terms of accuracy and computational cost unless the minimum number of data point can not be obtained. In this case the 4^{th} order Padé can be used.

4.5 A simplified approach

Because of the transient nature of the evaporation process, the governing equation for the droplet diameter, d, has to be solved by stepping in time (Equation 4.15). In a real evaporation process, the droplet trajectory is obtained using a camera and not calculated analytically as in subsection 4.4.1. In this case, any error in the droplet trajectory will be reflected into the calculated evaporation rate. This error will propagate very fast in subsequent time steps due to the transient nature of the problem. The error in the estimation of the initial droplet diameter, d_{o}, (which is a required variable for the previously proposed approach) is another source of errors which contributes in making the approach less suitable for practical applications.

4.5.1 Theory

In this section, a much simpler approach is proposed for the determination of the variable droplet diameter, $d(t)$, and the variable evaporation rate, $\kappa(t)$, that minimizes the propagation of the error in the droplet trajectory data and the initial droplet diameter.

This is done by calculating the droplet diameter, $d(t)$, from the droplet velocity in the Y direction assuming that the droplet has reached its terminal settling velocity,

$\mathbf{v}_{\mathrm{ts}}$ as follows:

$$d(t) \approx \sqrt{\frac{18\mu \mathbf{v}_{\mathrm{ts}}(t)}{\rho_{\mathrm{p}}(t) C_{\mathrm{cs}}(t) \mathbf{g}}} \tag{4.41}$$

In order to use this approximation, some assumptions and conditions have to be met which can be summarized as follows:

- The droplet Reynolds number, Re, is less than unity (i.e., small droplet $d(t)$).
- The droplet velocity in the Y direction, $\mathbf{v}_y(t)$, should be calculated using the minimum number of trajectory points.
- The droplet relaxation time, $\tau_{\mathrm{r}}(t)$, is small compared to the time step between the droplets, Δt.
- The component of droplet velocity relative to the gas velocity in the Y direction, $\mathbf{v}_{\mathrm{r}}$, can be approximated as the droplet terminal settling velocity, $\mathbf{v}_{\mathrm{ts}}$.
- The slip correction factor, C_{cs}, for the droplet should be close to unity.

The first condition is necessary because the droplet terminal settling velocity can only be calculated analytically for droplets with a Reynolds number less than unity [Hinds, 1999]. If this condition is not satisfied for the first droplet in the chain, the proposed approach can still be used but starting from the first point in the droplet chain that satisfies this condition.

The second condition is required to minimize the propagation of the error in obtaining the droplet trajectory date. The minimum number of points to calculate $\mathbf{v}_y$ is two, using Euler's first order approximation as follows:

$$\mathbf{v}_y(t) \approx \frac{y(t + \Delta t) - y(t)}{\Delta t} \tag{4.42}$$

Although a higher order approximation is favored, the uncertainty in the trajectory data does not guarantee a better approximation for the droplet velocity.

The third condition is required because the relaxation time, τ_{r}, reflects how fast the droplet accommodates to the surrounding flow field. For a particle starting from rest, the time needed to reach 63% of its terminal settling velocity ,$\mathbf{v}_{\mathrm{ts}}$, is $t = \tau_{\mathrm{r}}$ and to reach 95% of $\mathbf{v}_{\mathrm{ts}}$ is $t = 3\tau_{\mathrm{r}}$. So in assuming that the droplet has a constant diameter between two trajectory points, a small τ_r compared to Δt makes the assumption that the droplet reached its terminal settling velocity a reasonable one. If this condition is not satisfied the proposed approach can still be used but starting from the first point in the chain that satisfies it. This is possible since the droplet relaxation time decreases with the square of the droplet diameter as it evaporates, while the time step, Δt, is constant.

The droplet/particle relation time, $\tau_{\mathrm{r}}(t)$, can be calculated as follows [Hinds, 1999]:

$$\tau_{\mathrm{r}}(t) = \frac{\rho_{\mathrm{d}}(t) d(t)^2 C_{\mathrm{cs}}(t)}{18\mu} \tag{4.43}$$

While the time step, Δt, is given by Equation 4.35. The proposed approach can still be used even if this condition is not strictly satisfied. This is because the

droplet does not actually start from rest, but rather changes it velocity from the terminal settling velocity at one diameter to a lower terminal velocity at a smaller diameter.

The fourth condition is based on the third one by assuming that droplet reaches its terminal settling velocity in the time interval Δt.

The last condition is required since the slip correction factor, C_{cs}, is a non-linear function of the droplet diameter, d, and Equation 4.41 has to be solved iteratively if this condition is not satisfied. At atmospheric pressure, a droplet/particle with a diameter of 10 μm or more satisfies this condition.

For multi-component droplets, the dependence of the droplet density, ρ_{d}, on the droplet diameter, $d(t)$, through Equation 4.3 also necessitates the use of an iterative approach to solve Equation 4.41 for the droplet diameter, $d(t)$.

However, this can be avoided by calculating the droplet aerodynamic diameter, $d_{\mathrm{a}}(t)$, which does not depend on the droplet density, ρ_{d}, as follows (assuming a slip correction factor, C_{cs}, close to unity):

$$d_{\mathrm{a}}(t) = \sqrt{\frac{18\mu \mathbf{v}_{\mathrm{ts}}}{\rho_* C_{\mathrm{cs}} \mathbf{g}}} \tag{4.44}$$

Assuming a droplet chain centered at the tube center line with a fully developed laminar flow velocity profile and satisfying all the previously mentioned conditions, the droplet diameter at any time, $d(t)$, can be calculated as follows:

$$d(t) = \sqrt{\frac{18\mu}{\rho_{\mathrm{d}} g} \left[\Delta y f - \frac{8}{\pi} \frac{Q}{d_{\mathrm{t}}^2} \right]} \tag{4.45}$$

Where: Q is the drying gas flow rate. The evaporation rate, $\kappa(t)$, can then be calculated using Equation 4.34.

This simplified approach theoretically looks less accurate than the detailed approach suggested before. However, practical considerations related to the uncertainties of different measured parameters makes it more accurate than the detailed one in some cases.

The droplet terminal settling velocity, $\mathbf{v}_{\mathrm{ts}}$, is the difference between the measured droplet velocity in the Y direction, $\mathbf{v}_y$, and the drying gas velocity, $\mathbf{v}_{\mathrm{dg}}$.

$$\mathbf{v}_{\mathrm{ts}} = \mathbf{v}_y - \mathbf{v}_{\mathrm{dg}} \tag{4.46}$$

The droplet/particle terminal settling velocity, $\mathbf{v}_{\mathrm{ts}}$, has to be larger than the uncertainty in the measured droplet velocity, $\mathbf{v}_y$. This puts a lower limit on the smallest droplet diameter, $d(t)$, that can be calculated with a reasonable accuracy. It also puts an upper limit on the maximum flow rate in the tube, Q, in addition to the condition of a droplet Reynolds number, Re, less than unity.

In case of high gas temperatures, convection currents impose a limit on the minimum gas flow rate that can be used. The drying gas should have enough momentum to overcome convection currents resulting from non-uniform temperature distribution so that a stable droplet chain can be achieved.

4.5.2 A test case

In this section, a test case on the use of the simplified approach is presented to validate the proposed approach. All the required physical properties of the drying gas (air) and the solvent (acetone) are given in Appendix C.

The test case is the evaporation of acetone droplets. An acetone droplet chain was generated using the droplet chain setup and was allowed to evaporate in air at a room temperature of 18 °C with a generation frequency of 50 Hz. A digital camera was used to obtain the droplet trajectory during evaporation. The obtained image was used to calculate the coordinates of each droplet in the droplet chain. The drying gas (air) has a flow rate of 1 L/min and the internal tube diameter was 30 mm.

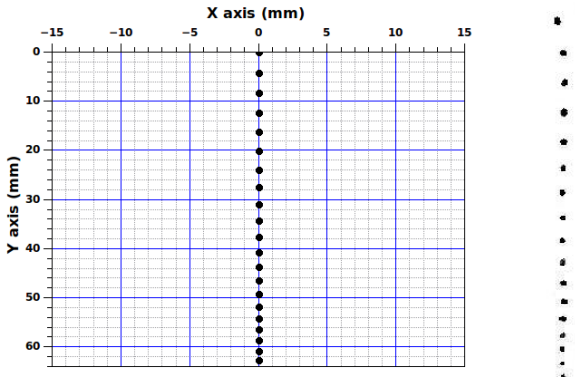

Figure 4.4: Trajectories of an evaporating acetone droplet chain.

Figure 4.4 shows a photo of the evaporating droplet chain and the measured Y coordinates of the droplets. The droplet diameter can then be calculated using Equation 4.45. Note that the first two droplets in the chain will not be considered because they are not at the tube center line.

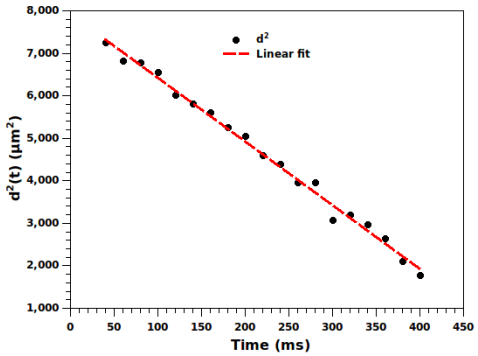

Figure 4.5: Calculated droplet diameter for the acetone droplet chain.

Figure 4.5 shows the calculated droplet diameter squared, d^2, from the obtained

trajectory data along with a liner fit. The variations around the linear fit shows that the detailed time stepping approach will suffer from a big error propagation and even with the simplified approach, the instantaneous evaporation rate, $\kappa(t)$, will not be accurate. The linear fit shows the trend of a constant evaporation rate according to what is known as the d^2 law [Finlay, 2001].

The slope of the linear fit is the average evaporation rate in the observed evaporation period. Based on these results the evaporation rate is calculated to be $\kappa = 14.99$ µm^2/ms.

The assumption of a Reynolds number less than unity can be checked by plotting the droplet Reynolds number for the observed period of evaporation time as shown in Figure 4.6.

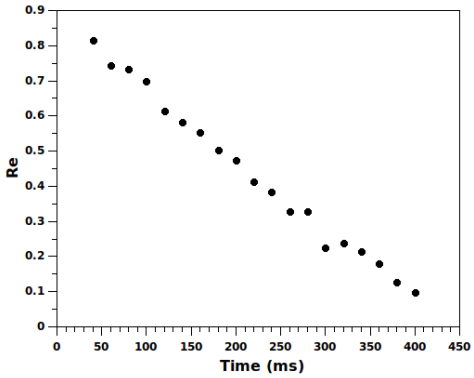

Figure 4.6: Droplet Reynolds number during evaporation.

Where the droplet Reynolds number is calculated as follows:

$$Re = \frac{\rho_{\mathrm{dg}} ||\mathbf{v}_{\mathrm{ts}}|| d}{\mu} \tag{4.47}$$

The last droplet in the chain has a diameter of 42.12 µm, so the slip correction factor, C_{cs}, can be assumed to be unity. The first droplet used to calculate the evaporation rate has a diameter of 85.21 µm with a corresponding relaxation time of τ_{r} = 16 ms. This relaxation time is smaller than the time step between the droplets, $\Delta t = \frac{1}{f} = 20$ ms. All the conditions necessary to use the simplified approach are satisfied in the current test case.

The verification of the predicted evaporation rate can be done by comparing it to the evaporation rate predicted using Maxwell's equation. The evaporation rate based on Maxwell's equation can be written as follows [Finlay, 2001] assuming that Stefan flow can be neglected.

$$\kappa = -\frac{\mathrm{d}d^2}{\mathrm{d}t} = \frac{8 D_{\mathrm{s}} [\tilde{c}_{\mathrm{s}} - \tilde{c}_{\infty}]}{\rho_{\mathrm{l}}} \tag{4.48}$$

Where: $\tilde{c}_{\mathrm{s}}$ is the solvent vapor concentration at the droplet surface and $\tilde{c}_{\infty}$ is the solvent vapor concentration far from the droplet surface. Equation 4.48 requires

the determination of the droplet equilibrium temperature, T_d, in order to calculate $\tilde{c}_s$.

The equilibrium temperature, T_d, can be calculated assuming that the droplet will maintain a constant temperature during evaporation as follows [Finlay, 2001]:

$$LD_s(\tilde{c}_s - \tilde{c}_\infty) + k(T_d - T_\infty) = 0 \tag{4.49}$$

Material properties in the gas phase, i.e., L, D_s and$k$, can be approximated by those of the surrounding medium (air in this case). This assumption is valid as long as the partial pressure of the solvent vapor at the droplet surface is small, as will be shown later [Finlay, 2001].

T_∞ is the surrounding gas temperature (18 °C in this case). This equation has to be solved iteratively because of the dependence of $\tilde{c}_s$ on T_d. Solving Equation 4.49 gives:

- Solvent surface vapor concentration, $\tilde{c}_s = 0.124$ kg/m^3
- Droplet temperate, T_d = -12.92 °C
- Solvent surface vapor pressure, $P_s = 4608.42$ Pa

To assess the validity of the constant droplet temperature assumption, the following inequality was checked [Finlay, 2001]:

$$\frac{8D_s(\tilde{c}_s - \tilde{c}_\infty)c_p}{12k} \ll 1 \tag{4.50}$$

Substituting all variables in Equation 4.50, this quantity is found to be 0.086. So this assumption is valid.

Now we have to check the second assumption of negligible Stefan flow. This assumption is valid if the ratio of vapor pressure at the droplet surface to the total pressure is small [Finlay, 2001].

$$\frac{P_s}{P_{total}} \ll 1 \tag{4.51}$$

Where: P_{total} is the total pressure (atmospheric in this case). In this case, this ratio is 0.045.

Now we can use Equation 4.48 to estimate the evaporation rate. The calculated value is $\kappa = 15.51$ μm^2/ms. This corresponds to an error of $e_\kappa = 3.4\%$ in the calculated evaporation rate using the simplified approach.

Given the fact that Maxwell's equation is a simplified mathematical description of the evaporation process, we can see that the proposed approach has a good accuracy.

4.6 Conclusions

A new approach for the determination of the variable evaporation rate of a droplet of virtually any composition is presented. The approach relies on solving the droplet

equation of motion numerically given its experimentally acquired trajectory data. The approach was validated by calculating the evaporation rate of a constant diameter droplet. The error predicted was minimal for a droplet generation frequency of 1000 Hz or more.

The poor performance of the higher order compact schemes suggests that the standard FDM schemes are the best option for the problem at hand.

The proposed approach offers a robust, easy to use, less complicated and less expensive alternative for the determination of a time dependent evaporation rate with the minimal knowledge of the material properties of different components involved in the evaporation process.

The proposed approach can be used to easily generate charts and look up tables for the evaporation rates of a variety of multi-component solutions at different conditions. Although the proposed technique lacks accuracy at very low droplet generation frequencies, it is promising and can be greatly improved by identifying the sources of errors and working to minimize them through further test cases.

This approach can be used to establish correlations or tabulated data for the evaporation rate of different solvents and solvent mixtures for pure and non pure droplets. Since the droplet chain setup is temperature and humidity controlled, the evaporation rate at different surrounding conditions can also be measured.

In the case of high uncertainties in the measured droplet trajectory data or low droplet generation frequencies, a simplified approach is introduced that minimizes the propagation of the error in the predicted droplet diameter and evaporation rate.

Chapter 5

Concentration profiles of an evaporating cylindrical solution droplet

5.1 Introduction

The purpose of this chapter is to develop an asymptotic state solution and a transient solution for the case of an evaporating cylindrical solution droplet.

The main motive to develop such a solution for this hypothetical case is to have a verification for the proposed numerical model that will be discussed in chapter 6. Similar to the case of a spherical droplet, We will start by developing the solute concentration profiles and surface enrichment for the asymptotic state then move to the transient case.

5.2 Asymptotic state solution

The solution developed here will follow the same approach developed by Gardner [Gardner, 1965] with some modifications to account for the difference in the droplet geometry (i.e., cylindrical vs. spherical).

Assume we have a cylindrical droplet that is infinitely long. If this droplet evaporates we can assume that the droplet height remains constant while the radius, $r_s(t)$, shrinks. If the droplet is a solution droplet, we expect that the evaporation of the solvent will generate a radial concentration gradient of the solute that depends on the solute properties and the rate of evaporation.

Assuming the mass diffusion coefficient of the solute in the solvent, D, to be constant, the solute radial concentration profile can be described by the one dimensional diffusion equation in the radial direction in cylindrical coordinates. This equation can be written as follows:

$$\frac{\partial C}{\partial t} = D\left[\frac{\partial^2 C}{\partial r^2} + \frac{1}{r}\frac{\partial C}{\partial r}\right] \tag{5.1}$$

The radial coordinate, r, can be normalized by the time dependent droplet radius, $r_s(t)$, to give the following normalized equation (see a similar derivation in chapter 2):

$$\frac{\partial C}{\partial t} = \frac{D}{r_s^2(t)}\left(\frac{\partial^2 C}{\partial R^2} + \frac{1}{R}\frac{\partial C}{\partial R}\right) + \frac{R}{r_s(t)}\frac{\partial C}{\partial R}\frac{\partial r_s(t)}{\partial t} \tag{5.2}$$

The assumption that the droplet is evaporating with a constant evaporation rate, κ, as defined by Vehring [2008]; Vehring et al. [2007] can be incorporated mathematically as follows [Gardner, 1965]:

$$d^2(t) = -\kappa t \tag{5.3}$$

$$r_s^2(t) = -\frac{1}{4}\kappa t \tag{5.4}$$

$$\frac{\partial r_s^2(t)}{\partial t} = -\frac{1}{4}\kappa \tag{5.5}$$

Substituting Equation 5.4 and Equation 5.5 in Equation 5.2 and using the definition of the Péclet number, $Pe = \frac{\kappa}{8D}$ [Vehring, 2008; Vehring et al., 2007], Equation 5.2 can be written as follows after normalizing the concentration C:

$$\frac{\partial^2 c}{\partial R^2} + \frac{\partial c}{\partial R}\left[\frac{1}{R} - RPe\right] + 2Pe\frac{\partial c}{\partial t}t = 0 \tag{5.6}$$

At the asymptotic state of a cylindrical droplet, the concentration, c, at any point, R, can be assumed to be proportional to the inverse of the droplet radius, $r_s(t)$, squared. (This is equivalent to saying that all points will have a concentration, c, that is changing with the same rate of the mean concentration, c_m, since the droplet height is constant).

$$c_o r_o^2 = c r_s^2 \tag{5.7}$$

$$c = c_o\left(\frac{r_o}{r_s}\right)^2 \tag{5.8}$$

$$c \propto r_s^{-2} \tag{5.9}$$

For a given constant evaporation rate, κ, the relation between the droplet radius, $r_s(t)$, and time, t, can be derived from Equation 5.4 as follows:

$$r_s^2(t) \propto -t \tag{5.10}$$

From Equation 5.9 and Equation 5.10 the concentration, $c(t)$, at any point, R, in the asymptotic state can be written as follows:

$$c \propto (-t)^{-1} \tag{5.11}$$

$$c = A(-t)^{-1} \tag{5.12}$$

Where: A is a constant.

The term $\left[-t\frac{\partial c}{\partial t}\right]$ in Equation 5.6 can be replaced by a time independent term in the asymptotic state as follows:

$$c = A(-t)^{-1} \tag{5.13}$$

$$\frac{\partial c}{\partial t} = A(-t)^{-2} \tag{5.14}$$

$$-t\frac{\partial c}{\partial t} = A(-t)^{-1} \tag{5.15}$$

$$-t\frac{\partial c}{\partial t} = c \tag{5.16}$$

Substituting Equation 5.16 in Equation 5.6 gives the following equation for the solute concentration at the asymptotic state.

$$\frac{\partial^2 c}{\partial R^2} + \frac{\partial c}{\partial R}\left[\frac{1}{R} - RPe\right] - 2cPe = 0 \tag{5.17}$$

The solution for Equation 5.17 is given by:

$$c(R) = c_{\mathrm{c}} \exp\left[\left(\frac{Pe}{2}\right)R^2\right] \tag{5.18}$$

Where: c_{c} is the concentration at the droplet center (which is time dependent).

The solution satisfies the following two boundary conditions (see chapter 2 for more details):

$$\frac{\partial c}{\partial R} = 0 \quad \text{at } R = 0 \tag{5.19}$$

$$\frac{\partial c}{\partial R} - cPe = 0 \quad \text{at } R = 1 \tag{5.20}$$

The mean concentration, c_{m}, can then be calculated from $c(R)$ as follows:

$$\pi(1)^2 c_{\mathrm{m}} = \int_0^1 c(R) 2\pi R \mathrm{d}R \tag{5.21}$$

$$c_{\mathrm{m}} = 2c_{\mathrm{c}} \int_0^1 R \exp\left[\left(\frac{Pe}{2}\right)R^2\right] \mathrm{d}R \tag{5.22}$$

$$c_{\mathrm{m}} = 2c_{\mathrm{c}}\beta \tag{5.23}$$

$$\beta = \int_0^1 R \exp\left[\left(\frac{Pe}{2}\right)R^2\right] \mathrm{d}R \tag{5.24}$$

In this case, Equation 5.24 can be integrated analytically to calculate β as follows:

$$\beta = \int_0^1 R \exp\left[\left(\frac{Pe}{2}\right)R^2\right] \mathrm{d}R \tag{5.25}$$

$$\beta = \frac{1}{Pe}\int_0^1 PeR\exp\left[\left(\frac{Pe}{2}\right)R^2\right]\mathrm{d}R \tag{5.26}$$

$$\beta = \frac{1}{Pe}\left[\exp\left(\frac{Pe}{2}R^2\right)\right]_0^1 \tag{5.27}$$

$$\beta = \frac{\exp\left(\frac{Pe}{2}\right)-1}{Pe} \tag{5.28}$$

Using Equation 5.23, the concentration, $c(R)$, can be expressed as follows:

$$c(R) = \frac{c_\mathrm{m}}{2\beta}\exp\left[\left(\frac{Pe}{2}\right)R^2\right] \tag{5.29}$$

And the surface concentration, c_s, is obtained at $R = 1$ as follows:

$$c_\mathrm{s} = \frac{c_\mathrm{m}}{2\beta}\exp\left(\frac{Pe}{2}\right) \tag{5.30}$$

Surface enrichment, E, can be calculated from Equation 5.30 as follows:

$$E = \frac{c_\mathrm{s}}{c_\mathrm{m}} = \frac{1}{2\beta}\exp\left(\frac{Pe}{2}\right) \tag{5.31}$$

Substituting the value of β from Equation 5.28 into Equation 5.31 yields the following expression for surface enrichment:

$$E = \frac{c_\mathrm{s}}{c_\mathrm{m}} = \frac{Pe}{2}\frac{\exp\left(\frac{Pe}{2}\right)}{\exp\left(\frac{Pe}{2}\right)-1} \tag{5.32}$$

For high Péclet numbers, Pe, Equation 5.32 can be simplified to the following form:

$$E = \frac{c_\mathrm{s}}{c_\mathrm{m}} \approx \frac{Pe}{2} \tag{5.33}$$

The error in using Equation 5.33 instead of Equation 5.32 can be calculated as follows:

$$e\% = \left|\frac{E_\mathrm{exact} - E_\mathrm{approx}}{E_\mathrm{exact}}\right| \times 100 \tag{5.34}$$

$$e\% = \frac{100}{\exp\left(\frac{Pe}{2}\right)} \tag{5.35}$$

$e\%$ is less than 0.7 % for $Pe \geq 10$.

We can see that although both cases (spherical and cylindrical droplets) have the same radial concentration profiles (i.e., Equation 5.18) surface enrichment, E, is different because the concentration at the droplet center, c_c, is not the same.

5.3 Transient solution

In this section the transient solution for the concentration profile and surface enrichment similar to the ones developed previously for spherical droplets (chapter 2) will be developed .

The importance of the transient solution is twofold. First, to use it as a verification case for the Adaptive Interface Sweeping Method that will be discussed in chapter 6. Second, to validate the asymptotic solution developed in section 5.2. The procedure used is the same one used for spherical droplets but with some modifications.

The one dimensional diffusion equation in cylindrical coordinates (Equation 5.2) can be normalized using the same normalization procedure to yield the following equation:

$$\frac{\partial c}{\partial \tau} = \frac{1}{2Pe(1-\tau)}\left(\frac{\partial^2 c}{\partial R^2} + \frac{1}{R}\frac{\partial c}{\partial R}\right) - \frac{R}{2(1-\tau)}\frac{\partial c}{\partial R} \tag{5.36}$$

The normalized mean concentration, c_m, can also be derived in terms of the normalized time, τ, as follows:

$$c_{\mathrm{m}} = \left(\frac{r_o}{r_s}\right)^2 = (1-\tau)^{-1} \tag{5.37}$$

Transient surface enrichment, $E(\tau)$, can be obtained from the solution of Equation 5.36 and Equation 5.37.

In terms of the saturation ratio, s, Equation 5.36 reads as follows:

$$\frac{\partial s}{\partial \tau} = \frac{1}{2Pe(1-\tau)}\left(\frac{\partial^2 s}{\partial R^2} + \frac{1}{R}\frac{\partial s}{\partial R}\right) - \frac{R}{2(1-\tau)}\frac{\partial s}{\partial R} \tag{5.38}$$

It can also be expressed in terms of the concentration enrichment, e, as follows:

$$\frac{\partial e}{\partial \tau} = \frac{1}{2Pe(1-\tau)}\left(\frac{\partial^2 e}{\partial R^2} + \frac{1}{R}\frac{\partial e}{\partial R}\right) - \frac{R}{2(1-\tau)}\frac{\partial e}{\partial R} - \frac{e}{(1-\tau)} \tag{5.39}$$

5.3.1 Boundary and initial conditions

The same set of boundary and initial conditions used for the spherical droplet (subsection 2.6.1) will be used.

5.3.2 Mass conservation

The same approach developed to check for solute mass conservation (subsection 2.6.2) will be used but with minor modifications.

The total system mass has to be checked every time step during the solution to ensure mass conservation. In the real physical domain of the problem, the domain

is changing with time (i.e., $r_s(t)$) and mass can be simply calculated at each time step as follows:

$$M(t) = \iiint_{v(t)} C \, \mathrm{d}v \tag{5.40}$$

Where: C is the solute concentration.

But since the radial coordinate, r, is normalized, the computational domain is fixed and its volume does not reflect the actual volume of the droplet. An expression has to be derived to express the system mass in terms of the normalized coordinate, R.

Differential mass, $\mathrm{d}M$, can be calculated for an elemental volume, $\mathrm{d}v = r\mathrm{d}r\mathrm{d}\theta\mathrm{d}z$, in cylindrical coordinates as follows:

$$\mathrm{d}M = C(r) \, \mathrm{d}v = C(r) \, r \, \mathrm{d}r \, \mathrm{d}\theta \, \mathrm{d}z \tag{5.41}$$

Since it is only the radial coordinate, r, that was normalized and not the other two coordinates (i.e., θ, z), we can define the mass, m, as follows:

$$\mathrm{d}m = \frac{\mathrm{d}M}{\mathrm{d}\theta\mathrm{d}z} = C(r) r \, \mathrm{d}r \tag{5.42}$$

$$m(t) = \int_0^{r_s(t)} C(r) r \, \mathrm{d}r = \int_0^1 C(R) R r_s(t) \mathrm{d}R \, r_s(t) \tag{5.43}$$

$$m(t) = r_s^2(t) \int_0^1 C(R) R \mathrm{d}R \tag{5.44}$$

Equation 5.44 can be used to calculate the mass at any time, $m(\tau)$, using the concentration, $C(R)$, in the normalized coordinate , R. It can also be used to express the ratio of the mass at any time, $m(\tau)$, to the initial mass, m_o.

$$m_o = r_o^2 \int_0^1 C_o R \, \mathrm{d}R = r_o^2 C_o \int_0^1 R \, \mathrm{d}R = \frac{r_o^2 C_o}{2} \tag{5.45}$$

$$\frac{m(t)}{m_o} = 2 \left(\frac{r_s}{r_o} \right)^2 \int_0^1 \frac{C}{C_o} R \, \mathrm{d}R \tag{5.46}$$

$$\frac{m(\tau)}{m_o} = 2(1-\tau) \int_0^1 \frac{C}{C_o} R \, \mathrm{d}R \tag{5.47}$$

$$\frac{m(\tau)}{m_o} = 2(1-\tau) \int_0^1 cR \, \mathrm{d}R \tag{5.48}$$

Where: c is the normalized concentration, $\frac{C}{C_o}$. Equation 5.48 can be integrated numerically using a zero order integration polynomial as follows:

$$\frac{m(\tau)}{m_o} \approx 2(1-\tau) \sum_{i=0}^{N} c_i R_i \Delta R \tag{5.49}$$

Where: $N+1$ is the number of grid points and ΔR is the grid spacing (i.e., $\Delta R = 1/N$).

Although the ratio given by Equation 5.48 should be unity if mass conservation is achieved, it will be slightly different than unity even if the solution is mass conservative. This is because the accuracy of the numerical integration given by Equation 5.49 depends on the number of grid points, $N+1$, and the integration method. To account for this error, Equation 5.49 has to be corrected to account for the accuracy of the numerical integration used.

We can start by calculating the ratio $\frac{m(0)}{m_o}$ for the initial concentration profile, $c_o(R) = 1$, at time $\tau = 0$ assuming a constant grid spacing, ΔR.

$$\frac{m(0)}{m_o} \approx 2(1-\tau)\sum_{i=0}^{N} c_i R_i \Delta R \tag{5.50}$$

$$\frac{m(0)}{m_o} \approx 2(1-\tau)\Delta R c_o \sum_{i=0}^{N} R_i \tag{5.51}$$

$$R_i = i\Delta R \tag{5.52}$$

$$\frac{m(0)}{m_o} \approx 2(1-\tau)(\Delta R)^2 c_o \sum_{i=0}^{N} i \tag{5.53}$$

$$\Delta R = \frac{1}{N} \tag{5.54}$$

$$\frac{m(0)}{m_o} \approx 2(1-\tau)\frac{1}{N^2} c_o \sum_{i=0}^{N} i \tag{5.55}$$

$$\sum_{i=0}^{N} i = \frac{N(N+1)}{2} \tag{5.56}$$

$$\frac{m(0)}{m_o} \approx 1 + \frac{1}{N} \tag{5.57}$$

Equation 5.57 shows that the ratio calculated by Equation 5.49 is not unity and has to be corrected. The correction factor is a function of the number of grid points used, $N+1$.

5.3.3 Stability considerations

Using an explicit scheme (i.e., first order Euler) for time stepping puts an upper limit on the time step, $\Delta\tau$. The CFL condition can be used to calculate the maximum time step for a stable solution.

First, we need to know the velocity of the convective term. Equation 5.36 will be rewritten by grouping all terms with a fist order spatial derivative together.

$$\frac{\partial c}{\partial \tau} = \frac{1}{2Pe(1-\tau)}\left(\frac{\partial^2 c}{\partial R^2}\right) + \frac{1 - R^2 Pe}{2(1-\tau)RPe}\left(\frac{\partial c}{\partial R}\right) \tag{5.58}$$

By comparing Equation 5.58 to a standard convection-diffusion equation we can write the velocity magnitude of the convective term as follows:

$$||\mathbf{v}_{\text{conv}}|| = \frac{1 - R^2 Pe}{2(1-\tau)RPe} \tag{5.59}$$

The velocity of the convective term depends on the radial coordinate, R, the Péclet number, Pe, and the time at the current time step, τ. Plotting Equation 5.59 shows that for a given Péclet number and time, τ, $||\mathbf{v}_{\text{conv}}||$ is maximum at the droplet center (Figure 5.1).

Since the concentration of the first grid point is calculated from the no flux boundary condition (i.e., Equation 5.19), the solution of Equation 5.36 starts from the second grid point which has a radial coordinate, $R = \Delta R$. The maximum value for $||\mathbf{v}_{\text{conv}}||$ can then be calculated as follows:

$$||\mathbf{v}_{\text{conv,max}}|| = \frac{1 - (\Delta R)^2 Pe}{2(1-\tau)\Delta RPe} \tag{5.60}$$

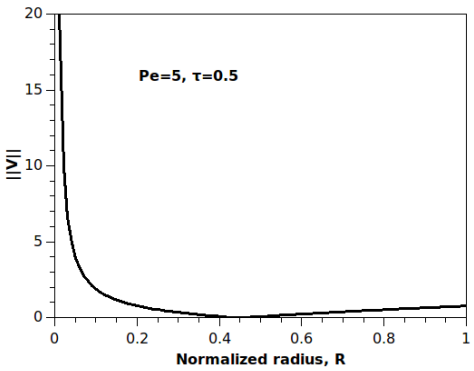

Figure 5.1: Magnitude of the convective term in Equation 5.59 for $Pe = 5$ & $\tau = 0.5$.

Which can be approximated for small values of ΔR as follows:

$$||\mathbf{v}_{\text{conv,max}}|| \approx \frac{1}{2(1-\tau)\Delta RPe} \tag{5.61}$$

The CFL condition is given by:

$$\text{CFL} = \frac{||\mathbf{v}_{\text{conv,max}}||\Delta\tau}{\Delta R} \leq 1 \tag{5.62}$$

$$\text{CFL} = \frac{1 - (\Delta R)^2 Pe}{2(1-\tau)\Delta RPe}\frac{\Delta\tau}{\Delta R} \leq 1 \tag{5.63}$$

$$\text{CFL} \approx \frac{\Delta\tau}{2(1-\tau)(\Delta R)^2 Pe} \leq 1 \tag{5.64}$$

The maximum time step, $\Delta\tau_{\max}$, can be approximated as follows:

$$\Delta\tau_{\max} \approx 2(1-\tau)(\Delta R)^2 Pe \tag{5.65}$$

Comparing Equation 5.65 to Equation 2.100 shows that the spherical droplet case is more restrictive in limiting the maximum stable time step than the cylindrical droplet case (Figure 5.2).

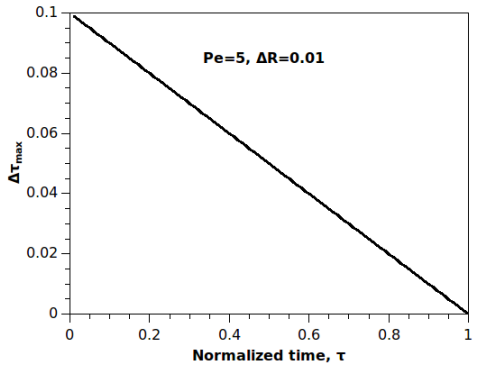

Figure 5.2: Maximum stable time step, $\Delta\tau_{\max}$, for $Pe = 5$ & $\Delta R = 0.01$.

It has to be noted that the CFL condition provides a rough estimate of the minimum time step that can be used for a stable solution. A more accurate estimate can be obtained by using other stability analysis techniques like the matrix stability analysis or von Neumann stability analysis [Moin, 2010].

5.3.4 Results

Equation 5.36 is solved for a wide range of Pe numbers (1-200) and the results show a behavior similar to that of spherical droplets. However, cylindrical droplets seem to take more time to reach the asymptotic state for the concentration profiles or the steady state value for surface enrichment (Figure 5.3).

5.3.5 Asymptotic concentration profiles

The normalized concentration, $\frac{c(R)}{c_{\mathrm{m}}}$, can be calculated using the asymptotic concentration profile as follows (see Equation 5.29):

$$\frac{c(R)}{c_{\mathrm{m}}} = \frac{1}{2\beta} \exp\left[\left(\frac{Pe}{2}\right) R^2\right] \tag{5.66}$$

The transient results for the normalized concentration, $\frac{c(R)}{c_{\mathrm{m}}}$, at $\tau = 0.99$ is compared against the asymptotic state solution given by Equation 5.66 for $Pe = 25$ as shown in Figure 5.4.

The perfect agreement between the results confirms the validity of the predicted asymptotic state solution and the corresponding concentration profiles.

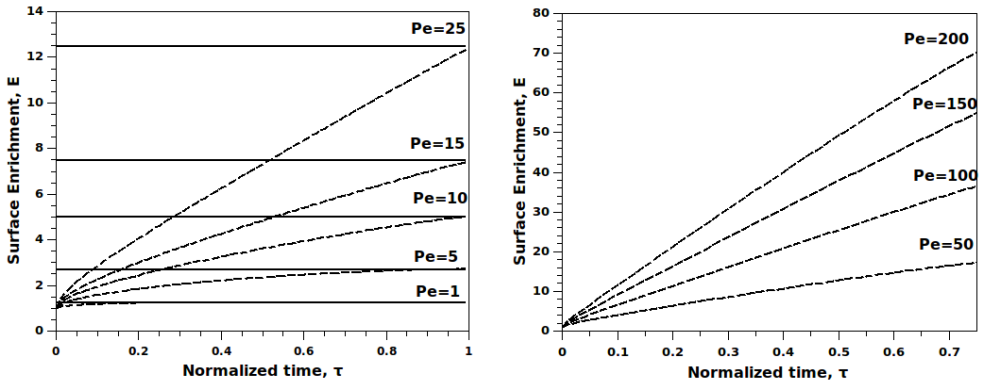

$1 \leq Pe \leq 25$ $\quad$ $50 \leq Pe \leq 200$

Figure 5.3: Evolution of surface enrichment for different Péclet numbers: Transient numerical solution, $E(\tau)$ vs. the steady state value, E_{ss}.

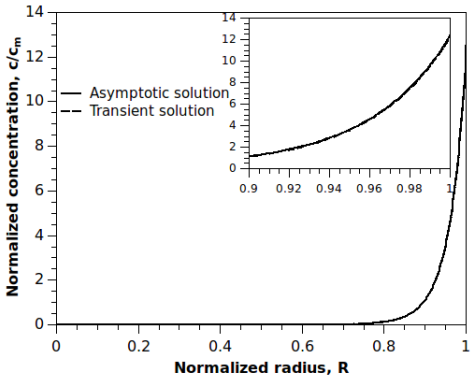

Figure 5.4: Normalized concentration profiles: Transient results at $\tau = 0.99$ vs. Asymptotic state solution for $Pe = 25$.

5.3.6 Steady state surface enrichment

The steady state surface enrichment, E_{ss}, predicted using the asymptotic state assumption is compared against the transient value for surface enrichment, $E(\tau)$, at $\tau = 0.99$. Good agreement can be seen in Figure 5.5.

5.4 Conclusions

All the results derived in the previous sections were verified by solving Equation 5.36. The results confirmed the existence of an asymptotic solution and the corresponding value of surface enrichment, E. The results also confirmed the validity of the analysis done for mass conservation and stability considerations.

Through this chapter it was shown that the same approach used to obtain an asymptotic and transient solution of the concentration profiles for spherical droplets

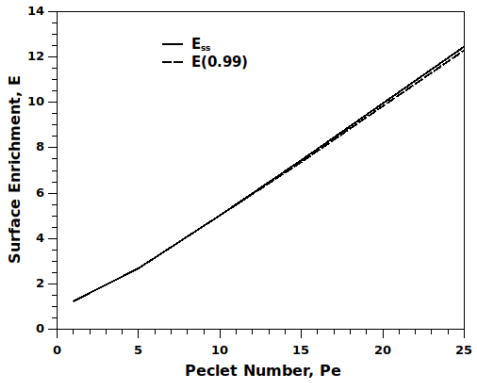

Figure 5.5: Surface enrichment: Transient results at $\tau = 0.99$ vs. Asymptotic state solution.

can be used for cylindrical droplets as well.

The results confirmed the validity of the used assumptions and approximations and will be used to validate the results of the Adaptive Interface Sweeping Method discussed in the next chapter.

Chapter 6

The Adaptive Interface Sweeping Method: Theory

6.1 Introduction

In the development of the simplified particle formation model proposed in chapter 2, it was assumed that both the evaporation rate and the solute properties (i.e., diffusion coefficient, solubility) are constant. These assumptions were necessary to develop the proposed normalization procedure in order to recast the numerical results in a general easy-to-use form for an easy and fast means of designing multi-component layered microparticles in a computationally affordable manner. However, in some cases these assumptions limit the model usability and accuracy.

During the evaporation of solution droplets, the solute surface concentration increases with time and suppresses the solvent vapor pressure on the droplet surface which is the driving force for the evaporation process [Finlay, 2001]. This effect, which becomes more significant in the later stages of evaporation, leads to a decrease in the actual Péclet number and a subsequent decrease in the surface enrichment rate. At the same time the diffusivity of the solute decreases because the molecular mobility drops significantly at higher concentrations.

The effects of variable solvent vapor pressure and solute diffusivity have been incorporated into several numerical models [Seydel et al., 2006; Eslamian et al., 2009; Okuzono et al., 2006; Homer et al., 2009; Handscomb et al., 2009b,a; Jiang et al., 2010; Chen et al., 2011; Vehring et al., 2007] that can take into account the variation in both the evaporation rate and the solute properties.

These models can be generally classified as spherically symmetric models. In these models, the droplet is assumed to be a perfect sphere during the whole evaporation and shell formation process with the subsequent mapping of the physical domain into a one dimensional spherically symmetric domain. This offers many advantages such as lower computational cost for the model and a simplified form for the governing equations. It also allows the normalization of the radial coordinate with the time dependent droplet radius which reduces the variable size domain into a one dimensional fixed size domain and avoids many numerical issues in dealing with moving interfaces.

Different studies also extend this spherical symmetry to different variable fields

outside the evaporating droplet, e.g., velocity, temperature and solvent vapor concentration. Some of these studies solved for these external variable fields using this assumption, while others relied on analytical and semi-analytical predefined solutions to them.

Although spherical symmetry offers an accurate and computationally affordable way of tackling the problem of droplet evaporation, there are some situations that necessitate the use of a non-spherically symmetric model even if the droplet is spherical.

- **Internal circulation**: For droplets with high Reynolds number, Re, (due to large size or high droplet velocities like Pressurized Metered Dose inhalers (pMDIs) [Finlay, 2001]) the solvent internal circulation has to be taken into account when solving for the concentration field.
- **Internal structure**: Formation of particles with non spherically symmetric internal structure [Okuyama et al., 2006b; Okuyama and Lenggoro, 2003; Guterres et al., 2009; Yuk et al., 2012] cannot be modeled. This includes evaporation of suspension/emulsion droplets with more than one component.

Despite the fact that the majority of pharmaceutical aerosols do not fall under the last two categories [Finlay, 2001], recent advances in the design of structured microparticles and the accompanying sophistication in the manufacturing techniques suggest that the majority of these aerosols will shift towards a more complicated morphology [Nandiyanto and Okuyama, 2011].

The purpose of this chapter is to introduce a new numerical method for the calculation of the transient concentration fields of an evaporating solution droplet without the use of the spherical symmetry assumption. This method is a first step toward the development of a more general numerical framework for modeling structured microparticle formation.

6.2 The Adaptive Interface Sweeping Method (AISM)

The proposed Adaptive Interface Sweeping Method (AISM) mimics the physical mechanism responsible for the phenomena of surface enrichment of evaporating solution droplets as explained in section 2.2 [Vehring, 2008; Vehring et al., 2007]. It can predict the evolution of the solute concentration fields during the whole evaporation period under an arbitrary evaporation rate and varying material properties (spatially and temporally).

In the current chapter, the method is developed for a hypothetical cylindrical droplet. The reason for this is to make the problem tractable using reasonable computational resources and to ease the method implementation during the development phase of the model. The extension to the three dimensional case (i.e., spherical droplets) is straightforward.

Assume an initially well mixed solution droplet, that started to evaporate with an evaporation rate, κ. Depending on the relative strength of the diffusional flux and the convective flux resulting from the motion of the droplet surface, a concentration gradient will develop. So at any given position in the droplet, solute molecules will experience the two counteracting mechanisms of diffusion and convection. These two mechanisms act at the same time and modeling their simultaneous effect is a

key factor for a successful modeling approach.

In the case of a spherically symmetric model, the radial coordinate normalization by the droplet radius guarantees that both mechanisms' effects are considered simultaneously (see the boundary conditions given by Equation 2.69). However, if the whole droplet geometry is to be modeled, which does not allow for the radial normalization procedure, another approach has to be used.

The other option is to model the two mechanisms separately. By controlling the way the two mechanisms are modeled, the effect of their simultaneous action can be modeled.

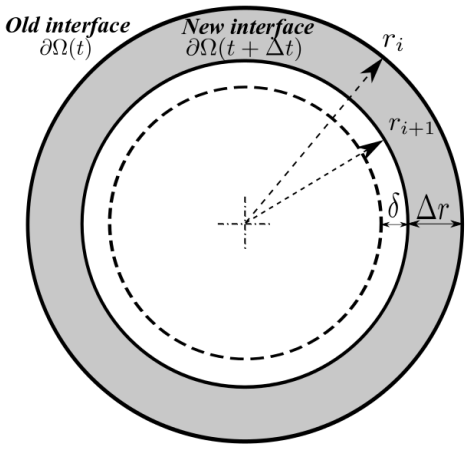

Figure 6.1: A schematic diagram showing the AISM

If the droplet has a radius of r_i at time t (Figure 6.1) after a time increment Δt the new droplet radius is r_{i+1}. During the time interval Δt, the droplet interface changed from the old $\partial\Omega(t)$ to the new $\partial\Omega(t+\Delta t)$ while sweeping the solute molecules towards the new droplet interface. At the same time diffusional flux of solute goes from the droplet interface (which is higher in concentration) to the droplet center (which is lower in concentration).

The AISM splits the two processes, instead of modeling them simultaneously, into the following two steps:

- *Process 1*: The sweeping of the molecules towards the new interface (recession of the droplet surface without solute diffusion).
- *Process 2*: The diffusion of the solute from the interface to the droplet center (diffusion of the solute in a constant diameter droplet).

Process 1: Starting from a droplet of radius r_i and allowing the droplet to evaporate until it reaches a radius r_{i+1}, the solute mass between the two interfaces can be added to the solute mass of the new droplet interface $\partial\Omega(t+\Delta t)$. In this step it is assumed that there is no diffusion taking place during the evaporation.

Process 2: Following the first step, the concentration field in a hypothetically non-evaporating droplet of radius r_{i+1} is allowed to relax to a period of time Δt

that is needed to change the droplet radius by Δr.

The proposed method starts with calculating the time needed to change the droplet radius from r_i to r_{i+1} which can be derived from the instantaneous evaporation rate, $\kappa(t)$, as follows (note that i is a counter for the interface update):

$$\kappa(t) = -\frac{\mathrm{d}d^2}{\mathrm{d}t} = -4\frac{\mathrm{d}r^2}{\mathrm{d}t} \tag{6.1}$$

$$-4\int_{r_i}^{r_{i+1}} \mathrm{d}r^2 = \int_{t_i}^{t_{i+1}} \kappa(t)\mathrm{d}t \tag{6.2}$$

$$t_{i+1} - t_i = \frac{4}{\kappa_i}\left[r_i^2 - r_{i+1}^2\right] \tag{6.3}$$

$$r_{i+1} = r_i - \Delta r \tag{6.4}$$

$$\Delta t = \frac{4}{\kappa_i}\Delta r\left[2r_i - \Delta r\right] \tag{6.5}$$

Equation 6.5 allows the calculation of Δt for a given evaporation rate, κ_i, initial droplet radius, r_i, and a given change in the droplet radius, Δr. Note that κ can be any function of time and not a constant.

The equation can also be recast to allow the calculation of the changes in the droplet radius, Δr, for a given period of time ,Δt, as follows:

$$4\left[r_i^2 - r_{i+1}^2\right] = \kappa_i \Delta t \tag{6.6}$$

$$4\left[r_i - \Delta r\right]^2 = 4r_i^2 - \kappa_i \Delta t \tag{6.7}$$

$$\left[r_i - \Delta r\right]^2 = r_i^2 - \frac{\kappa_i \Delta t}{4} \tag{6.8}$$

$$r_i - \Delta r = \sqrt{r_i^2 - \frac{\kappa_i \Delta t}{4}} \tag{6.9}$$

$$\Delta r = r_i - \sqrt{r_i^2 - \frac{\kappa_i \Delta t}{4}} \tag{6.10}$$

The reason for preferring one form over the other will be explained later in the implementation section.

The solute mass, Δm_{int}, contained between the two interfaces can be calculated as follows:

$$\Delta m_{\mathrm{int}} = \iint_{\Delta\Omega} c(x,y)\,\mathrm{d}x\,\mathrm{d}y \tag{6.11}$$

This mass is distributed on the new interface, $\partial\Omega(t + \Delta t)$, by increasing the interface concentration by Δc_{int}, assuming an interface of thickness δ, as follows:

$$\Delta c_{\mathrm{int}} = \frac{\Delta m_{\mathrm{int}}}{2\pi\delta r_{i+1}} \tag{6.12}$$

The updated interface concentration, c_{int}, is used as an initial condition for the interface before solving for the concentration field. This concentration can be calculated as follows:

$$c_{\text{int}} = c_{\text{int},i} + \Delta c_{\text{int}} \tag{6.13}$$

In the second step, the concentration field inside the droplet is solved assuming a non-evaporating droplet by relaxing the concentration field with the new interface concentration initial condition for a Δt period of time using the standard convection-diffusion equation.

$$\frac{\partial c}{\partial t} = \nabla \left(D \, \nabla c \right) - \mathbf{v} \nabla c \tag{6.14}$$

Note that Equation 6.14 contains a convective term which allows the inclusion of the internal velocity field from internal circulation in the solution of the concentration field. It also allows for a variable diffusion coefficient, D.

These two steps correspond to a single interface update from $\partial\Omega(t)$ to $\partial\Omega(t+\Delta t)$. The two steps can be repeated as many times as required.

The success of this approach depends on the time scales of diffusion and droplet surface recession, which are governed by the diffusion coefficient, D, and the evaporation rate, κ, respectively. The numerical details are discussed subsequently.

The AISM algorithm can be summarized as follows:

Step 1: Start with a droplet radius r_{o}, a uniform solute concentration, c_{o}, a known evaporation rate, $\kappa(t)$ and solute diffusivity, $D(\mathbf{x}, t)$.

Step 2: Calculate the new droplet radius, r_{i+1}, and the corresponding time step, Δt (Equation 6.5 or Equation 6.10).

Step 3: Calculate the initial solute concentration on the new droplet interface (Equation 6.13).

Step 4: Calculate the concentration field by relaxing the current one for a Δt period of time (Equation 6.14).

Step 5: The concentration field at the end of the last step is the required transient concentration field at the new interface.

Step 6: All the previous steps can be repeated as required (e.g., until a predefined droplet radius, r, is reached, a predefined concentration value on the droplet surface is reached or any other criterion).

6.3 Numerical implementation of the AISM

This section details the numerical implementation of the AISM discussed in section 6.2. This includes droplet interface updating and numerical solution of the convection-diffusion equation to obtain the transient concentration field.

6.3.1 Interface updates

The interface update frequency is crucial in obtaining reasonable results as it has to resolve the real-time competing behavior between the velocity of the receding interface and the solute diffusivity. Two alternatives of updating the droplet interface were suggested in section 6.2.

1. Using a predefined change in the droplet radius, Δr (Equation 6.5).

2. Using a predefined time step, Δt (Equation 6.10).

A predefined change in Δr guarantees that the change between the two interfaces $\partial\Omega(t)$ and $\partial\Omega(t + \Delta t)$ can be controlled regardless of the evaporation rate. In contrast, a predefined change in Δt will not control the corresponding change in Δr since it depends on the current droplet radius, r_i, and the time dependent evaporation rate, $\kappa(t)$.

For a very low evaporation rate, $\kappa(t)$, a predefined time step, Δt, might not be enough to cause any changes in the droplet radius, Δr, for a given grid refinement level. On the other hand a high evaporation rate results in a large change in the droplet radius. It will be shown later that Δr should be kept as small as possible for better accuracy. For this reason Equation 6.5 is used to update the droplet interface.

6.3.2 Solving for the concentration field

Equation 6.14 suggests that a robust numerical method has to be used for the calculation of the transient concentration field. The Lattice Boltzmann Method (LBM) is a good candidate due to its superior ability in dealing with complex boundaries and variable material properties [Chen and Doolen, 1998]. The LBM is also well suited for parallelization which makes it the method of choice for computationally demanding problems.

The Lattice Boltzmann Method (LBM) is a discrete meso-scale modeling approach. It relies on solving the Boltzmann Equation in a discrete velocity space. The method has been successfully used to model many computationally challenging problems [Boraey and Epstein, 2010; Aidun and Clausen, 2010].

The computational domain is divided into grid points, i.e., a lattice, and for each lattice location the *Particle Velocity Distribution Function* (PDF) reflects the fraction of fictitious particles at that location moving in a certain direction with a specific velocity at a given time instant.

By initializing the particle distribution functions at all lattice sites and allowing these particles to *stream* to neighboring lattice nodes and *collide* with others coming from different directions according to a set of predetermined streaming and collision rules, the macro-scale behavior of the convection-diffusion equation can be retrieved.

The discretized Boltzmann equation is given by:

$$g_\alpha(\mathbf{x} + \mathbf{e}_\alpha \Delta t, t + \Delta t) - g_\alpha(\mathbf{x}, t) = \Omega \tag{6.15}$$

Where: $g_\alpha(\mathbf{x}, t)$ is the particle distribution function in the direction α at lattice node $\mathbf{x}$ at time t and Ω is the collision operator which when replaced by the BGK

(Bhatnagar-Gross-Krook) collision operator [Bhatnagar et al., 1954],

$$\Omega = -\left[\frac{g_\alpha(\mathbf{x},t) - g_\alpha^{eq}(\mathbf{x},t)}{\tau_g}\right] \tag{6.16}$$

results in the following PDF evolution equation:

$$g_\alpha(\mathbf{x}+\mathbf{e}_\alpha\Delta t, t+\Delta t) = g_\alpha(\mathbf{x},t) - \left[\frac{g_\alpha(\mathbf{x},t) - g_\alpha^{\mathrm{eq}}(\mathbf{x},t)}{\tau_{\mathrm{g}}}\right] \tag{6.17}$$

g_α^{eq} is the local equilibrium distribution function given by:

$$g_\alpha^{\mathrm{eq}}(\mathbf{x},t) = \omega_\alpha c(\mathbf{x},t)\left[1 + \frac{3\mathbf{e}_\alpha.\mathbf{U}(\mathbf{x},t)}{c_{\mathrm{ss}}^2\ e^2}\right] \tag{6.18}$$

Where: **U** is the flow velocity in the lattice Boltzmann units. The first term in the brackets represents the diffusive flux while the second term is the convective one.

The solute concentration, c, can be calculated from g_α as follows:

$$c(\mathbf{x},t) = \sum_{\alpha=0}^{n} g_\alpha(\mathbf{x},t) \tag{6.19}$$

and the solute diffusivity, D, is given by:

$$D = c_{\mathrm{ss}}^2\left(\tau_{\mathrm{g}} - \frac{1}{2}\right) \tag{6.20}$$

Where: c_{ss} is the lattice speed of sound.

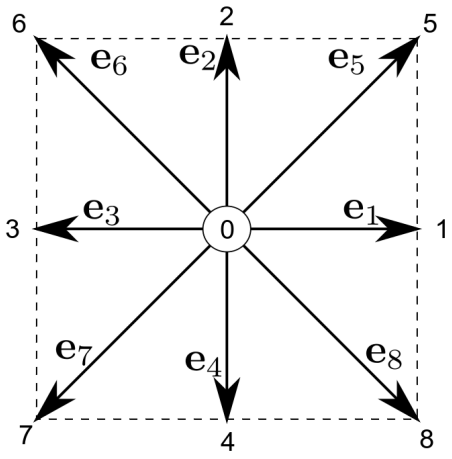

Figure 6.2: The D2Q9 lattice configuration

For the two dimensional, nine speed, i.e., D2Q9, lattice configuration shown in Figure 6.2, $c_{ss} = 1/3$ and ω_α is given by:

$$\omega_\alpha = \begin{cases} 4/9 & \alpha = 0 \\ 1/9 & \alpha = 1,2,3,4 \\ 1/36 & \alpha = 5,6,7,8 \end{cases} \tag{6.21}$$

At the beginning of the simulation, the initial concentration field, c_o, represents a uniform well mixed droplet and is used to calculate the initial PDF as follows:

$$g_\alpha(\mathbf{x}, 0) = \omega_\alpha c_o \quad \text{at } \Omega(0) \tag{6.22}$$

Before solving for the concentration field at each interface update, the concentration at the new interface, c_{int}, (calculated using Equation 6.13) is set as an initial condition for the interface cells as follows:

$$g_\alpha(\mathbf{x}, t) = \omega_\alpha c_{int} \quad \text{at } \partial\Omega(t + \Delta t) \tag{6.23}$$

$$g_\alpha(\mathbf{x}, t) = \omega_\alpha \left[c_{int,i} + \Delta c_{int}\right] \quad \text{at } \partial\Omega(t + \Delta t) \tag{6.24}$$

During the solution of the concentration field, the droplet is assumed to have a constant radius (i.e., non-evaporating) and the boundary condition given by Equation 2.68 reduces to the no flux boundary condition.

$$\frac{\partial c}{\partial r} = 0 \tag{6.25}$$

This boundary condition is implemented by applying the full-way bounce back condition for all the cells outside the new droplet interface.

6.4 On the optimal selection of the AISM parameters

As has been discussed before, the AISM models the surface recession and diffusion processes separately. This necessitates the fine tuning of the method parameters to make it as close as possible to their real simultaneous effects. In this section, the optimal selection of different simulation parameters is discussed.

6.4.1 The change in the droplet radius, Δr, between interface updates

The change in the droplet radius, Δr, is an input parameter for the AISM. The accuracy of the predicted transient concentration fields will depend on it (for a given grid refinement level). Δr has to be kept to a minimum for an accurate prediction of the transient concentration fields. Large Δr results in an underestimation of the calculated concentration field because of a higher concentration gradient at the droplet surface (Equation 6.11) which is the driving force for the diffusion and a longer time, Δt, for the concentration field to relax.

In the model results, it will be shown that Δr affects the predicted concentration field even if other simulation parameters are kept the same. For all reported results Δr was set to one computational cell.

6.4.2 The minimum number of time steps, n_{int}, between interface updates

To relax the concentration field, the transient convection-diffusion equation has to be solved for a Δt period of time . In the LBM, this physical time step corresponds to a number of time steps, n_{int}, between interface updates. The LBM iterates for n_{int} number of time steps to represent the physical Δt. Since n_{int} is generally not an integer, it has to be rounded up or down to produce an integer number of iterations.

For a given evaporation rate, κ, a change in the droplet radius, Δr, and a corresponding Δm_{int}, if the number of iterations is rounded down, this will be equivalent to a higher evaporation rate (Equation 6.5) which will overestimate the concentration values. On the other hand, if n_{int} is rounded up, this will give the effect of a lower evaporation rate and consequently an underestimated concentration fields. Because of the underestimation effect of the concentration due to a large Δr (or a coarse grid) as explained in the previous section, it is better to round the number of iterations down to counteract that effect.

The calculated number of iterations using Equation 6.5 can be written as follows:

$$n_{\text{int}} = A + B \tag{6.26}$$

Where: A is the integer part which will be used during the relaxation step of the concentration field (since n_{int} is rounded down) while B is the real part that will be ignored. The simulated evaporation rate, κ_{sim}, and the real one, κ_{rel}, for a single interface update can be calculated as follows:

$$\kappa_{\text{sim}} = \frac{4}{A}\left[r_i^2 - r_{i+1}^2\right] \tag{6.27}$$

$$\kappa_{\text{rel}} = \frac{4}{A+B}\left[r_i^2 - r_{i+1}^2\right] \tag{6.28}$$

The error in the simulated evaporation rate for a single interface update, e_κ, can then be calculated as follows:

$$e_\kappa = \left|\frac{\kappa_{\text{rel}} - \kappa_{\text{sim}}}{\kappa_{\text{rel}}}\right| \tag{6.29}$$

$$e_\kappa = \frac{B}{A} \tag{6.30}$$

Since B is the real part of n_{int}, its maximum value is ~ 1 and the maximum error in the simulated evaporation rate is give by:

$$e_{\kappa,\max} \sim \frac{1}{A} \tag{6.31}$$

Equation 6.31 is the maximum error in a single interface update. Even if this error is small, a large number of interface updates, N, will cause an overestimation of the concentration values especially at latter stages of the simulation. It is desired to keep this error below a certain value by limiting the minimum n_{int} during the whole simulation period.

n_{int} can be calculated from Equation 6.5 using Lattice Boltzmann units as follows:

$$n_{\text{int}} = \frac{4}{\kappa_i}\Delta r\,[2r_i - \Delta r] \tag{6.32}$$

n_{int} should not drop below a predefined minimum value $n_{\text{int,min}}$ at any instant during the whole simulation period to minimize the effect of rounding the number of iterations.

$$n_{\text{int}} \geq n_{\text{int,min}} \tag{6.33}$$

If the evaporation rate, κ_i, is known in advance, Equation 6.32 can be used to check that the condition given by Equation 6.33 is satisfied. If κ_i is not known (e.g., function of the simulation results), this condition has to be checked during the simulation.

If the condition of Equation 6.33 is not satisfied, further grid refinement is required to satisfy it. This can be shown by considering a case of a constant evaporation rate, κ. For a constant evaporation rate, the minimum number of iterations occurs at the final interface update (i.e., $r_{i+1} = r_{\text{N}}$) and is given by:

$$n_{\text{int}} = \frac{4}{\kappa}\Delta r\,[2r_{\text{N}-1} - \Delta r] \tag{6.34}$$

$$n_{\text{int}} = \frac{4}{\kappa}\Delta r\,[2r_{\text{N}} + \Delta r] \tag{6.35}$$

Where: N is the number of interface updates. The final droplet radius, r_{N}, can be related to the initial radius, r_{o}, as follows:

$$r_{\text{N}} = r_{\text{o}} - N\,\Delta r \tag{6.36}$$

n_{int} can be expressed as a function of the initial droplet radius, r_{o}, as follows:

$$n_{\text{int}} = \frac{4\Delta r}{\kappa}\,[2r_{\text{o}} - 2N\Delta r + \Delta r] \tag{6.37}$$

Equation 6.37 shows that a finer grid (i.e., more points to represent the initial droplet radius, r_{o}) results in a higher n_{int}. The number of grid points needed for the initial droplet (in Lattice Boltzmann units) can be derived as follows:

$$d_{\text{o}} = \frac{\kappa\, n_{\text{int}}}{4\Delta r} + \Delta r\,[2N - 1] \tag{6.38}$$

And the minimum number of grid points to represent the initial droplet diameter, d_{o}, for a given $n_{\text{int,min}}$ is given by:

$$d_{\text{o}} = \frac{\kappa\, n_{\text{int,min}}}{4\Delta r} + \Delta r\,[2N - 1] \tag{6.39}$$

For the most conservative selection of $\Delta r = 1$, Equation 6.39 becomes:

$$d_{\text{o}} = \frac{\kappa\, n_{\text{int,min}}}{4} + 2N - 1 \tag{6.40}$$

$$d_{\text{o}} \approx \frac{\kappa\, n_{\text{int,min}}}{4} + 2N \tag{6.41}$$

Equation 6.41 represents the minimum number of points needed to represents the initial droplet (i.e., grid size) in order to satisfy the condition given by Equation 6.33 to minimize the error in the simulated evaporation rate. It is worth mentioning that this condition is not a substitute for a grid convergence study.

6.4.3 Grid convergence

Solving for the transient concentration fields using the AISM requires careful consideration of the grid convergence. As the droplet evaporates, the number of grid points representing the droplet geometry decreases while concentration gradients increase. So, it can be expected that the size of the used grid will depend on the evaporation rate and the final simulation time. A grid convergence study has to be performed for each case since the results can not be generalized as it depends on many parameters governing the problem at hand.

However, Equation 6.41 is a good starting point for a grid convergence study since it takes into account the evaporation rate, κ, and the final simulation time (represented by N) in calculating the minimum number of grid point used to represent the initial droplet diameter, d_{o}.

Generally speaking, Equation 6.41 is more conservative than the results of the grid convergence study for high evaporation rates (assuming κ is constant). But a grid convergence study is still needed since the evaporation rate is generally variable.

6.4.4 Interface concentration, c_{int}, between interface updates

Implementing *Step 3* of the AISM algorithm requires the imposition of the solute surface concentration, c_{int}, as an initial condition before relaxing the concentration field for each interface update.

Instead of updating the droplet surface concentration at the beginning of the relaxation step for each interface update (Equation 6.23), it can be updated at each time step during the relaxation stage of the algorithm. In this case the Δm_{int} calculated using Equation 6.11 is divided by the number of time steps n_{int} to calculate the solute concentration that will be imposed at each time step of n_{int}. Δm_{int} is divided by the rounded number of iterations to conserve the solute mass.

At each iteration, j, the interface concentration for the next iteration, $j+1$, can now be written as follows (i denotes the interface update counter while j is the iteration counter for a given interface update i).

$$c_{\mathrm{int}}^{j+1} = c_{\mathrm{int,i}}^{j} + \frac{\Delta c_{\mathrm{int}}}{\mathrm{Int}(n_{\mathrm{int}})} \tag{6.42}$$

$$g_{\alpha}^{j+1}(\mathbf{x},t) = \omega_{\alpha} c_{\mathrm{int}}^{j+1} \quad \text{at } \partial\Omega(t+\Delta t) \tag{6.43}$$

So at each iteration of n_{int} a concentration increment of $\frac{\Delta c_{\mathrm{int}}}{\mathrm{Int}(n_{\mathrm{int}})}$ is added to the previous iteration's concentration. This also helps is minimizing the effect of large values of Δr or the use of a coarse grid as discussed in subsection 6.4.1.

6.5 Mass conservation

The conservation of mass can be checked by comparing the solute mass at a given time, $m(t)$, to the initial mass, m_o. The error in mass conservation can be calculated as follows:

$$e_\mathrm{m} = \frac{m(t) - m_\mathrm{o}}{m_\mathrm{o}} \tag{6.44}$$

$$e_\mathrm{m} = \frac{m(t)}{m_\mathrm{o}} - 1 \tag{6.45}$$

$m(t)$ and m_o can be calculated as follows:

$$m(t) = \iint\limits_{\Omega(t)} c(t, x, y)\,\mathrm{d}x\,\mathrm{d}y \tag{6.46}$$

$$m_\mathrm{o} = \frac{\pi}{4}\, c_\mathrm{o}\, d_\mathrm{o}^2 \tag{6.47}$$

e_m has to be checked at each time step to ensure the conservation of mass.

6.6 Conclusions

A new approach is proposed for calculating the transient concentration fields of an evaporating solution droplet. The Adaptive Interface Sweeping Method can predict the concentration field of different solutes in an evaporating solution droplet. Variable evaporation rate and material properties can be taken into account. The method relies on updating the droplet interface using an adaptive approach rather than updating it after a constant time step.

Chapter 7

The Adaptive Interface Sweeping Method: Validation & Results

7.1 Introduction

The results of the proposed Adaptive Interface Sweeping Method (chapter 6) will be presented here. The chapter starts with the validation of the results using the asymptotic state solution then the transient solution, both derived in chapter 5. Some cases for variable evaporation rate and material properties are given to show the ability of the proposed approach to deal with these cases.

For all simulation cases, the error in mass conservation, e_{m}, as defined by Equation 6.45 was checked and was less than 0.0007.

7.2 Validation

In this section, the results of the AISM are compared against the analytical asymptotic state solution and the numerical transient solution of radial concentration profiles of an evaporating cylindrical solution droplet. This validation step is necessary before the AISM can be used for the general cases of variable evaporation rate and material properties.

7.2.1 Asymptotic concentration profiles

The results of the AISM are compared against the asymptotic state solution derived in chapter 5. The normalized radial concentration profiles, $\frac{c(R)}{c_{\mathrm{m}}}$, can be derived from the asymptotic solution as follows:

$$\frac{c(R)}{c_{\mathrm{m}}} = \frac{1}{2\beta}\exp\left[\left(\frac{Pe}{2}\right)R^2\right] \tag{7.1}$$

It is clear from Figure 5.3 that the asymptotic state is reached for cylindrical solution droplet in less than 90 % of the droplet lifetime (i.e., τ <0.9) for Péclet

numbers of 5 or less.

Figure 7.1 shows the normalized radial concentration profiles for two Péclet numbers compared to the asymptotic state profiles calculated using Equation 7.1.

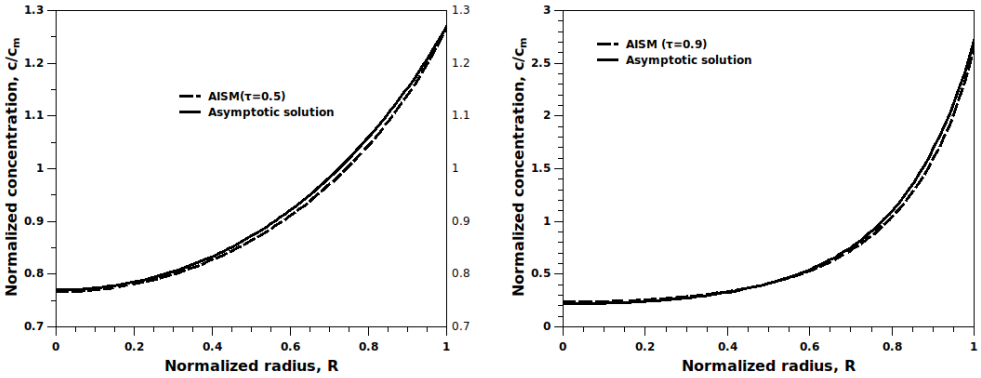

$Pe = 1$ $Pe = 5$

Figure 7.1: Normalized concentration profiles: AISM vs. Asymptotic state solution.

It is clear that the AISM can accurately predict the asymptotic state concentration profile given by Equation 7.1.

7.2.2 Steady state surface enrichment

The evolution of surface enrichment, $E(\tau)$, is plotted against the steady state values of surface enrichment, E_{ss}, given by Equation 5.32 as follows:

$$E_{\text{ss}} = \frac{c_{\text{s}}}{c_{\text{m}}} = \frac{Pe}{2} \frac{\exp\left(\frac{Pe}{2}\right)}{\exp\left(\frac{Pe}{2}\right) - 1} \tag{7.2}$$

The steady state surface enrichment, E_{ss}, is reached around $\tau = 0.3$ for $Pe = 1$ and at $\tau = 0.9$ for $Pe = 5$ as can be seen from Figure 5.3.

7.2.3 Transient concentration profiles

The calculated transient concentration profiles using the AISM are compared against the profiles calculated by the numerical solution of the normalized diffusion equation given in chapter 5 for different Péclet numbers at different times during the evaporation process.

Figure 7.3 and Figure 7.4 show a good agreement between the AISM results and the numerical ones for different cases.

7.2.4 Transient surface enrichment

The evolution of surface enrichment, $E(\tau)$, of the AISM is compared against the transient solution as shown in Figure 7.5 and Figure 7.6.

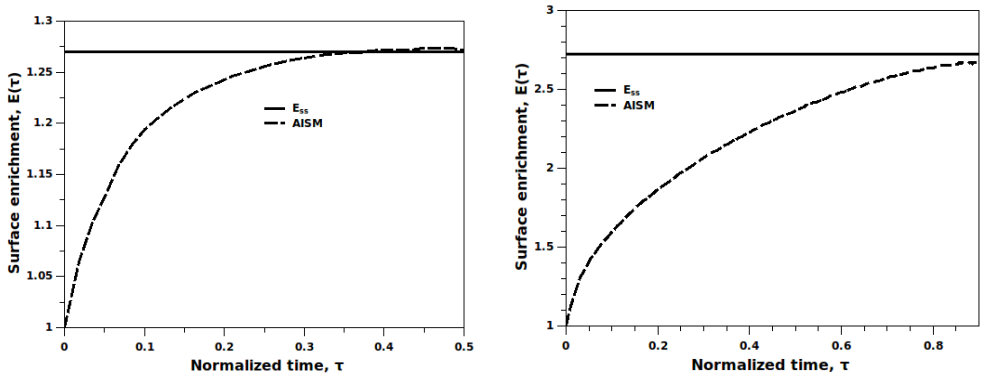

$Pe = 1$ $Pe = 5$

Figure 7.2: Evolution of surface enrichment: AISM vs. Steady state value, E_{ss}.

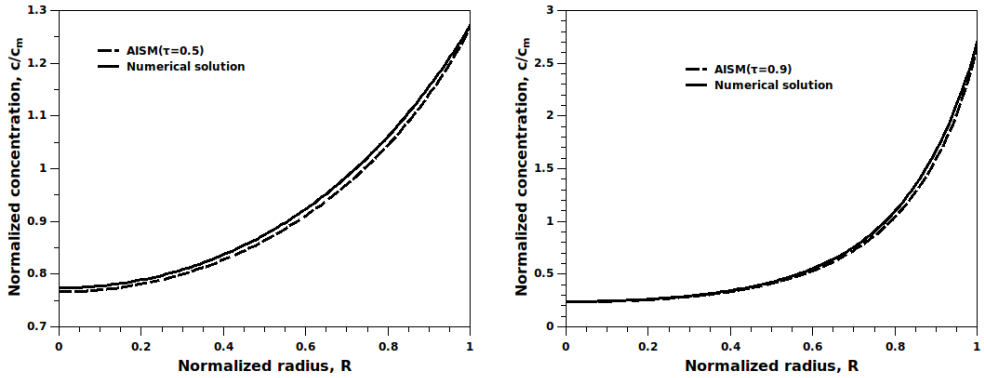

$Pe = 1$ & $\tau = 0.5$ $Pe = 5$ & $\tau = 0.9$

Figure 7.3: Transient concentration profiles for cylindrical solution droplets: the AISM vs. the numerical solution given in chapter 5 for $Pe = 1$ & 5.

Good agreement between the numerical solution and the AISM can be seen from both figures.

7.2.5 Preservation of the circular symmetry

The AISM was mainly developed to deal with problems where the spherical symmetry assumption breaks down for the required solution variables, i.e., concentration and velocity fields, (section 6.1). However, for problems where this assumption is still valid, like the cases discussed in this chapter, the method should preserve this symmetry.

Radial normalized concentration profiles can not be used to check for this, instead normalized concentration contours are used. Figure 7.7 shows the contours for the normalized concentration, $\frac{c}{c_{\mathrm{m}}}$, for two Péclet numbers at different evaporation times.

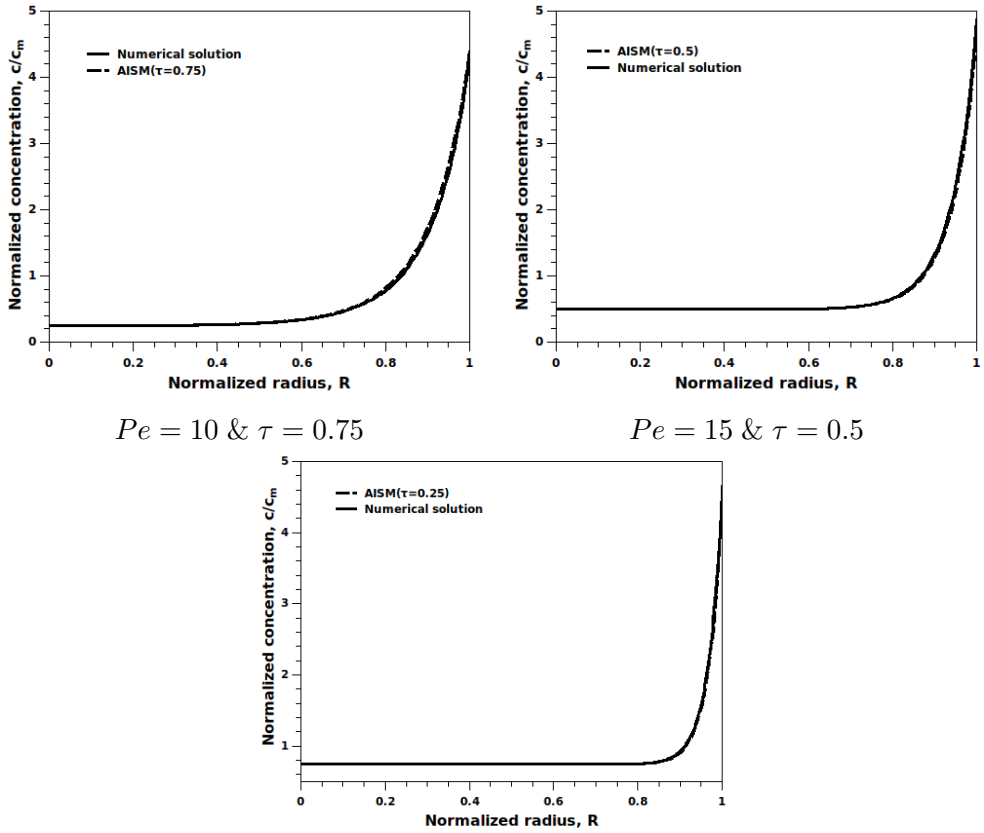

$Pe = 10$ & $\tau = 0.75$ $Pe = 15$ & $\tau = 0.5$

$Pe = 25$ & $\tau = 0.25$

Figure 7.4: Transient concentration profiles for cylindrical solution droplets: the AISM vs. the numerical solution given in chapter 5 for $Pe = 10$, 15 & 25.

It is clear that the AISM can preserve the symmetry of the transient concentration profiles for cases where the problem physically possesses circular symmetry.

7.3 Selection of the AISM parameters

In this section, the effect of selecting different parameters of the AISM is demonstrated as compared to the analysis given in section 6.4.

7.3.1 The change in the droplet radius, Δr

In subsection 6.4.1 is was concluded that for a given grid size (i.e., level of grid refinement) the change in the droplet radius, Δr, has to be kept to the minimum.

The solution for the case of $Pe = 10$ is repeated with different values for Δr and compared against the numerical solution up to $\tau = 0.5$. Figure 7.8 shows the radial concentration profiles at $\tau = 0.5$ and transient surface enrichment, $E(\tau)$. As Δr increases the surface concentration becomes increasingly underestimated as

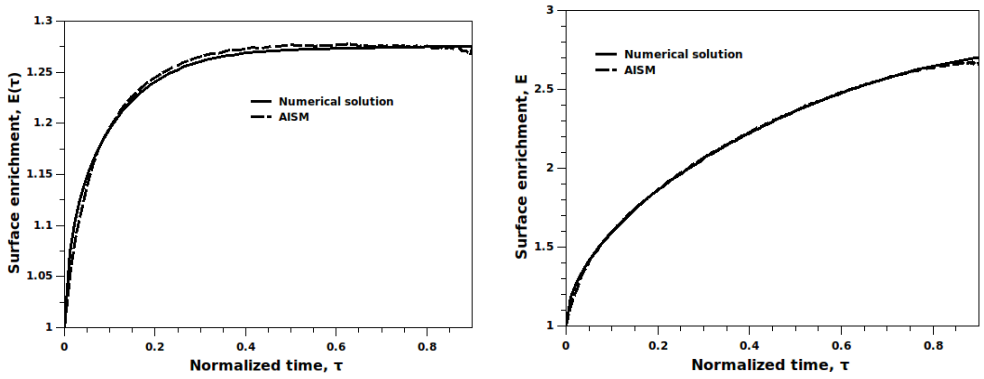

$Pe = 1$ $Pe = 5$

Figure 7.5: Evolution of surface enrichment for cylindrical solution droplets: the AISM vs. the numerical solution given in chapter 5 for $Pe = 1$ & 5.

predicted in subsection 6.4.1. This becomes more clear by looking at the evolution of surface enrichment. The case with the smallest Δr is the closest to the correct numerical solution.

7.3.2 The minimum number of time steps, n_{int}

In subsection 6.4.2 it was shown that the number of time steps between interface updates, n_{int}, has to be kept above a minimum value, $n_{\text{int,min}}$, for an accurate prediction of the transient concentration profiles.

Figure 7.9 shows the normalized concentration profiles and surface enrichment for different $n_{\text{int,min}}$ values for the case of $Pe = 10$. As predicted in subsection 6.4.2, a smaller $n_{\text{int,min}}$ overestimates the concentration profiles.

7.3.3 Grid convergence

The numerical solution of any problem should be grid independent. In subsection 6.4.3 is was shown that the condition for $n_{\text{int,min}}$ is a good starting point for a grid convergence test.

Figure 7.10 shows the solution for the $Pe = 10$ with different level of grid refinement. It is clear that after a certain level of grid refinement, the solution does not change.

7.4 Results

In section 7.2 the results of the AISM were validated using the analytical and numerical solutions presented previously (chapter 5). Different parameters controlling the accuracy of the results of the AISM were investigated in section 7.3. In this section, the results for cases with variable evaporation rate, κ, and variable diffusion coefficient, D, are presented. None of these cases can be solved using the approach

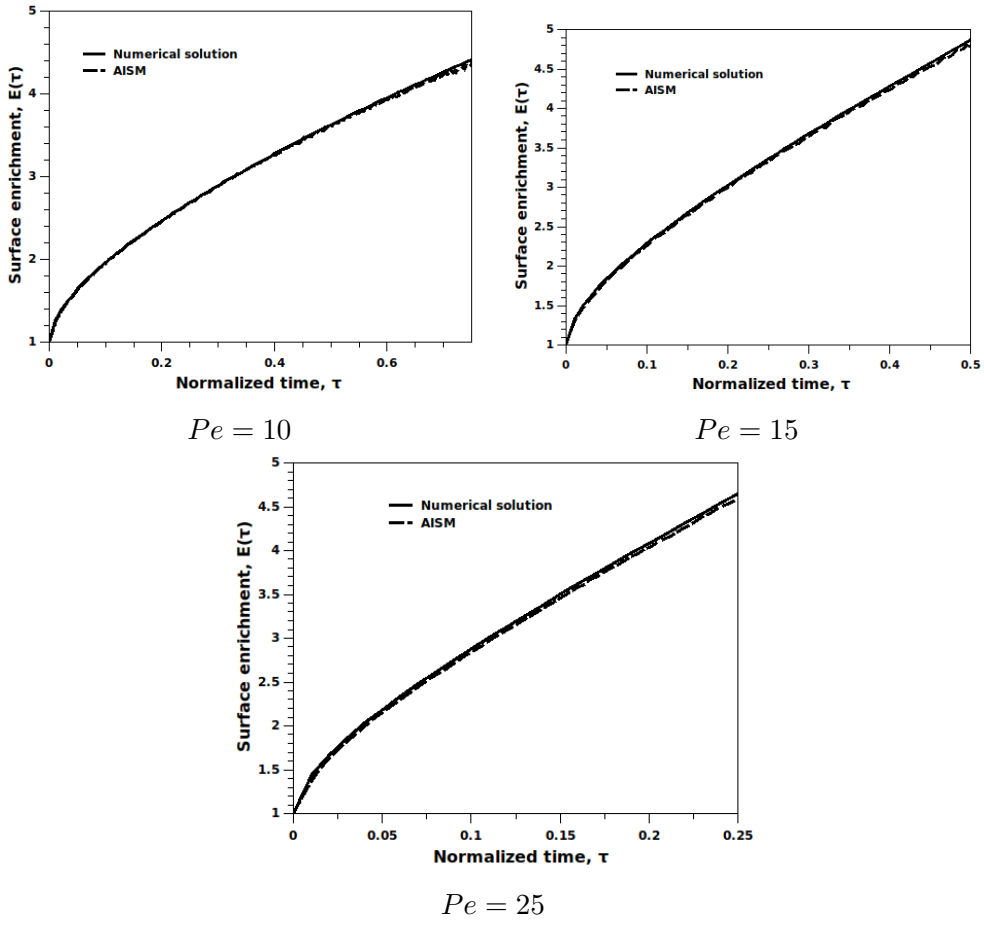

Figure 7.6: Evolution of surface enrichment for cylindrical solution droplets: the AISM vs. the numerical solution given in chapter 5 for Pe = 10, 15 & 25.

proposed in chapter 2. This was one of the motives behind the development of the AISM as discussed in chapter 6.

7.4.1 Variable evaporation rate, $\kappa(c_s)$

The simplified particle formation theory presented in chapter 2 assumes a constant evaporation rate, κ. Maxwell's equation predicts a constant evaporation rate for the case of a pure liquid droplet in a sufficiently large domain with constant material properties [Finlay, 2001].

In real evaporation processes, some of the simplifying assumptions used in the derivation of Maxwell's equation are not satisfied. In addition, most of the industrial evaporation processes are for multi-component solvents and non-pure solutions. A simple representation for the effect of solutes on the evaporation rate is given by Raoult's law [Finlay, 2001]. In this section, a case of an evaporating solution droplet with variable evaporation rate is presented.

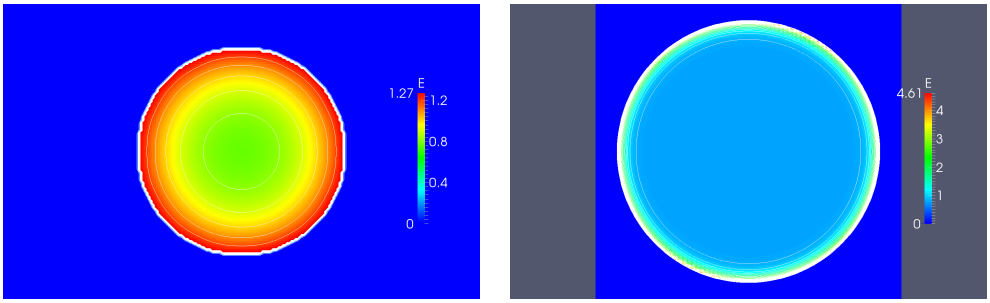

$Pe = 1$ & $\tau = 0.9$ $Pe = 25$ & $\tau = 0.25$

Figure 7.7: Normalized concentration, $\frac{c}{c_m}$, contours for a cylindrical droplet.

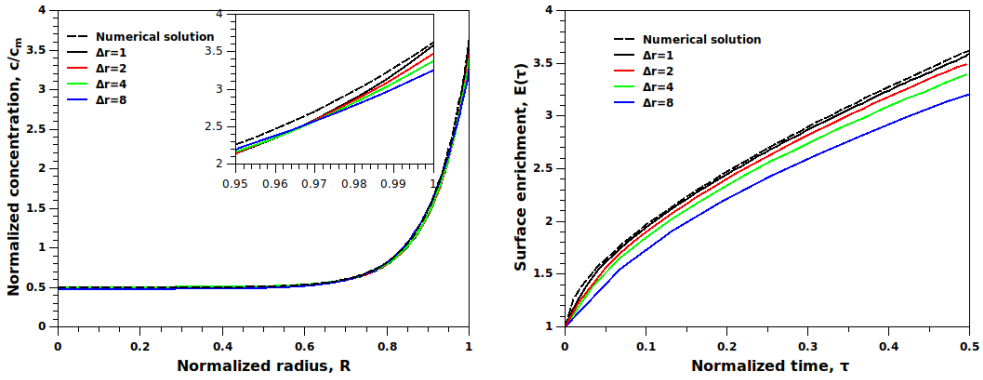

Figure 7.8: The effect of Δr on the accuracy of the AISM for $Pe = 10$.

Assuming a variable evaporation rate that is surface concentration dependent as follows:

$$\kappa(c_s) = \kappa_o \, e^{-\lambda_\kappa (c_s - 1)} \tag{7.3}$$

Where: κ_o is the initial evaporation rate at the beginning of the evaporation process, c_s is the normalized solute surface concentration and λ_κ is a solute dependent dimensionless decay rate. Although the relation between the evaporation rate and the solute surface concentration depends on the type of the solute [Finlay, 2001] and may be more complicated than the proposed relation, Equation 7.3 can capture the two-way coupling between the evaporation rate, κ, and the solute surface concentration, c_s.

As the droplet evaporates according to the initial evaporation rate, κ_o, a concentration profile develops and c_s increases. This increase suppresses the evaporation rate and results in a lower rate of increase for c_s.

An evaporating solution droplet with an initial Péclet number of 10 based on the initial evaporation rate, κ_o, and a constant diffusion coefficient, D, evaporates with a variable evaporation rate given by Equation 7.3 and $\lambda_\kappa = 0.1$ which results in a variable Péclet number evaporation process. As the evaporation rate decreases the Péclet number decreases and the simulation continued until the Péclet number

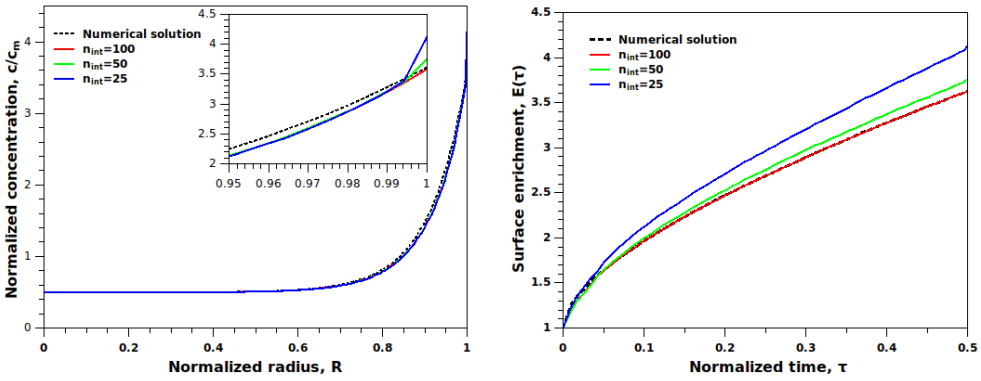

Figure 7.9: The effect of $n_{\text{int,min}}$ on the accuracy of the AISM for $Pe = 10$.

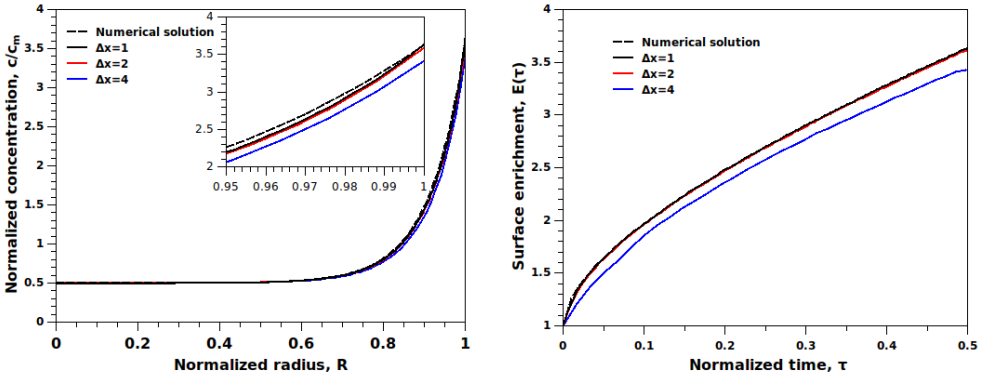

Figure 7.10: Grid convergence test for the AISM for $Pe = 10$.

drops to 5. Figure 7.11 shows the variation of the Péclet number during the evaporation process.

The variable evaporation rate case does not have an analytical or numerical solution. The results were compared against the two limiting Péclet numbers of 5 and 10. Figure 7.12 shows the transient surface enrichment and the normalized surface concentration for the variable evaporation rate case. It can be seen that the surface enrichment increases then decreases. Surface enrichment, E, (right panel) is not to be confused with surface concentration which always increases, (left panel).

It can be seen that for both the surface enrichment, E, and surface concentration, c_{s}, the solution for the variable evaporation rate is bound by the two solutions for $Pe = 5$ and 10. The values of E and c_{s} at the final value of the reduced droplet diameter, $\frac{d}{d_{\text{o}}}$, is higher than the corresponding values for the case of $Pe = 5$ because of the effect of higher evaporation rate, κ, at the beginning of the evaporation process. The trends change from being close to the case of $Pe = 10$ to being close to the case of $Pe = 5$ as the evaporation proceeds.

Since the results of the constant Pe number cases are given as a function of the

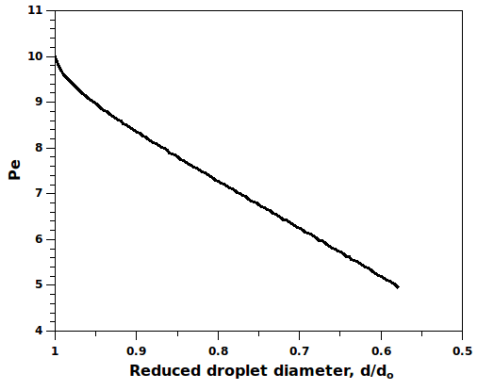

Figure 7.11: Evolution of the Péclet number during evaporation with a variable evaporation rate for an initial Péclet number of 10 and $\lambda_\kappa = 0.1$.

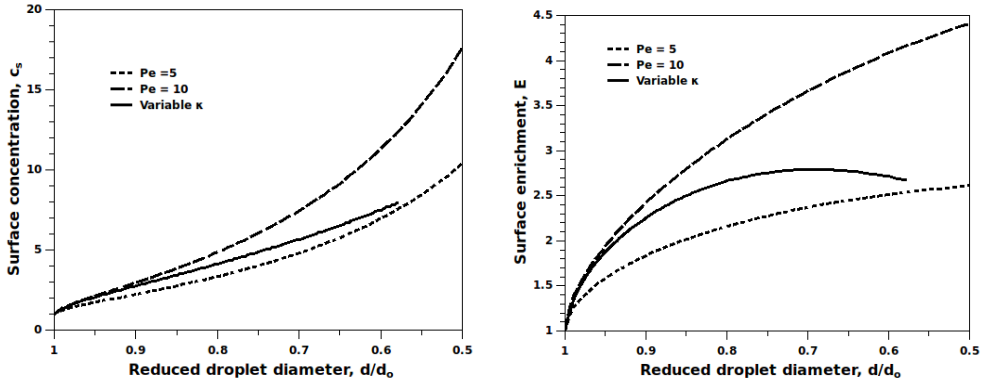

Figure 7.12: Evaporation with a variable evaporation rate, $\kappa(c_\mathrm{s})$, for an initial Péclet number of 10 and $\lambda_\kappa = 0.1$.

normalized evaporation time, τ, while the results of the variable evaporation rate are given as a function of the reduced droplet diameter, $\frac{d}{d_\mathrm{o}}$, (since the droplet lifetime τ_D is not known), the results for the cases of constant Pe numbers were converted as follows:

$$\frac{d(\tau)}{d_\mathrm{o}} = \sqrt{1-\tau} \tag{7.4}$$

7.4.2 Variable diffusion coefficient, $D(c)$

The case of variable material properties provides another example of the limitations of the model discussed in chapter 2. Normally the solute diffusivity is concentration dependent. Solubility and critical super saturation values are also temperature dependent.

In this section, a case of droplet evaporating with a variable diffusivity, $D(c)$,

is solved using the proposed AISM. The initial droplet is well mixed with initial concentration, c_o, initial diffusivity, D_o, and initial Péclet number, $Pe = 10$. The evaporation rate was kept constant while the diffusivity is allowed to change as a function of the concentration as follows:

$$D(c) = D_o \, e^{-\lambda_D (c-1)} \tag{7.5}$$

Where: c is the normalized local solute concentration and λ_D is a solute dependent dimensionless decay rate. The definition of the Péclet number is not valid in this case since the diffusivity will change spatially in addition to its temporal change. Figure 7.13 shows the evolution of surface enrichment and the normalized concentration profiles at the final simulation time of $\tau = 0.5$.

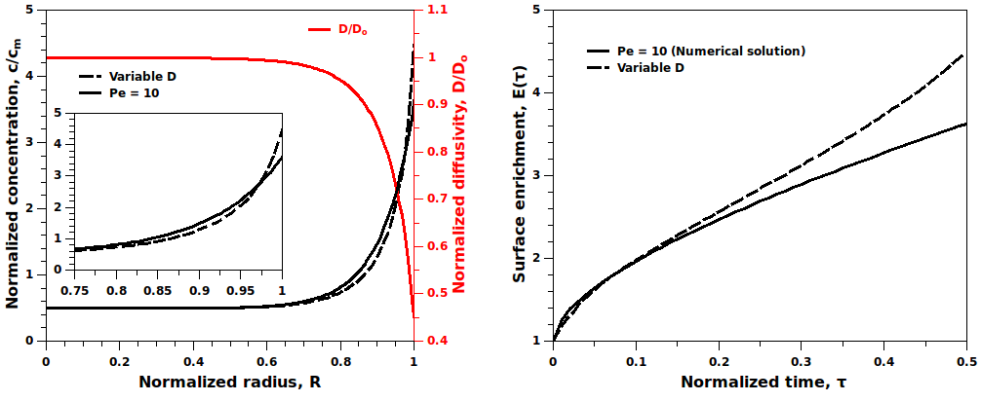

Figure 7.13: Evaporation with a variable diffusion coefficient, $D(c)$, for an initial Péclet number of 10 and $\lambda_D = 0.1$.

The relation between D and the concentration is solute dependent, but Equation 7.5 still represent the coupling between the diffusion coefficient, D, and the solute concentration, c. As a concentration gradient develops and higher solute concentrations are achieved near the droplet surface, the diffusivity drops which results in a higher surface enrichment, E. It is clear that surface enrichment exceeds the value of the corresponding surface enrichment for the case of a constant Péclet number, $Pe = 10$, because of the reduced diffusivity.

At such high initial Péclet number, the effect of variable D is limited to the region close to the droplet surface since the concentration at the core of the droplet is still close to the initial concentration. This is evident from the plot of the normalized diffusion coefficient, $\frac{D}{D_o}$, shown in the left panel of Figure 7.13.

7.4.3 Variable evaporation rate, $\kappa(c_s)$, and diffusion coefficient, $D(c)$

In this case, both the evaporation rate, κ, and the diffusion coefficient, D, were allowed to change for the case of an initial Péclet number of 10.

Figure 7.14 shows the evolution of the surface enrichment, E, compared to the case of a constant Péclet number, variable evaporation rate and variable diffusion coefficient. The current case is again bound by the two extreme cases of a variable

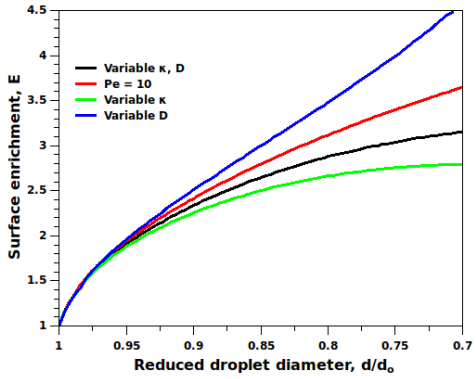

Figure 7.14: Evaporation with a variable evaporation rate, $\kappa(c_s)$, and diffusion coefficient, $D(c)$, for $\lambda_\kappa = 0.1$, $\lambda_D = 0.1$ and an initial Péclet number of 10.

evaporation rate (resulting in lower surface enrichment) and a variable diffusion coefficient (resulting in a higher surface enrichment). The result for a constant Péclet number is given as a reference case. During the initial evaporation period ($\frac{d}{d_o} = 1 : 0.95$) all the cases predict nearly the same surface enrichment values.

The dependence of the evaporation rate and diffusion coefficient on the solute concentration can be governed by any relation and the usability of the AISM is not limited to the form given in the current cases (Equation 7.3 and Equation 7.5).

7.5 Conclusions

Throughout this chapter the results of the AISM were verified using analytical and numerical results. The effect of different simulation parameters on the accuracy of the predicted concentration profiles were investigated. The ability of the AISM to predict the transient concentration profiles for cases with variable evaporation rate and material properties was demonstrated.

The flexibility of the proposed AISM offers many advantages in the design of engineered microparticles. By incorporating more physical mechanisms affecting the particle formation process, more realistic predictions can be obtained.

The use of the LBM for the solution of the concentration fields offers the extra advantage of dealing with complex geometries and variable material properties.

The AISM is a first step towards a comprehensive numerical framework for modeling the formation of structured microparticles.

Chapter 8

Discussion and future work

8.1 Discussion

Throughout this work, several aspects related to the formation of structured microparticles were investigated from a particle engineering perspective. The emphasis here is to provide simple and easy-to-use approaches to design structured microparticles with predefined set of desired properties. Although the present work does not discuss several other related processes like solute crystallization, it is thought that droplet evaporation and solute diffusion processes are the main ones controlling the particle formation process.

8.1.1 Calculation of the evaporation rate

In terms of predicting the evaporation rate, two approaches have been suggested along with the limitations and assumptions for each. Again, the emphasis here is to predict the variable evaporation rate of different solute/solvent combinations given tabulated, constant material properties. The simplified approach offers an easy estimation of the evaporation rate which is accurate enough during the preliminary stage of design, while the detailed approach offers extra accuracy at the cost of more computational work and a more sophisticated experimental setup.

The detailed approach takes into account the transient nature of the droplet evaporation process by solving the droplet/particle equation of motion in a time stepping manner. The effect of the used numerical scheme on the accuracy of the predicted evaporation rate was demonstrated. Several numerical schemes were tested along with the advantages and limitations of each. The use of a specific scheme depends largely on the problem at hand.

On the other hand, the simplified approach offers a faster and easier way of calculating the evaporation rate, but at the cost of more limitations. The simplified approach is more suitable for cases when the trajectory data has a large margin of uncertainty.

8.1.2 The simplified particle formation theory

The simplified particle formation theory proposed in chapter 2 introduces an easy and fast alternative of designing engineered microparticles with a desired set of proprieties. Despite its simplicity its results can greatly accelerate the development

stage of microparticle design and manufacturing. Recasting the model results in a non-dimensional form makes them more readily applicable to a variety of processing conditions. The model shows that with the extra effort needed to consider the transient nature of the concentration profiles, more accurate predictions for the final dry particle properties can be made without compromising the utility of the model. The usability of the model results were increased by fitting the numerical model results with analytical easy-to-use expressions.

The theory also introduces asymptotic approximations for different variables like the steady state surface enrichment and the evolution of the transient surface enrichment in the limit of high Péclet numbers. These approximations are a powerful tool when designing formulations containing suspensions or large molecular weight actives.

The characteristic times previously proposed by the VFL model can now be estimated more accurately after taking the transient nature of the problem into account. These characteristic times are good indicative parameters of the solid state of different components in final dry particle.

8.1.3 The Adaptive Interface Sweeping Method

The AISM approach proposed in chapter 6 is a first step towards building a comprehensive framework for a detailed numerical simulation of the particle formation process. It allows for the addition of many physical mechanisms that contribute to the particle formation process. This approach is more suitable if a fundamental understanding of the particle formation process is desired, especially for interacting multi-component formulations.

The numerical implementation of the AISM was discussed in detail. Different numerical parameters affecting the accuracy of the ASIM were investigated. The equations needed for the determination of these parameters were derived and verified by the model results.

The ability of the proposed approach to deal with cases that cannot be dealt with using the proposed simplified particle formation theory was demonstrated.

It has to be noted that the AISM can only be used for spherical or cylindrical droplets. Although it can deal with non-spherically symmetric variables fields, i.e., concentration, velocity, temperature, the droplet geometry itself has to stay spherical. This condition must be fulfilled because the droplet surface recession velocity is in the radial direction only for spherical droplets. This allows for the sweeping of the solute mass in the radial direction , which is one of the two main steps in the AISM algorithm.

8.2 Future work

There is still many improvements that can be introduced to enhance the predictive ability of the proposed simplified particle formation theory. This can be done by lifting one or more of the assumptions imposed during the development of the theory.

The first assumption that can be lifted is the assumption of a constant evaporation rate, κ. In this case, the Péclet number will change during the evaporation

process.

The second assumption is the assumption of a constant diffusion coefficient, D. For this assumption, two scenarios will be possible. The first is to assume that D is a function of the mean concentration, $c_{\mathrm{m}}(\tau)$, which results in a time dependent Pe number. The second possibility is to have D as a function of the local concentration, $c(R, \tau)$. In this case the definition of the Pe number is not valid and a more detailed model is need.

The AISM can be extended by including more physical mechanisms like internal circulation. The crystallization process can be modelled by incorporating a source term [Boraey and Epstein, 2010] in the diffusion equation to represent the formation of crystals. Suspension droplets can also be modelled by modelling the motion of the suspending particles during evaporation.

Bibliography

C.K. Aidun and J.R. Clausen. Lattice-boltzmann method for complex flows. *Annual Review of Fluid Mechanics*, 42(1):439–472, 2010.

N. Anton, A. Jakhmola, and T.F. Vandamme. Trojan microparticles for drug delivery. *Pharmaceutics*, 4:1–25, 2012.

D.Y. Arifin, L.Y. Lee, and C.-H. Wang. Mathematical modeling and simulation of drug release from microspheres: Implications to drug delivery systems. *Advanced Drug Delivery Reviews*, 58:1274–1325, 2006.

P.L. Bhatnagar, E.P. Gross, and M. Krook. A model for collision processes in gases. i. small amplitude processes in charged and neutral one-component systems. *Phys. Rev.*, 94:511–525, 1954.

R.B. Bird, W.E. Stewart, and E.N. Lightfoot. *Transport Phenomena*. John Wiley & Sons, Inc., 2nd edition, 2006.

M. Boraey, A. Baldelli, and R. Vehring. Theoretical and experimental investigation of particle formation from evaporating microdroplets. In *AAAR 32nd Annual Conference, American Association for Aerosol Research, Portland, Oregon, USA, September 30 - October 4*, 2013a.

M.A. Boraey and M. Epstein. Lattice boltzmann modeling of viscous elementary flows. *Advances in Applied Mathematics and Mechanics*, 2:451–466, 2010.

M.A. Boraey and R. Vehring. A particle design model for spray drying of suspensions and large molecule formulations. In *RDD Europe, Respiratory Drug Delivery.*, 2013.

M.A. Boraey and R. Vehring. Diffusion controlled formation of microparticles. *Journal of Aerosol Science*, 67:131–143, 2014.

M.A. Boraey, S. Matinkhoo, and R. Vehring. A new time and cost effective approach for the development of microparticles for pulmonary drug delivery. In *RDD Europe, Respiratory Drug Delivery.*, 2011.

M.A. Boraey, S. Hoe, H. Sharif, D.P. Miller, D. Lechuga-Ballesteros, and R. Vehring. Improvement of the dispersibility of spray-dried budesonide powders using leucine in an ethanol-water cosolvent system. *Powder Technology*, 236:171–178, 2013b.

F.J. Brechtel and S.M. Kreidenweis. Predicting particle critical supersaturation from hygroscopic growth measurements in the humidified tdma. part i: Theory and sensitivity studies. *Journal of the Atmospheric Sciences*, 57(12):1854–1871, 2000a.

F.J. Brechtel and S.M. Kreidenweis. Predicting particle critical supersaturation from hygroscopic growth measurements in the humidified tdma. part ii: Laboratory and ambient studies. *Journal of the Atmospheric Sciences*, 57(12):1872–1887, 2000b.

I. Castillo and R.J. Munz. Transient heat, mass and momentum transfer of an evaporating stationary droplet containing dissolved cerium nitrate in a rf thermal argon-oxygen plasma under reduced pressure. *International Journal of Heat and Mass Transfer*, 50(12):240–256, 2007a.

I. Castillo and R.J. Munz. Transient modeling of heat, mass and momentum transfer of an evaporating cerium nitrate solution droplet with a surrounding shell in a rf thermal argon-oxygen plasma under reduced pressure. *International Journal of Heat and Mass Transfer*, 50(2122):4468–4487, 2007b.

J. Champion, A. Walker, and S. Mitragotri. Role of particle size in phagocytosis of polymeric microspheres. *Pharmaceutical Research*, 25:1815–1821, 2008.

S. Chen and G.D. Doolen. Lattice boltzmann method for fluid flows. *Annual Review of Fluid Mechanics*, 30(1):329–364, 1998.

X.D. Chen, H. Sidhu, and M. Nelson. Theoretical probing of the phenomenon of the formation of the outermost surface layer of a multi-component particle, and the surface chemical composition after the rapid removal of water in spray drying. *Chemical Engineering Science*, 66(24):6375–6384, 2011.

R. Clift, J.R. Grace, and M.E. Weber. *Bubbles, Drops, and Particles*. Academic Press, 1978.

E.A. Corbanie, J.P. Remon, K. Van Reeth, W.J.M. Landman, J.H.H. van Eck, and C. Vervaet. Spray drying of an attenuated live newcastle disease vaccine virus intended for respiratory mass vaccination of poultry. *Vaccine*, 25:8306–8317, 2007.

E.A. Corbanie, C. Vervaet, J.H.H. van Eck, J.P. Remon, and W.J.M. Landman. Vaccination of broiler chickens with dispersed dry powder vaccines as an alternative for liquid spray and aerosol vaccination. *Vaccine*, 26:4469–4476, 2008.

L. Cruz, E. Fattal, L. Tasso, G.C. Freitas, A.B. Carregaro, S.S. Guterres, A.R. Pohlmann, and N. Tsapis. Formulation and in vivo evaluation of sodium alendronate spray-dried microparticles intended for lung delivery. *Journal of Controlled Release*, 152:370–375, 2011.

E.J. Davis. A history and state-of-the-art of accommodation coefficients. *Atmospheric Research*, 82:561–578, 2006.

P.F. DeCarlo, J.G. Slowik, D.R. Worsnop, P. Davidovits, and J.L. Jimenez. Particle morphology and density characterization by combined mobility and aerodynamic diameter measurements. part 1: Theory. *Aerosol Science and Technology*, 38: 1185–1205, 2004.

M. Eslamian and N. Ashgriz. Evaporation and evolution of suspended solution droplets at atmospheric and reduced pressures. *Drying Technology*, 25(6):999–1010, 2007.

M. Eslamian, M. Ahmed, and N. Ashgriz. Modeling of solution droplet evaporation and particle evolution in droplet-to-particle spray methods. *Drying Technology*, 27(1):3–13, 2009.

A.L. Feng, M.A. Boraey, M.A. Gwin, P.R. Finlay, P.J. Kuehl, and R. Vehring. Mechanistic models facilitate efficient development of leucine containing microparticles for pulmonary drug delivery. *International Journal of Pharmaceutics*, 409(1-2): 156–163, 2011.

W. H. Finlay. *Mechanics of Inhaled Pharmaceutical Aerosols - An Introduction*. Elsevier, 2001.

B. Fornberg. Generation of finite difference formulas on arbitrarily spaced grids. *Mathematics of Computation*, 51:699–706, 1988.

C. Gardner. Asymptotic concentration distribution of an involatile solute in an evaporating drop. *International Journal of Heat and Mass Transfer*, 8(4):667–668, 1965.

C. Gómez-Gaete, E. Fattal, L. Silva, M. Besnard, and N. Tsapis. Dexamethasone acetate encapsulation into trojan particles. *Journal of Controlled Release*, 128: 41–49, 2008.

C. Gómez Gaete, N. Tsapis, L. Silva, C. Bourgaux, and E. Fattal. Morphology, structure and supramolecular organization of hybrid 1,2-dipalmitoyl-sn-glycero-3-phosphatidylcholinehyaluronic acid microparticles prepared by spray drying. *European Journal of Pharmaceutical Sciences*, 34:12–21, 2008.

E. A. Guggenheim. The diffusion coefficient of sodium chloride. *Transactions of the Faraday Society*, 50:1048–1051, 1954.

S.S. Guterres, R.C.R. Beck, and A.R. Pohlmann. Spray-drying technique to prepare innovative nanoparticulated formulations for drug administration: a brief overview. *Brazilian Journal of Physics*, 39:205–209, 04 2009.

C.S. Handscomb, M. Kraft, and A.E. Bayly. A new model for the drying of droplets containing suspended solids. *Chemical Engineering Science*, 64(4):628–637, 2009a.

C.S. Handscomb, M. Kraft, and A.E. Bayly. A new model for the drying of droplets containing suspended solids after shell formation. *Chemical Engineering Science*, 64(2):228–246, 2009b.

W.C. Hinds. *Aerosol Technology: Properties, Behavior, and Measurement of Airborne Particles*. John Wiley & Sons, 1999.

S. Hoe, M.A. Boraey, J.W. Ivey, W.H. Finlay, and R. Vehring. Manufacturing and device options for the delivery of biotherapeutics. *Journal of Aerosol Medicine and Pulmonary Drug Delivery*, 27:1–14, 2013a.

S. Hoe, J. Ivey, M.A. Boraey, A. Shamsaddini-Shahrbabak, S. Matinkhoo, W.H. Finlay, and R. Vehring. A rational approach to spray drying multi-component formulations containing low-solubility actives. In *RDD Europe, Respiratory Drug Delivery.*, 2013b.

S. Hoe, J.W. Ivey, M.A. Boraey, A. Shamsaddini-Shahrbabak, E. Javaheri, S. Matinkhoo, W.H. Finlay, and R. Vehring. Use of a fundamental approach to spray-drying formulation design to facilitate the development of multi-component dry powder aerosols for respiratory drug delivery. *Pharmaceutical Research*, 0724-8741:1–17, 2013c.

S. Hoe, S. Matinkhoo, M. Boraey, J. Ivey, A. Shamsaddini-Shahrbabak, W.H. Finlay, and R. Vehring. Substitution of l-leucine with d-leucine in spraydried respirable powders for control of pseudomonas aeruginosa infection. In *19th International Congress. International Society for Aerosols in Medicine. Chapel Hill, North Carolina, USA, April 6:10*, 2013d.

C.J. Homer, X. Jiang, T.L. Ward, C.J. Brinker, and J.P. Reid. Measurements and simulations of the near-surface composition of evaporating ethanol-water droplets. *Phys. Chem. Chem. Phys.*, 11:7780–7791, 2009.

R.J. Hopkins and J.P. Reid. Evaporation of ethanol/water droplets: Examining the temporal evolution of droplet size, composition and temperature. *The Journal of Physical Chemistry A*, 109(35):7923–7931, 2005.

R.J. Hopkins and J.P. Reid. A comparative study of the mass and heat transfer dynamics of evaporating ethanol/water, methanol/water, and 1-propanol/water aerosol droplets. *The Journal of Physical Chemistry B*, 110(7):3239–3249, 2006.

G.L. Hubbard, V.E. Denny, and A.F. Mills. Droplet evaporation: Effects of transients and variable properties. *International Journal of Heat and Mass Transfer*, 18(9):1003–1008, 1975.

P.T. Ingvarsson, S.T. Schmidt, D. Christensen, N.B. Larsen, W.L.J. Hinrichs, P. Andersen, J. Rantanen, M.H. Nielsen, M. Yang, and C. Foged. Designing caf-adjuvanted dry powder vaccines: Spray drying preserves the adjuvant activity of caf01. *Journal of Controlled Release*, 167:256–264, 2013.

G.V. Jayanthi, S.C. Zhang, and G.L. Messing. Modeling of solid particle formation during solution aerosol thermolysis: The evaporation stage. *Aerosol Science and Technology*, 19(4):478–490, 1993.

X. Jiang, T.L. Ward, F. Swol, and C.J. Brinker. Numerical simulation of ethanol-water-nacl droplet evaporation. *Industrial & Engineering Chemistry Research*, 49 (12):5631–5643, 2010.

G. Lamanna, H. Sun, B. Weigand, D. Magatti, P. Micciché, and F. Ferri. Measurements of droplet vaporisation by means of light scattering. *Colloids and Surfaces A: Physicochemical and Engineering Aspects*, 261(13):153–161, 2005.

H.K. Lee, J. H. Park, and K. C. Kwon. Double-walled microparticles for single shot vaccine. *Journal of Controlled Release*, 44:283–293, 1997.

S.K. Lele. Compact finite difference schemes with spectral-like resolution. *Journal of Computational Physics*, 103(1):16–42, 1992.

I.W. Lenggoro, T. Hata, F. Iskandar, M.M. Lunden, and K. Okuyama. An experimental and modeling investigation of particle production by spray pyrolysis using a laminar flow aerosol reactor. *Journal of Materials Research*, 15:733–743, 2000.

K.H. Leong. Morphological control of particles generated from the evaporation of solution droplets: Theoretical considerations. *Journal of Aerosol Science*, 18(5): 511–524, 1987.

J.-C. Lin and J.W. Gentry. Spray drying drop morphology: Experimental study. *Aerosol Science and Technology*, 37(1):15–32, 2003.

Y. Lu and K. Park. Polymeric micelles and alternative nanonized delivery vehicles for poorly soluble drugs. *International Journal of Pharmaceutics*, 453:198–214, 2013.

K. Mahesh. A family of high order finite difference schemes with good spectral resolution. *Journal of Computational Physics*, 145(1):332–358, 1998.

M.J. Maltesen, S. Bjerregaard, L. Hovgaard, S. Havelund, and M. van de Weert. Quality by design - spray drying of insulin intended for inhalation. *European Journal of Pharmaceutics and Biopharmaceutics*, 70:828–838, 2008.

G. Marty and N. Tsapis. Monitoring the buckling threshold of drying colloidal droplets using water-ethanol mixtures. *European Physical Journal E – Soft Matter*, 27:213–219, 2008.

S. Matinkhoo, K.H. Lynch, J.J. Dennis, W.H. Finlay, and R. Vehring. Spray-dried respirable powders containing bacteriophages for the treatment of pulmonary infections. *Journal of Pharmaceutical Sciences*, 100:5197–5205, 2011.

S. Matinkhoo, S. Hoe, M. Boraey, A. Shamsaddini-Shahrbabak, W.H. Finlay, and R. Vehring. Spray drying d-amino acids to develop respirable dry powder for the treatment of pseudomonas aeruginosa biofilms. In *2012 AAPS Annual Meeting and Exposition, American Association of Pharmaceutical Scientists, McCormick Place, Chicago, October 14:18*, 2012.

P. Moin. *Fundamentals of Engineering Numerical Analysis*. Cambridge University Press, 2nd edition, 2010.

A.B.D. Nandiyanto and K. Okuyama. Progress in developing spray-drying methods for the production of controlled morphology particles: From the nanometer to submicrometer size ranges. *Advanced Powder Technology*, 22(1):1–19, 2011.

H. Nie, Z. Dong, D.Y. Arifin, Y. Hu, and C.-H. Wang. Core/shell microspheres via coaxial electrohydrodynamic atomization for sequential and parallel release of drugs. *Journal of Biomedical Materials Research Part A*, 95A:709–716, 2010.

K. Okuyama and I.W. Lenggoro. Preparation of nanoparticles via spray route. *Chemical Engineering Science*, 58(36):537–547, 2003.

K. Okuyama, M. Abdullah, I.W. Lenggoro, and F. Iskandar. Preparation of functional nanostructured particles by spray drying. *Advanced Powder Technology*, 17:587–611, 2006a.

K. Okuyama, M. Abdullah, I.W. Lenggoro, and K. Iskandar. Preparation of functional nanostructured particles by spray drying. *Advanced Powder Technology*, 17 (6):587–611, 2006b.

T. Okuzono, K. Ozawa, and M. Doi. Simple model of skin formation caused by solvent evaporation in polymer solutions. *Phys. Rev. Lett.*, 97:136103, 2006.

E.P. Pakhomov. On the density of zirconium dioxide. *High Temperature*, 49:766–768, 2011.

K. Park, I.C. Kwon, and K. Park. Oral protein delivery: Current status and future prospect. *Reactive and Functional Polymers*, 71:280–287, 2011.

N. Roth, J. Wilms, and B. Weigand. Technique for measurements of the evaporation rate of single, freely falling, droplets. In *12th International Symposium on Application of Laser Techniques to Fluid Mechanics, Lisbon*, 2004.

S.P. Schwendeman. Recent advances in the stabilization of proteins encapsulated in injectable plga delivery systems. *Critical Reviews in Therapeutic Drug Carrier Systems*, 19:26, 2002.

P. Seydel, J. Blömer, and J. Bertling. Modeling particle formation at spray drying using population balances. *Drying Technology*, 24(2):137–146, 2006.

W.A. Sirignano. *Fluid Dynamics and Transport of Droplets and Sprays*. Cambridge University Press, 1999.

E.C. Tan, R. Lin, and C.-H. Wang. Fabrication of double-walled microspheres for the sustained release of doxorubicin. *Journal of Colloid and Interface Science*, 291:135–143, 2005.

I.N. Tang and H.R. Munkelwitz. An investigation of solute nucleation in levitated solution droplets. *Journal of Colloid and Interface Science*, 98(2):430–438, 1984.

R. Vehring. Red-excitation dispersive raman spectroscopy is a suitable technique for solid-state analysis of respirable pharmaceutical powders. *Applied Spectroscopy*, 59(7):286–292, 2005.

R. Vehring. Pharmaceutical particle engineering via spray drying. *Pharmaceutical Research*, 25:999–1022, 2008.

R. Vehring, W.R. Foss, and D. Lechuga-Ballesteros. Particle formation in spray drying. *Journal of Aerosol Science*, 38(7):728–746, 2007.

R. Vehring, D. Lechuga-Ballesteros, V. Joshi, B. Noga, and S.K. Dwivedi. Cosuspensions of microcrystals and engineered microparticles for uniform and efficient delivery of respiratory therapeutics from pressurized metered dose inhalers. *Langmuir*, 28:15015–15023, 2012.

J.G. Weers, T.E. Tarara, and A.R. Clark. Design of fine particles for pulmonary drug delivery. *Expert Opinion on Drug Delivery*, 4:297–313, 2007.

C. Weiler, J.H. Sahner, M. Munz, and C.-M. Lehr. Effect of molecular weight and process parameters on the morphology of spray-dried dextran particles. In *Respiratory Drug Delivery 2012*, volume 2, pages 421–426, 2012.

W. Widiyastuti, W.-N. Wang, I.W. Lenggoro, F. Iskandar, and K. Okuyama. Simulation and experimental study of spray pyrolysis of polydispersed droplets. *Journal of Materials Research*, 22(07):1888–1898, 2007.

C. Wischke and S.P. Schwendeman. Principles of encapsulating hydrophobic drugs in pla/plga microparticles. *International Journal of Pharmaceutics*, 364:298–327, 2008.

Y. Xiong and T.T. Kodas. Droplet evaporation and solute precipitation during spray pyrolysis. *Journal of Aerosol Science*, 24(7):893–908, 1993.

Q. Xu, S.E. Chin, C.H. Wang, and D.W. Pack. Mechanism of drug release from double-walled pdlla(plga) microspheres. *Biomaterials*, 34:3902–3911, 2013.

H.-F. Yu and W.-H. Liao. Evaporation of solution droplets in spray pyrolysis. *International Journal of Heat and Mass Transfer*, 41(89):993–1001, 1998.

S. Yuk, K. Oh, S. Kim, J. Lee, S. Cho, K. Kim, H. Jeon, and I. Kwon. Multicore vesicle nanoparticles for controlled delivery of protein drug. *Macromolecular Research*, 20(3):309–312, 2012.

Appendix A

Asymptotic concentration profiles of an evaporating spherical solution droplet

A.1 Introduction

This appendix gives a detailed derivation of the asymptotic concentration profiles of an evaporating spherical solution droplet as presented by Gardner [1965]; Leong [1987]; Vehring et al. [2007].

A.2 Derivation

The asymptotic concentration profiles and surface enrichment for an evaporating spherical solution droplet were obtained analytically by Gardner [Gardner, 1965].

Gardner [Gardner, 1965] started with the one dimensional diffusion equation in spherical coordinates which can be written as follows:

$$\frac{\partial C}{\partial t} = D\left[\frac{\partial^2 C}{\partial r^2} + \frac{2}{r}\frac{\partial C}{\partial r}\right] \tag{A.1}$$

The radial coordinate, r, can be normalized by the droplet time dependent radius, $r_s(t)$, to give the following normalized equation.

$$\frac{\partial C}{\partial t} = \frac{D}{r_s^2(t)}\left(\frac{\partial^2 C}{\partial R^2} + \frac{2}{R}\frac{\partial C}{\partial R}\right) + \frac{R}{r_s(t)}\frac{\partial C}{\partial R}\frac{\partial r_s(t)}{\partial t} \tag{A.2}$$

The assumption of a constant evaporation rate, κ, as defined by Vehring [2008] and Vehring et al. [2007] can be written as follows [Gardner, 1965]:

$$d^2(t) = -\kappa t \tag{A.3}$$

$$r_s^2(t) = -\frac{1}{4}\kappa t \tag{A.4}$$

$$\frac{\partial r_s^2(t)}{\partial t} = -\frac{1}{4}\kappa \tag{A.5}$$

$$\frac{\partial r_{\mathrm{s}}(t)}{\partial t} = -\frac{1}{8}\frac{\kappa}{r_{\mathrm{s}}} \tag{A.6}$$

Substituting Equation A.4 and Equation A.6 in Equation A.2 and using the definition of the Péclet number, $Pe = \frac{\kappa}{8D}$ [Vehring, 2008; Vehring et al., 2007], Equation A.2 can be written as follows after normalizing the concentration, C:

$$\frac{\partial^2 c}{\partial R^2} + \frac{\partial c}{\partial R}\left[\frac{2}{R} - RPe\right] + 2Pe\frac{\partial c}{\partial t}t = 0 \tag{A.7}$$

For the asymptotic state, the concentration, c, at any point, R, is proportional to the inverse of the droplet radius, $r_s(t)$, cubed. (This is equivalent to saying that all points will have a concentration, $c(R)$, that is changing with the same rate as the mean concentration, c_{m}).

$$c_{\mathrm{o}} r_{\mathrm{o}}^3 = c r_{\mathrm{s}}^3 \tag{A.8}$$

$$c = c_{\mathrm{o}}\left(\frac{r_{\mathrm{o}}}{r_{\mathrm{s}}}\right)^3 \tag{A.9}$$

$$c \propto r_{\mathrm{s}}^{-3} \tag{A.10}$$

From Equation A.4 we can derive the relation between the droplet radius, $r_{\mathrm{s}}(t)$, and time, t, as follows:

$$r_{\mathrm{s}}^2(t) \propto -t \tag{A.11}$$

$$r_{\mathrm{s}}^3(t) \propto (-t)^{\frac{3}{2}} \tag{A.12}$$

From Equation A.10 and Equation A.12 the concentration, $c(t)$, at any point, R, in the asymptotic state can be written as follows:

$$c \propto (-t)^{-\frac{3}{2}} \tag{A.13}$$

$$c = A(-t)^{-\frac{3}{2}} \tag{A.14}$$

Where: A is a constant.

The term $-t\frac{\partial c}{\partial t}$ in Equation A.7 can be replaced by a time independent term in the asymptotic state as follows:

$$c = A(-t)^{-\frac{3}{2}} \tag{A.15}$$

$$\frac{\partial c}{\partial t} = \frac{3}{2}A(-t)^{-\frac{5}{2}} \tag{A.16}$$

$$-t\frac{\partial c}{\partial t} = \frac{3}{2}A(-t)^{-\frac{3}{2}} \tag{A.17}$$

$$-t\frac{\partial c}{\partial t} = \frac{3}{2}c \tag{A.18}$$

Substituting Equation A.18 in Equation A.7 gives the following equation for the solute concentration at the asymptotic state.

$$\frac{\partial^2 c}{\partial R^2} + \frac{\partial c}{\partial R}\left[\frac{2}{R} - RPe\right] - 3cPe = 0 \tag{A.19}$$

The solution for equation Equation A.19 under the boundary condition, $\frac{\partial c}{\partial R}|_{R=0} = 0$ is given by:

$$c(R) = c_{\mathrm{c}} \exp\left[\left(\frac{Pe}{2}\right) R^2\right] \tag{A.20}$$

Where: c_{c} is the concentration at the droplet center (which is time dependent).

The mean concentration, c_{m}, can then be calculated from $c(R)$ as follows:

$$\frac{4}{3}\pi(1)^3 c_{\mathrm{m}} = \int_0^1 c(R) 4\pi R^2 \mathrm{d}R \tag{A.21}$$

$$c_{\mathrm{m}} = 3c_{\mathrm{c}} \int_0^1 R^2 \exp\left[\left(\frac{Pe}{2}\right) R^2\right] \mathrm{d}R \tag{A.22}$$

$$c_{\mathrm{m}} = 3c_{\mathrm{c}}\beta \tag{A.23}$$

$$\beta = \int_0^1 R^2 \exp\left[\left(\frac{Pe}{2}\right) R^2\right] \mathrm{d}R \tag{A.24}$$

Equation A.24 can not be integrated analytically to calculate β and has to be numerically evaluated for each Pe number.

Using Equation A.23, the concentration $c(R)$ can be expressed as follows:

$$c(R) = \frac{c_{\mathrm{m}}}{3\beta} \exp\left[\left(\frac{Pe}{2}\right) R^2\right] \tag{A.25}$$

And the surface concentration, c_{s}, is obtained at $R = 1$ as following

$$c_{\mathrm{s}} = \frac{c_{\mathrm{m}}}{3\beta} \exp\left(\frac{Pe}{2}\right) \tag{A.26}$$

Surface enrichment, E, can be calculated from Equation A.26 as follows:

$$E = \frac{c_{\mathrm{s}}}{c_{\mathrm{m}}} = \frac{1}{3\beta} \exp\left(\frac{Pe}{2}\right) \tag{A.27}$$

Surface enrichment, E, can also be approximated using the relation given by Vehring [2008]; Vehring et al. [2007]:

$$E = \frac{c_{\mathrm{s}}}{c_{\mathrm{m}}} \approx 1 + \frac{Pe}{5} + \frac{Pe^2}{100} - \frac{Pe^3}{4,000} \tag{A.28}$$

Equation A.28 is accurate within 1% for Pe <20.

Appendix B

Derivation of the droplet diameter updating equation

B.1 Introduction

It is required to derive a form for the droplet diameter updating equation such that the denominator is not zero for any point in the droplet trajectory.

B.2 The derivation

Starting by witting Equation 4.29 as follows:

$$d(t+\Delta t) \approx d(t) + \frac{2\Delta t}{\mathbf{v}\pi\rho_l d^2(t)} \left[\mathbf{F}_{\mathrm{G}} + \mathbf{F}_{\mathrm{D}} - m\mathbf{a}\right] \tag{B.1}$$

This equation can be written for both directions ($X\&Y$) of the used coordinate system as follows:

$$d(t+\Delta t) \approx d(t) + \frac{2\Delta t}{v_x\pi\rho_l d^2(t)} \left[F_{\mathrm{G}x} + F_{\mathrm{D}x} - ma_x\right] \tag{B.2}$$

$$d(t+\Delta t) \approx d(t) + \frac{2\Delta t}{v_y\pi\rho_l d^2(t)} \left[F_{\mathrm{G}y} + F_{\mathrm{D}y} - ma_y\right] \tag{B.3}$$

Summing Equation B.2 and Equation B.3 results in the following equation:

$$d(t+\Delta t) \approx d(t) + \frac{\Delta t}{\pi\rho_l d^2(t)} \left[\frac{F_{\mathrm{G}x} + F_{\mathrm{D}x} - ma_x}{v_x} + \frac{F_{\mathrm{G}y} + F_{\mathrm{D}y} - ma_y}{v_y}\right] \tag{B.4}$$

Equation B.4 does not solve the problem that arises if one of the two velocity components ($v_x\&v_y$) is zero. This can be solved by manipulating the equation as follows:

$$d(t+\Delta t) \approx d(t) + \frac{\Delta t}{\pi\rho_l d^2(t)} \frac{v_x+v_y}{v_x+v_y} \left[\frac{F_{\mathrm{G}x} + F_{\mathrm{D}x} - ma_x}{v_x} + \frac{F_{\mathrm{G}y} + F_{\mathrm{D}y} - ma_y}{v_y}\right] \tag{B.5}$$

$$d(t+\Delta t) \approx d(t) + \frac{\Delta t}{\pi \rho_l d^2(t)} \frac{1}{v_x + v_y} \left[(F_{\mathrm{G}x} + F_{\mathrm{D}x} - ma_x) \left(1 + \frac{v_y}{v_x}\right) + (F_{\mathrm{G}y} + F_{\mathrm{D}y} - ma_y) \left(1 + \frac{v_x}{v_y}\right) \right] \tag{B.6}$$

From Equation B.2 and Equation B.3 the following relations can be derived:

$$\frac{F_{\mathrm{G}x} + F_{\mathrm{D}x} - ma_x}{v_x} = \frac{F_{\mathrm{G}y} + F_{\mathrm{D}y} - ma_y}{v_y} \tag{B.7}$$

$$\frac{v_x}{v_y} = \frac{F_{\mathrm{G}x} + F_{\mathrm{D}x} - ma_x}{F_{\mathrm{G}y} + F_{\mathrm{D}y} - ma_y} \tag{B.8}$$

$$\frac{v_y}{v_x} \left[F_{\mathrm{G}x} + F_{\mathrm{D}x} - ma_x\right] = F_{\mathrm{G}y} + F_{\mathrm{D}y} - ma_y \tag{B.9}$$

$$\frac{v_x}{v_y} \left[F_{\mathrm{G}y} + F_{\mathrm{D}y} - ma_y\right] = F_{\mathrm{G}x} + F_{\mathrm{D}x} - ma_x \tag{B.10}$$

Substituting Equation B.9 and Equation B.10 in Equation B.6 gives the required equation.

$$d(t+\Delta t) \approx d(t) + \frac{2\Delta t}{(v_x + v_y)\pi \rho_l d^2(t)} \left[F_{\mathrm{G}x} + F_{\mathrm{G}y} + F_{\mathrm{D}x} + F_{\mathrm{D}y} - m(a_x + a_y)\right] \tag{B.11}$$

The denominator of Equation B.11 will not be zero as long as the sum of the two velocity components (v_x&v_y) is not zero. The used coordinate system is chosen to ensure that this condition is satisfied (see Figure 4.1) by forcing both velocity components to be positive during the whole trajectory.

B.3 Another derivation

Another way to derive Equation B.11 is by writing Equation B.2 and Equation B.3 as follows:

$$F_{\mathrm{G}x} + F_{\mathrm{D}x} - ma_x \approx \frac{v_x \pi \rho_l d^2(t)}{2\Delta t} \left[d(t+\Delta t) - d(t)\right] \tag{B.12}$$

$$F_{\mathrm{G}y} + F_{\mathrm{D}y} - ma_y \approx \frac{v_y \pi \rho_l d^2(t)}{2\Delta t} \left[d(t+\Delta t) - d(t)\right] \tag{B.13}$$

Summing Equation B.12 and Equation B.13 and rearranging the resulting equation gives the required form for the droplet diameter updating equation as follows:

$$F_{\mathrm{G}x} + F_{\mathrm{G}y} + F_{\mathrm{D}x} + F_{\mathrm{D}y} - m(a_x + a_y) \approx \frac{(v_x + v_y)\pi \rho_l d^2(t)}{2\Delta t} \left[d(t+\Delta t) - d(t)\right] \tag{B.14}$$

$$d(t+\Delta t) \approx d(t) + \frac{2\Delta t}{(v_x + v_y)\pi \rho_l d^2(t)} \left[F_{\mathrm{G}x} + F_{\mathrm{G}y} + F_{\mathrm{D}x} + F_{\mathrm{D}y} - m(a_x + a_y)\right] \tag{B.15}$$

Appendix C

Physical properties of Air & Acetone

C.1 Physical properties of Air

Dynamic viscosity: $\mu = 1.98 \times 10^{-5}$ Pa.s
Thermal conductivity: $k = 0.0257$ W/m.K
Density: $\rho_{\mathrm{dg}} = 1.2$ kg/m^3

C.2 Physical properties of Acetone

Diffusion coefficient in air: $D_{\mathrm{s}} = 1.24 \times 10^{-5}$ m^2/s
Latent heat of vaporization: $L = 510 \times 10^3$ J/kg
Molecular weight: $M_{\mathrm{s}} = 58.08 \times 10^{-3}$ kg/mol
Density: $\rho_{\mathrm{l}} = 791$ kg/m^3
Specific heat: $c_{\mathrm{p}} = 2150$ J/kg.K

C.2.1 Antoine equation (vapor pressure)

$P = 10^{A - \frac{B}{T+C}}$
P: Vapor pressure in bar
T: Temperature in K
$A = 4.42448$
$B = 1312.253$
$C = -32.445$